FRIEDRICH-SCHILLER-
UNIVERSITÄT
JENA

Thermodynamic properties, crystal structures, phase relations and isotopic studies of selected copper oxysalts

Dissertation

zur Erlangung des akademischen Grades doctor rerum naturalium
(Dr. rer. nat.)

vorgelegt dem Rat der Chemisch-Geowissenschaftlichen Fakultät der
Friedrich-Schiller-Universität Jena

von Alexandra Mathilde Plumhoff, M.Sc.
geboren am 02.07.1987
in Darmstadt, Deutschland

Gutachter:

1. Prof. Dr. Juraj Majzlan, FSU Jena
2. Prof. Dr. Thorsten Schäfer, FSU Jena

Tag der Verteidigung: 04. November 2020

To my family

“When things go wrong, as they sometimes will,
When the road you’re trudging seems all uphill,
When the funds are low and the debts are high
And you want to smile but you have to sigh.
When care is pressing you down a bit,
Rest if you must, but don't you quit.
Life is strange with its twists and turns
As every one of us sometimes learns
And many a failure comes about
When he might have won had he stuck it out;
Don't give up though the pace seems slow—
You may succeed with another blow.
Success is failure turned inside out—
The silver tint on the clouds of doubt,
And you can never tell how close you are,
It may be near when it seems far;
So stick to the fight when you’re hardest hit—
It’s when things go wrong that you must not quit.”

(John Greenleaf Whittier)

Selbstständigkeitserklärung

Ich erkläre, dass ich die vorliegende Arbeit selbstständig und unter Verwendung der angegebenen Hilfsmittel, persönlichen Mitteilungen und Quellen angefertigt habe.

……. …….

(Ort, Datum) (Unterschrift der Verfasserin)

Acknowledgement

Indeed, I had to write this thesis by myself, but for its success, the support and guidance of a lot of people were involved. For this, I want to thank them.

Special thanks go to my advisors – without them it would not have been possible to write a dissertation at the Institute of Geosciences at the FSU Jena. I want to thank Prof. Dr. **Juraj Majzlan** for his guidance and support through my Ph.D. work. He gave me the chance to meet a lot of new people and researchers that I was able to work with. I also want to thank Prof. Dr. **Thorsten Schäfer** for his support and his feedback, who kindly agreed to be my second reviewer for this thesis.

Furthermore, I would like to thank PD Dr. **Klaus-Dieter Grevel**, for spending hours discussing data with me. I benefited greatly from his help and his ideas. He constantly motivated me throughout my Ph.D. research.

Moreover, I would like to thank all the researchers I was able to work with. Prof. Dr. **Ryan Mathur**, for his constructive discussions and feedback on my isotopic work. He kept in touch with me even when it was in long time intervals. **Rastislav Milovský**, who showed me his lab and was helpful with all questions concerning stable isotopes. **Jakub Plášil** for the single crystal measurements and his needed help to understand and use JANA. **Edgar Dachs** and **Artur Benisek**, for doing the calorimetric measurements that completed the thermodynamic data for my studied phases. **Martin Števko** and **Mike Rumsey** for sharing their knowledge about copper arsenate ore deposits. **Frank Bok** for his constant help with Geochemist's workbench®. **Maciej Manecki** with his input and support to synthesize the solid solution.

Additionally, I want to thank **Marcel Görn**, **Patrick Haase**, **Julia Hermann**, **Wiebke Nowak** and **Marcus Böhm** for their (mental) support throughout the whole Ph.D. work, including very long discussions and conversations.

Finally, and most important, I want to thank my family, **Peter**, **Christa**, und **Thomas Plumhoff**, **Christa Balz** and **Steffen Schuhmann** for their patience and support, especially during the stressful and final part of my Ph.D. thesis.

Abstract

Variability in the chemical and isotopic composition and crystal chemical properties of secondary copper minerals lends them for the understanding of the formation and evolution of oxidation zones of ore deposits. Among others, copper arsenates and carbonates are common and widely distributed minerals in such oxidation zones where they form through weathering of the primary minerals. Copper arsenates are not only capable of taking up and releasing copper and arsenic but also other elements such as lead, zinc and phosphor.

One part of this thesis is focused on how these minerals form, their thermodynamic properties, stabilities and crystal chemical data. These topics will be discussed in two chapters. The minerals investigated so far are liroconite [$Cu_2Al(AsO_4)(OH)_4 \cdot 4H_2O$], pushcharovskite [$Cu(AsO_3OH)(H_2O) \cdot 0.5H_2O$], geminite [$Cu(AsO_3OH)(H_2O)$], adamite [$Zn_2(AsO_4)(OH)$] and zincolivenite [$CuZn(AsO_4)(OH)$] as well as the olivenite-libethenite solid solution series, $Cu_2(PO_4)_x(AsO_4)_{1-x}(OH)$ [$0 \leq x \leq 1$]. All samples were synthesized by wet chemical methods in our laboratory, except for the natural liroconite. The phases were characterized by powder X-ray diffraction, infrared spectroscopy, electron microprobe analysis, thermogravimetric analysis and optical emission spectrometry, as needed. Their thermodynamic properties were determined by a combination of acid-solution calorimetry and relaxation calorimetry (Table 1). These thermodynamic data were used to supplement the Lawrence Livermore National Laboratory (LLNL) database which is used for common geochemical modelling programs as PhreeqC and Geochemist's workbench®. With these programs, the stability fields and formation conditions of the before mentioned secondary copper minerals were modelled and compared to natural paragenesis of several ore deposits. The formation of liroconite, in its type locality in Wheal Gorland, Cornwall, UK, requires circumneutral fluids in an Al-rich environment that is poor in Fe, Pb or other interfering metals. In contrast, geminite and pushcharovskite are minerals typical for very acidic solutions with no carbonates present (or accessory).

In addition to the study of the formation conditions, the crystal structure of liroconite was refined by single-crystal X-ray diffraction and the positions of H atoms, not known previously, were determined.

Table 1. Thermodynamic properties of the studied phases. All enthalpy and Gibbs free energy values are in $kJ \cdot mol^{-1}$, all entropy values are in $J \cdot mol^{-1} \cdot K^{-1}$.

	$\Delta_f H^\circ$	S^o	$\Delta_f S^\circ$	$\Delta_f G^\circ$	$\log K_{sp}$
Liroconite (natural)	–3516.6±9.1	401.1±4.8	–1745.1±4.9	–2996.3±9.2	–4.92
Liroconite (estimate for the phosphate-free end-member)				–2931.6	–4.85
Pushcharovskite	–1250.5±3.0	176.4±2.1	–718.0±2.3	–1036.4±3.8	–17.21
Geminite (natural)	–1110.4±3.0	158.2	–619.5	–925.7±3.2	–18.58
Geminite (synth.)	–1111.4±3.0	158.2	–619.5	–926.7±3.2	–18.75
Adamite	–1401.7±3.2	160.1±0.5	–537.1±1.0	–1247.6±3.4	–10.90
Zincolivenite	–1211.6±3.2	159.5±0.5	–529.6±1.0	–1053.7±3.4	–13.33
Olivenite	–997.3±3.2	158.9±0.5	–521.3±1.0	–841.9±3.4	–15.30
Libethenite	–1384.4±3.2	163.4±0.5	–522.2±1.0	–1228.7±3.4	–16.86

For the olivenite-libethenite solid solution series the unit cell parameters show a development following the size of the ionic radii from phosphor to arsenic as well as the bands of the infrared spectroscopy. The calculated ΔH^{MIX} values are positive for all values of X_{lib} with a maximum value around X_{lib} = 0.59 and a distinct step between X_{lib} = 0.69 and 0.79 which indicates the change in the crystal structure from monoclinic (olivenite) to orthorhombic (libethenite). All results together with the thermodynamic excess properties of the olivenite–libethenite solid solution show that a complete solid solution series without miscibility gap exists, with an easier incorporation of phosphor than of arsenic.

The third part of this thesis is focused on the isotopic fractionation of the copper, oxygen and hydrogen isotopes between malachite and aqueous solution which was determined by precipitation experiments over the temperature range from 10 to 65 °C. The solid products were characterized by powder X-ray diffraction, infrared spectroscopy and thermogravimetric analysis and consisted of a single phase $Cu_2CO_3(OH)_2$, corresponding to the mineral malachite. The isotopic fractionation factors for oxygen and hydrogen could be divided in two temperature regions (10-35 °C and 45-65 °C) (Table 2) due to a non-linear change in the isotopic values at around 40 °C. This change is related to the initial precipitation of georgeite (X-ray amorphous $Cu_2CO_3(OH)_2$) and the isotopic exchange of this mineral and the malachite formed from georgeite. The isotopic fractionation factor for copper is defined over the whole temperature range (10-65 °C) (Table 2) with a distinct temperature dependent fractionation and an average fractionation shift of $\Delta^{65}Cu_{sol\text{-}mal} = -0.16 \pm 0.05$ ‰. This fractionation shift implies that chemical reactions for oxide minerals without change of the redox state yield only minor copper isotope fractionation. With the application of the fractionation factors of oxygen and hydrogen of malachite onto source water from the meteoric water line, we were able to calculate the "malachite line" which represents the isotopic compositions of malachite that would precipitate from such water. Additionally, the calculated fractionation factors of oxygen and hydrogen were used to determine the oxygen and hydrogen isotopic composition of the formation waters of natural malachite samples from a number of localities worldwide and correlated to the isotopic composition of rain waters of nearby stations. Together with the Cu isotopes of the natural malachite samples, it is to assume that all investigated malachite samples are supergene samples which formed from meteoric water.

Table 2. Values for A and B of the equation for the isotopic fractionation factors of oxygen, hydrogen and copper in the form of 1000 ln α = A ($10^6/T^2$) + B, with T the temperature in Kelvin.

	temperature range	A	B
$oxygen_{georgeite\text{-}solution}$	10 – 35 °C	2.705 ± 0.156	4.064 ± 1.785
$oxygen_{malachite\text{-}solution}$	45 – 65 °C	2.866 ± 0.328	0.957 ± 3.055
$hydrogen_{georgeite\text{-}solution}$	10 – 35 °C	0.214 ± 0.473	–27.473 ± 5.519
$hydrogen_{malachite\text{-}solution}$	45 – 65 °C	–1.472 ± 0.607	–22.294 ± 5.651
$copper_{solution\text{-}malachite}$	10 – 65 °C	0.033 ± 0.013	–0.185 ± 0.136

Kurzfassung

Die Variabilität in der chemischen und isotopischen Zusammensetzung sowie die kristallchemischen Eigenschaften sekundärer Kupferminerale sind von großer Bedeutung für das Verständnis der Bildung und Entwicklung von Oxidationszonen in Erzlagerstätten. Unter anderem sind Kupferarsenate und –karbonate häufige und weit verbreitete Minerale in solchen Oxidationszonen, wo diese durch Verwitterung von primären Mineralen entstehen. Kupferarsenate sind nicht nur fähig, Kupfer und Arsen aufzunehmen und abzugeben, sondern auch andere Elemente wie Blei, Zink und Phosphor.

Ein Teil dieser Dissertation konzentriert sich auf die Bildung dieser Minerale, deren thermodynamische Eigenschaften, Stabilitätsbereiche und kristallchemische Daten. Diese Themen werden in zwei Kapiteln behandelt. Die untersuchten Minerale sind Lirokonit [$Cu_2Al(AsO_4)(OH)_4 \cdot 4H_2O$], Pushcharovskit [$Cu(AsO_3OH)(H_2O) \cdot 0.5H_2O$], Geminit [$Cu(AsO_3OH)(H_2O)$], Adamit [$Zn_2(AsO_4)(OH)$] und Zinkolivenit [$CuZn(AsO_4)(OH)$] sowie die Olivenit–Libethenit Mischkristallreihe, $Cu_2(PO_4)_x(AsO_4)_{1-x}(OH)$ [$0 \leq x \leq 1$]. Alle Proben, außer einer natürlichen Lirokonit-Probe, wurden mittels nasschemischer Methoden synthetisiert. Die Phasen wurden, je nach Bedarf, mittels Pulverröntgendiffraktometrie, Infrarotspektroskopie, Elekronenstrahlmikrosondenanalysen, thermogravimetrischen Analysen und optischer Emissionsspektrometrie charakterisiert. Die thermodynamischen Eigenschaften wurden mit einer Kombination aus Säure-Lösungskalorimetrie und Relaxationskalorimetrie bestimmt (Tabelle 1). Die erhaltenen thermodynamischen Daten wurden genutzt, um die Lawrence Livermore National Laboratory (LLNL) Datenbank zu ergänzen, welche für geochemische Modellierungsprogramme wie PhreeqC und Geochemist's workbench® benutzt wird. Mit diesen Programmen wurden die Stabilitätsfelder und Bildungsbedingungen der zuvor genannten sekundären Kupferminerale modelliert und mit natürlichen Paragenesen verschiedener Erzlagerstätten verglichen.

Die Bildung von Lirokonit, in seiner Typlokalität in Wheal Gorland, Cornwall, UK, benötigt neutrale Wässer in einer Al-reichen Umgebung, welche arm an Fe, Pb oder anderen interferierenden Metallen ist. Im Gegensatz dazu sind Geminit und Pushcharovskit Minerale welche sich typischerweise unter sauren Bedingungen bilden, wo generell keine Karbonate vorhanden sind und wenn doch, dann nur akzessorisch. Zusätzlich zu den Untersuchungen der

Tabelle 1. Thermodynamische Eigenschaften der untersuchten Phasen. Alle Enthalpien und Gibbsche freie Energien sind in kJ·mol^{-1}, alle Entropien sind in J·mol^{-1}·K^{-1}.

	$\Delta_f H^\circ$	S^o	$\Delta_f S^\circ$	$\Delta_f G^\circ$	log K_{sp}
Lirokonit (natürlich)	–3516.6±9.1	401.1±4.8	–1745.1±4.9	–2996.3±9.2	–4.92
Lirokonit (Schätzung für das phosphat-freie Endglied)				–2931.6	–4.85
Pushcharovskit	–1250.5±3.0	176.4±2.1	–718.0±2.3	–1036.4±3.8	–17.21
Geminit (natürlich)	–1110.4±3.0	158.2	–619.5	–925.7±3.2	–18.58
Geminit (synth.)	–1111.4±3.0	158.2	–619.5	–926.7±3.2	–18.75
Adamit	–1401.7±3.2	160.1±0.5	–537.1±1.0	–1247.6±3.4	–10.90
Zinkolivenit	–1211.6±3.2	159.5±0.5	–529.6±1.0	–1053.7±3.4	–13.33
Olivenit	–997.3±3.2	158.9±0.5	–521.3±1.0	–841.9±3.4	–15.30
Libethenit	–1384.4±3.2	163.4±0.5	–522.2±1.0	–1228.7±3.4	–16.86

Bildungsbedingungen wurde die Kristallstruktur von Lirokonit mittels Einkristall-Diffraktometrie verfeinert und die Positionen der H-Atome, welche vorher nicht bekannt waren, wurden bestimmt.

Für die Olivenit–Libethenit Mischkristallreihe zeigen die Einheitszellenparameter sowie die Banden der Infrarotspektroskopie eine Entwicklung entsprechend der Größe der ionischen Radien von Phosphor zu Arsen. Die berechneten ΔH^{MIX} Werte sind positiv für alle Werte von X_{lib} mit einem Maximum bei $X_{lib} = 0.59$ und einem deutlichen Schritt zwischen $X_{lib} = 0.69$ und 0.79, welcher eine Änderung in der Kristallstruktur von monoklin (Olivenit) zu orthorhombisch (Libethenit) indiziert. Zusammen mit den thermodynamischen Exzesseigenschaften der Olivenit–Libethenit Mischreihe zeigen die Ergebnisse, dass eine komplette Mischkristallreihe ohne Mischungslücke existiert, wobei der Einbau von Phosphor gegenüber Arsen bevorzugt wird.

Der dritte Teil dieser Arbeit konzentriert sich auf die isotopische Fraktionierung von Kupfer-, Sauerstoff- und Wasserstoff-Isotopen zwischen Malachit und wässriger Lösung. Dies wurde durch Ausfällungsexperimente über den Temperaturbereich von 10 bis 65 °C bestimmt. Die ausgefallenen Feststoffe wurden mittels Pulverröntgendiffraktometrie, Infrarotspektroskopie und thermogravimetrischer Analysen charakterisiert und bestanden aus einer einzigen Phase $Cu_2CO_3(OH)_2$, entsprechend dem Mineral Malachit. Die isotopischen Fraktionierungsfaktoren für Sauerstoff und Wasserstoff konnten wegen einer nichtlinearen Änderung der Isotopenwerte bei etwa 40 °C, in zwei Temperaturbereiche (10-35 °C und 45-65 °C) (Tabelle 2) eingeteilt werden. Diese Änderung hängt mit der anfänglichen Ausfällung von Georgeit (röntgenamorphes $Cu_2CO_3(OH)_2$) zusammen und dem damit verbundenen isotopischen Austausch zwischen diesem Mineral und dem sich daraus bildenden Malachit. Der isotopische Fraktionierungsfaktor für Kupfer ist über den ganzen Temperaturbereich (10-65 °C) (Tabelle 2) definiert, mit einer eindeutigen temperaturabhängigen Fraktionierung und einer durchschnittlichen Fraktionierungsverschiebung $\Delta^{65}Cu_{sol\text{-}mal} = -0.16 \pm 0.05$ ‰. Diese Fraktionierungsverschiebung impliziert, dass chemische Reaktionen von Mineralen, ohne Änderung des Redoxzustandes, nur eine geringfügige Kupferisotopenfraktionierung hervorbringen. Mit der Anwendung der Fraktionierungsfaktoren von Sauerstoff und Wasserstoff für Malachit auf Wasser von der meteorischen Wasserlinie, war es möglich, die „Malachitlinie“ zu berechnen, welche die isotopische Zusammensetzung von Malachit darstellt, der aus einem solchen Wasser ausfallen würde. Zusätzlich wurde der berechnete Fraktionierungsfaktor von Sauerstoff und Wasserstoff

Tabelle 2. Werte für A und B der Gleichung für die isotopischen Fraktionierungsfaktoren von Sauerstoff, Wasserstoff und Kupfer in der Form 1000 ln α = A ($10^6/T^2$) + B, der Temperatur T in Kelvin.

	Temperatur-bereich	A	B
$Sauerstoff_{Georgeit\text{-}Lösung}$	10 – 35 °C	2.705 ± 0.156	4.064 ± 1.785
$Sauerstoff_{Malachit\text{-}Lösung}$	45 – 65 °C	2.866 ± 0.328	0.957 ± 3.055
$Wasserstoff_{Georgeit\text{-}Lösung}$	10 – 35 °C	0.214 ± 0.473	–27.473 ± 5.519
$Wasserstoff_{Malachit\text{-}Lösung}$	45 – 65 °C	–1.472 ± 0.607	–22.294 ± 5.651
$Kupfer_{Lösung\text{-}Malachit}$	10 – 65 °C	0.033 ± 0.013	–0.185 ± 0.136

dazu verwendet, um die sauerstoff- und wasserstoffisotopische Zusammensetzung der Bildungswässer der natürlichen Malachit-Proben von Lokalitäten weltweit zu bestimmen und mit der isotopischen Zusammensetzung von Regenwässern nahegelegener Stationen zu vergleichen. Zusammen mit den Kupferisotopen der natürlichen Malachit-Proben kann man annehmen, dass alle untersuchten Malachite supergene Proben sind, welche sich aus meteorischem Wasser bildeten.

Table of content

Selbstständigkeitserklärung IV

Acknowledgement V

Abstract VI

Kurzfassung VIII

Table of content XI

List of figures XIV

List of tables XVIII

List of symbols and abbreviations XX

1 General introduction 1

1.1 Ore deposits 2

1.1.1 Structure of an ore deposit 2

1.1.2 Phosphates and arsenates 4

1.1.3 Copper 5

1.2 Motivation and scope of the work 7

2 Thermodynamic properties, crystal structure and phase relations of pushcharovskite [$Cu(AsO_3OH)(H_2O)\cdot 0.5H_2O$], geminite [$Cu(AsO_3OH)(H_2O)$] and liroconite [$Cu_2Al(AsO_4)(OH)_4\cdot 4H_2O$] 8

2.1 Abstract 9

2.2 Introduction 10

2.3 Materials 11

2.4 Methods 12

2.5 Results 14

2.5.1 Crystal structure and hydrogen-bonding network in liroconite 19

2.5.2 Enthalpies of formation 21

2.5.3 Low-temperature heat capacity and entropies 23

2.5.4 Gibbs free energies of formation and solubility products 25

2.5.5 Thermodynamics of the endmember liroconite 25

2.6 Discussion 26

2.6.1 Liroconite: associated minerals and thermodynamic models 26
2.6.2 Geminite: associated minerals and thermodynamic models 31
2.6.3 Pushcharovskite: associated minerals and thermodynamic models 35
2.7 Acknowledgements 35
3 Thermodynamic properties and crystal structure of adamite [$Zn_2(AsO_4)(OH)$], zincolivenite [$CuZn(AsO_4)(OH)$] and the solid solution series olivenite [$Cu_2(AsO_4)(OH)$] – libethenite [$Cu_2(PO_4)(OH)$] 37
3.1 Abstract 37
3.2 Introduction 38
3.3 Materials 39
3.4 Methods 40
3.5 Results and discussion 41
3.5.1 Structure and composition of end members 42
3.5.2 Structure and composition of the olivenite–libethenite solid solution 44
3.5.3 Thermodynamic properties of end members 46
3.5.4 Thermodynamic properties of the olivenite–libethenite solid solution 49
3.6 Conclusion 53
3.7 Special explanatory notes 54
3.8 Acknowledgements 54
4 Fractionation of copper, oxygen and hydrogen isotopes between malachite and aqueous phase 55
4.1 Abstract 56
4.2 Introduction 57
4.3 Materials 58
4.3.1 Natural malachite samples 59
4.4 Methods 60
4.5 Results 61
4.5.1 Transient phase during the synthesis of our samples 62
4.5.2 Isotopes 64
4.6 Discussion 67

4.6.1 Isotopic fractionation of Cu carbonate phases at various temperatures 67
4.6.2 Isotopic composition of natural samples 71
4.7 Summary and conclusion 74
4.8 Acknowledgements 75
5 Exposition of the results and perspective 76
5.1 Major conclusions and key findings 76
5.1.1 Thermodynamic properties 76
5.1.2 Crystal structures of the olivenite-libethenite series 80
5.1.3 Isotopic studies of malachite 80
5.2 Future perspectives 81
6 References 82
7 Appendix ..... A

List of figures

Figure 1-1. Generalized representation of the zones which may be developed in an oxidizing base metal orebody. 2

Figure 1-2. pH-pε phase diagram showing the stability of dissolved arsenic species in the supergene environment. T = 25 °C, P = 1 atm, log a[As(V)] = -4..... 4

Figure 1-3. pH-pε phase diagram for a suite of of secondary copper minerals, including malachite, showing the stability of dissolved copper species and copper minerals in the supergene environment. Conditions shift vertically from the more reducing, saturated zone in middle blue at the bottom (below the water table), to the more oxidizing conditions towards the top of the profile (vadose zone, where the soil and rock pores contains air as well as water). T = 25 °C, log a[Cu(II)] = -4, log a[S(-II)] = -5, log a[Fe(III)] = -4, log f_{CO2} = -2.5. Self calculated and modified after Sillitoe (2013) and Reich and Vasconcelos (2015)..... 5

Figure 2-1. FT-IR spectrum of pushcharovskite. Bands are marked with their positions in cm^{-1}. 18

Figure 2-2. Thermogravimetric analysis of pushcharovskite. The extrema in the heat flow are labelled with the corresponding temperature (°C). Two separate runs were stopped at temperatures, marked by circles on the heat flow curve, and the products were investigated by pXRD. Details are in the text..... 19

Figure 2-3. Hydrogen bonding in the structure of liroconite: Cu/Al – octahedrally coordinated cations; Wa – H_2O molecule; OH – hydroxyl group; ---> H bond; bond strengths are given in valence units (vu)..... 20

Figure 2-4. Low-temperature heat capacity of pushcharovskite and liroconite. Circles show the measured data, and the curves are the polynomials used for fitting. 23

Figure 2-5. Liroconite growing on greenish scorodite. b) Ceruleite (spherical aggregates) with liroconite crystals. c) Liroconite overgrown by azurite crystals. d) Pseudomorphs of cornwallite after liroconite. e) Clinoclase growing on liroconite. f) crystals with chalcophyllite (greenish tabular crystals). All samples from Wheal Gorland, England.27

Figure 2-6. Solubilities of some common Al-Fe minerals, compared to the Al(III) concentrations needed to stabilize liroconite. All curves are calculated by PHREEQC (Parkhurst and Appelo, 1999). The curve for olivenite –liroconite was calculated by forcing a fluid to be in equilibrium with both phases simultaneously..... 28

Figure 2-7. Stability fields of olivenite+mansfieldite versus liroconite, according to eq. 7 in text. 30

Figure 2-8. a) Geminite crystals on the milky-white quartz. Geschieber vein, Daniel level, Svornost mine, Jáchymov. b) Geminite crystals partially overgrown by bluish lavendulan. Matrix is represented by quartz. Geschieber vein, Daniel level, Svornost mine, Jáchymov. c) Geminite aggregate partially overgrown by bluish yvonite. White fine-grained phase is

arsenolite. Giftkies adit, Jáchymov. d) Geminite crystal in a cavity of strongly altered native arsenic. Octahedral colourless crystals belong to arsenolite. Geister vein, sixth Geister level, Rovnost mine, Jáchymov. Photograph a) by Stephan Wolfsried and b-d) by Pavel Škácha. 32

Figure 2-9. pε-pH diagram of the system CuO-SO_3-CO_2-H_2O for T = 298.15 K, log f(CO_2,g) = –2 and log a(S(VI)) = –2. 33

Figure 2-10. pε-pH diagram of the system CaO-CuO-SO_3-CO_2-H_2O for T = 298.15 K, log a(Cu(II)) = –2.5, log a(S(VI)) = –2.5, log a(HCO^{3-}) = –2. 33

Figure 2-11. pε-pH diagram of the system CuO-As_2O_5-H_2O for T = 298.15 K, log f(CO_2,g) = –2, log a(As(V)) = –2, olivenite is suppressed from the calculations. 34

Figure 3-1. FT-IR spectra of the end members libethenite, olivenite, zincolivenite and adamite. 43

Figure 3-2. Powder XRD patterns of the solid solution series olivenite-libethenite. e.g. 20P80As = $Cu_2(PO_4)_{0.2}(AsO_4)_{0.8}(OH)$ 43

Figure 3-3. Evolution of the lattice parameters and cell volume for $Cu_2(PO_4)_x(AsO_4)_{1-x}(OH)$ [0≤x≤1] from Rietveld refinement (error bars are smaller than symbols). 44

Figure 3-4. FT-IR spectra of the solid solution series olivenite-libethenite. e.g. 20P80As = $Cu_2(PO_4)_{0.2}(AsO_4)_{0.8}(OH)$ 45

Figure 3-5. Positions of a) absorption maxima around 545 cm^{-1} and b) asymmetric stretching vibrations of the PO_4 groups in the FT-IR spectra of members of the olivenite–libethenite solid solution series. 46

Figure 3-6. Excess volume of solid solution olivenite [$Cu_2(AsO_4)(OH)$] – libethenite [$Cu_2(PO_4)(OH)$]. The dashed line indicates ideal mixing. 49

Figure 3-7. Excess enthalpy of solid solution olivenite [$Cu_2(AsO_4)(OH)$] – libethenite [$Cu_2(PO_4)(OH)$]. The dashed line indicates ideal mixing. 50

Figure 3-8. Gibbs free energy of mixing of solid solution olivenite [$Cu_2(AsO_4)(OH)$] – libethenite [$Cu_2(PO_4)(OH)$]. The dashed line indicates ideal mixing. 51

Figure 3-9. Compositional variability of the members of the composition $M_2(XO_4)(OH)$ (M = Cu, Zn; X = P, As). Our data are shown as blue points and data from literature as shaded areas. Literature data from: Southwood et al. (2020), Majzlan et al. (2015), Braithwaite et al. (2009), Sejkora et al. (2008), Williams et al. (2006), Sejkora et al. (2006), Gołębiowska et al. (2006), Szakáll et al. (1994). Modified after Andersen and Moulding (2009). 53

Figure 4-1. FT-IR spectra of malachite and georgeite, both $Cu_2CO_3(OH)_2$. Bands are marked with their positions in cm^{-1}. 62

Figure 4-2. Thermogravimetric analysis of malachite. The extrema in the heat flow are labelled with corresponding temperature (in °C). 62

Figure 4-3. Isotopic values of a) deuterium (-62.04 ± 1.85 ‰) b) oxygen (-9.11 ± 0.63 ‰) and c) copper (0.4 ± 0.05‰) of the synthesized malachite samples. (Values of starting solution in brackets)..... 63

Figure 4-4. Mineral-solution oxygen isotope fractionation as a function of temperature for this study's results and for comparison, Melchiorre et al. (1999) experiment. 64

Figure 4-5. Mineral-solution hydrogen isotope fractionation as a function of temperature for this study's results. 65

Figure 4-6. Solution-malachite copper isotope fractionation as a function of temperature for this study's results. 66

Figure 4-7. Comparison of our mineral-solution oxygen isotope fractionation factors with carbonate-H_2O factors, all plotted as a function of temperature. ($CaCO_3$, $SrCO_3$, $BaCO_3$: Friedman and O'Neil, 1977; $FeCO_3$: Carothers et al., 1988; $Cu_3(CO_3)_2(OH)_2$: Melchiorre et al., 2000; $PbCO_3$: Melchiorre et al., 2001, $BaMg(CO_3)_2$: Bötcher, 2000, details in appendix) 67

Figure 4-8. Comparison of our mineral-solution hydrogen isotope fractionation factors with mineral-H_2O factors, all plotted as a function of temperature. ($Mg(OH)_2$: Xu and Zheng, 1999; $Mg_6Si_4O_{10}(OH)_8$: Wenner and Taylor, 1973; $Al_4Si_4O_{10}(OH)_8$: Gilg and Sheppard, 1996; $CaSO_4 \cdot 2H_2O$: Fontes and Gonfiantini, 1967; $CuSO_4 \cdot 5H_2O$: Heinzinger, 1969; $Al(OH)_3$: Vitali et al., 2001; details in appendix) 68

Figure 4-9. $\Delta^{65}Cu$ values that show the relative difference of original reactant to final product. More details in text. 69

Figure 4-10. $\delta^{18}O$ vs. δD diagram, with the isotopic values of the malachite samples (black symbols) and their respective calculated parental waters (blue symbols). Meteoric water line after Craig (1963)..... 71

Figure 4-11. Comparison of the rain water (GNIP) and the expected values of the malachite fparental water of δD (a) and δ18O (b) (error bars in y-direction are smaller than data points). 72

Figure 4-12. $\delta^{18}O$ vs. δD for the natural malachite samples with the calculated "malachite line" at different temperatures. The line "kaolinite" indicates the isotopic variations shown by kaolinites from surface weathering environments Savin and Epstein (1970)..... 73

Figure 5-1. a) pH-pε phase diagram for a suite of copper and zinc minerals, including copper phosphates, arsenates and zinc arsenates. T = 25 °C, log a[Cu(II)] = -4, log a[Zn(II)] = -4, log a[P(V)] = -5, log a[As(V)] = -4, log a[S(-II)] = -5. b) sketch of a) for better visibility of the stability fields of the minerals of interest..... 78

Figure 5-2. Activity-activity phase diagram for copper and zinc arsenates. T = 25 °C, log a[As(V)] = -4, pH = 6..... 79

Figure 5-3. Activity-activity phase diagram for copper phosphates, arsenates and tenorite. T = 25 °C, log a[Cu(II)] = -4, pH = 6. (self calculated after Majzlan et al., 2015) 79

List of tables

Table 1-1. Some secondary copper(II) and zinc(II) minerals. (e.g. Anthony et al., 2000) 3
Table 2-1. Unit cell parameters for geminite and pushcharovskite from this work, compared to values from studies on natural material. 14
Table 2-2. Crystal data, collection and refinement parameters for liroconite. 15
Table 2-3. Atom coordinates and equivalent and anisotropic displacement parameters for liroconite. 16
Table 2-4. Selected interatomic distances (Å) and polyhedral-distortion measures in the structure of liroconite. 17
Table 2-5. Bond-valence analysis of the liroconite crystal structure. 17
Table 2-6. Electron microprobe analysis of liroconite. 18
Table 2-7. Hydrogen-bond geometry (in Å and °) in the structure of liroconite. 20
Table 2-8. Thermodynamic properties of the studied phases. 21
Table 2-9. Thermochemical cycle for the studied minerals. 22
Table 2-10. Molar thermodynamic functions for pushcharovskite, $Cu(AsO_3OH)(H_2O)\cdot 0.5H_2O$, molecular mass 230.4945 $g\cdot mol^{-1}$. 24
Table 2-11. Molar thermodynamic functions for liroconite, $Cu_2Al[(AsO_4)_{0.83}(PO_4)_{0.17}](OH)_4\cdot 4H_2O$, molecular mass 425.6088 $g\cdot mol^{-1}$. 24
Table 3-1. Calculated quantities of reagents necessary for the synthesis of the olivenite-libethenite solid solution. H_2O = deionized water. 39
Table 3-2. Unit cell parameters for olivenite $[Cu_2(AsO_4)(OH)]$, libethenite $[Cu_2(PO_4)(OH)]$, adamite $[Zn_2(AsO_4)(OH)]$ and zincolivenite $[CuZn(AsO_4)(OH)]$ from this work, compared to values from studies on natural material. 41
Table 3-3. ICP-OES analyses of the end members adamite and zincolivenite as well as the solid solution series olivenite–libethenite. 42
Table 3-4. Unit cell parameters for the solid solution series olivenite–libethenite. 44
Table 3-5. Thermochemical cycle for the studied minerals. x = P/(P+As). All enthalpies in $kJ\cdot mol^{-1}$. 47
Table 3-6. Thermodynamic properties of the end members adamite, zincolivenite, olivenite and libethenite. 48
Table 3-7. Gibbs free energy of formation and solubility products of the end members adamite, zincolivenite, olivenite and libethenite from this work and other researchers. 48
Table 3-8. Enthalpies of dissolution and thermodynamic properties of mixing of the solid solution olivenite $[Cu_2(AsO_4)(OH)]$ – libethenite $[Cu_2(PO_4)(OH)]$ 51
Table 4-1. Overview of the syntheses with sample names, duration of the syntheses, temperature set and the average of the measured temperature. 58

Table 4-2. Unit-cell parameters for synthetic malachite in comparison with specimen from Schwarzenberg, Saxony, Germany (Süsse, 1967). 61

Table 4-3. Values for A and B of the equation for the isotopic fractionation factors of oxygen and hydrogen in the form of 1000 ln α = A (10^6 / T^2) + B, with T the temperature in Kelvin. 65

Table 4-4. Isotopic composition of the natural malachite samples. *calculated. 66

Table 4-5. Overview of the fractionation pairs of Δ^{65}Cu values and the experimental methods. 70

Table 4-6. Natural malachite locations of the rain water measuring stations of GNIP for the comparison. 74

Table 5-1. Overview of minerals mentioned in this chapter, together with their formula. 77

Table 7-1. Comparison of our mineral-solution **oxygen** isotope fractionation factors with carbonate-H_2O factors, all plotted as a function of temperature. .....A

Table 7-2. Comparison of our mineral-solution **hydrogen** isotope fractionation factors with mineral-H_2O factors, all plotted as a function of temperature. .....A

List of symbols and abbreviations

Symbols

Acronym	Description	Unit
$\alpha_{A\text{-}B}$	fractionation factor between A and B	-
$a(X)$	activity of species X	-
C_p	heat capacity	[J·mol^{-1}·K^{-1}]
δ_A	isotopic delta value of A	[‰]
D_{calc}	density, calculated	[g·cm^{-3}]
ΔG^{EX}	excess free energy of mixing	[kJ·mol^{-1}]
ΔG^{MIX}	free energy of mixing	[kJ·mol^{-1}]
$\Delta_f G^o$	Gibbs free energy of formation	[kJ·mol^{-1}]
$\Delta_r G^o$	Gibbs free energy of reaction	[kJ·mol^{-1}]
ΔH	enthalpy	[kJ·mol^{-1}]
ΔH^{EX}	excess enthalpy of mixing	[kJ·mol^{-1}]
ΔH^{MIX}	enthalpy of mixing	[kJ·mol^{-1}]
$\Delta_f H^\circ$	enthalpy of formation	[kJ·mol^{-1}]
K	equilibrium constant	-
log K_{sp}	solubility product	-
Q	reaction quotient	-
ΔS^{EX}	excess entropy of mixing	[J·mol^{-1}·K^{-1}]
ΔS^{MIX}	entropy of mixing	[J·mol^{-1}·K^{-1}]
S°	standard entropy	[J·mol^{-1}·K^{-1}]
$\Delta_f S°$	entropy of formation	[J·mol^{-1}·K^{-1}]
T	temperature	[K]
t	time	[s]
V	cell volume	[Å^3]
ΔV^{EX}	excess molar volume	[Å^3]
ΔV^{MIX}	molar volume of mixing	[Å^3]

Abbreviations

apfu	atoms per formula unit
BV	Bond-valence
CIF	crystallographic information file
DSC	differential scanning calorimetry
FT-IR	Fourier-transformed infrared spectroscopy
FWHM	full width at half maximum
GOF	Goodness of fit
GMWL	Global Meteoric Water Line
ICP-OES	inductively coupled plasma – optical emission spectroscopy
pXRD	powder X-ray diffraction
SG	Space group
SMOW	Standard Mean Ocean Water
TGA	thermogravimetric analysis

Mineral abbreviations (after Whitney and Evans, 2010)

* - labelled by myself

Ad	Adamite*
Bn	Bornite
Cct	Chalcocite
Ccp	Chalcopyrite
Cu	Copper*
Cv	Covellite
Cpr	Cuprite
Lib	Libethenite*
Mlc	Malachite
Oli	Olivenite*
Orp	Orpiment
Psm	Pseudomalachite*
Rg	Realgar
Sp	Sphalerite
Tnr	Tenorite
Zno	Zincolivenite*

1 General introduction

The Earth's complex outer layer of air, water, biota, organic matter and minerals is a critical zone where combinations of geological, chemical, physical and biological processes operate together on pre-existing metal-bearing rocks to form supergene metal deposits. Oxidation zones of supergene ore deposits have a large mineralogical diversity and can help for the understanding of the history of ore deposits. Apart from being an important window into the geological past of ore bodies and the interaction history between ores, country rocks, aqueous solutions of various origin and living organisms, supergene ores are also important for the economics of a region. Supergene ores are hosts for economically important metals (e.g., Kampunzu et al., 2009; Borg, 2015) which leads to exploration and mining. Draining from mineralized and mined areas may have high dissolved metal and toxic heavy metals concentrations (e.g. Cu, Pb and Hg) as well as metalloids (e.g As and Se) (Bowell and Craw, 2014; Reich and Vasconcelos, 2015). Such enriched waters can contaminate aquifers and cause poisoning of communities using drinking water from these aquifers (e.g., Smedley and Kinniburgh, 2002; Lee et al., 2005; Wongsasuluk et al., 2014).

For all these processes minerals are the most important subject. Minerals store and release elements and therefore exert control on solubility of harmless and toxic ions. They provide surface for organisms which can change, for example, their solubility behaviour and isotopic fractionation of elements (Mathur et al., 2005). Secondary minerals play an important role in the uptake and release of such ions. Crystallization of secondary minerals may be thought of as a 'metal-buffering' process between ores and species able to migrate freely in groundwater (Williams, 1990). Hence, the ability to predict the fate of oxidation zones is limited due to the complexibility of minerals and all parameters that are involved in changing the behaviour of them, like temperature, pH, chemical potential (Eh), organisms, and more.

Around one third of all minerals occur in oxidation zones (Williams, 1990) and variability in the chemical composition and crystal chemical properties of secondary copper minerals lends them for the understanding of the formation and evolution of oxidation zones of ore deposits. Secondary minerals in ore deposits are commonly carbonates, sulfates, phosphates and arsenates. We chose copper and arsenic because both are potential contaminants for the environments and secondary copper arsenic minerals are a large and variable group with still some gaps in knowledge. "Copper(II) is the most versatile" element in terms of its "elaborate stoichiometric variations with commonly available counter ions" (Williams, 1990). As a result, there is an astonishing variability of secondary copper minerals. Also arsenic is widely distributed in the environment and is used for industrial, agricultural, medical and other purposes but has also a toxic effect on a variety of organisms, including humans (Bowell et al., 2014; Mitchell, 2014; Plant et al., 2014). The understanding of mechanisms of arsenic behaviour in the near surface conditions is one of the actual problems of modern mineralogy and geochemistry and it is very important for the solving

of some environmental problems. Additionally, copper arsenates are not only capable of taking up and releasing copper and arsenic but also other elements such as lead, zinc and phosphor. These processes can negatively influence the natural environment, from microscopic life forms up to humans. Therefore, we want to enhance the understanding of the processes that form secondary copper minerals.

1.1 Ore deposits

Ore deposits are always complex assemblages of many different mineral species and are formed by a variety of geological processes. One common way to classify ore deposits is after the processes of formation after Lindgren (1933) (modified 1985; Guilbert and Park, 2007). The primary subdivision is into chemical and mechanical processes of concentration with the chemical processes further divided into groups according to the place of deposition of minerals. All ores forming through these processes in different places are primary ores. Supergene ores are in most cases formed as a result of the reaction between meteoric waters, host rocks and primary ores, through chemical processes and mineral reactions of weathering. Therefore, supergene ore deposits form when chemical weathering promotes the dissolution, remobilization and re-precipitation of elements of economic interest at or near the Earth's surface. The rates of these reactions are invariably dependent of the climate, reflecting ambient temperature and availability of liquid water, organic or inorganic redox system and parent material (Vasconcelos et al., 2015; Dill, 2015). The most abundant reagent and reaction medium in the supergene zone is water, as gas or liquid. Given the widespread nature of carbonate species in groundwater, it is not surprising to discover that secondary carbonate minerals, especially those of the more common base metals, such as copper, lead and zinc, are frequently found in oxide zones of orebodies. Malachite is one of the most common secondary minerals of those carbonates. The wall rock composition is also influencing the type of minerals that are forming and the zonation of metals and minerals.

1.1.1 Structure of an ore deposit

The upper most part of an ore deposit, closest to or even on the Earth's surface, is the so called "Gossan" (Fig.1-1). Here the most chemically resistant primary phases remain, including quartz, zircon and also residual minerals like oxides of manganese and iron (hematite and goethite). Beneath is the leached zone with

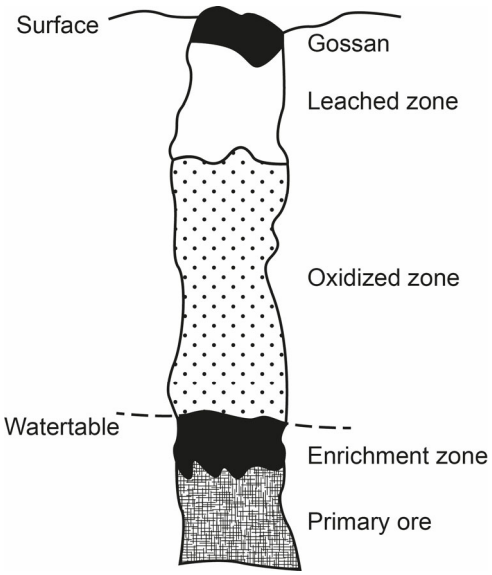

Figure 1-1. Generalized representation of the zones which may be developed in an oxidizing base metal orebody.

sulfides and sulfosalts which are essentially insoluble in aqueous solution (with a few exceptions). With the exposure to weathering processes, the electrochemical oxidation of the primary sulfides starts, e.g. Cu(0) to Cu(II), and the released metals will be transported as soluble species (e.g. $CuSO_4$).

Consequently, the groundwater is charged with various metallic cations and complexes together with other aqueous species, including carbonate and bicarbonate, sulfate, phosphate, arsenate and other anionic species. Additionally, it is enriched with oxygen which then reacts with the above mentioned aqueous species and new mineral phases precipitate: the secondary minerals of the oxidized zone of orebodies (Fig.1-1). In this environment, the temperature and pressure deviate little from atmospheric conditions, oxygen is abundant and water freely available. It is to mention that the anion set available for the precipitation of secondary minerals is reasonably limited and is therefore a limiting factor for the formation of secondary minerals.

The water table represents the border between oxidizing and reducing conditions. In the enrichment zone, the oxygen in the groundwater is exhausted and solutions have become more reducing in nature. Supergene sulfides, like covellite (CuS) and chalcocite (Cu_2S), are characteristic for the enriched zone.

The lowest part of an ore body consists of the primary environment with the unaltered primary mineralization. More or less elevated temperatures and pressures with respect to ambient conditions predominate this environment with a low concentration of oxygen which makes it rather reducing than oxidizing.

Table 1-1. Some secondary copper(II) and zinc(II) minerals. (e.g. Anthony et al., 2000)

Oxides	Cuprite	Cu_2O
	Tenorite	CuO
Sulfates	Antlerite	$Cu_3SO_4(OH)_4$
	Brochantite	$Cu_4SO_4(OH)_6$
	Chalcanthite	$CuSO_4 \cdot 5H_2O$
Carbonates	Malachite	$Cu_2CO_3(OH)_2$
	Azurite	$Cu_3(CO_3)_2(OH)_2$
Silicate	Chrysocolla	$Cu_2H_2SiO_5(OH)_4 \cdot nH_2O$
Arsenates	Olivenite	$Cu_2AsO_4(OH)$
	Cornwallite	$Cu_5(AsO_4)_2(OH)_4$
	Clinoclase	$Cu_3AsO_4(OH)_3$
	Geminite	$Cu(AsO_3OH)(H_2O) \cdot H_2O$
	Pushcharovskite	$Cu(AsO_3OH)(H_2O) \cdot 0.5H_2O$
	Köttigite	$Zn_3(AsO_4)_2 \cdot 8H_2O$
	Adamite	$Zn_2AsO_4(OH)$
	Paradamite	$Zn_2AsO_4(OH)$
	Legrandite	$Zn_2AsO_4(OH) \cdot H_2O$
	Liroconite	$Cu_2Al(AsO_4)(OH)_4 \cdot 4H_2O$
Phosphates	Libethenite	$Cu_2PO_4(OH)$
	Pseudomalachite	$Cu_5(PO_4)_2(OH)_4$
	Cornubite	$Cu_3PO_4(OH)_3$
	Hopeite	$Zn_3(PO_4)_2 \cdot 4H_2O$
	Tarbuttite	$Zn_2PO_4(OH)$

1.1.2 Phosphates and arsenates

A great number of minerals containing phosphate and arsenate ions are reported from the oxidized zone of base metal orebodies (Williams, 1990). Phosphorous in oxidation state V, as phosphate ion PO_4^{2-}, is stable over a remarkable range of redox conditions. Arsenic has quite a different redox stability. In the primary environment, the primary ore, arsenic containing minerals in general contain arsenic(III) ions with arsenopyrite as most abundant mineral. These species, containing As(III) are not stable in oxidation zones. The oxidation of arsenides and arsenic-containing sulfosalts results in formation of arsenites (AsO_3^{3-}) and arsenate (AsO_4^{3-}) oxyanions, which are unknown in the primary environment. Those are more soluble compounds which lead to an increase in the As concentration in the groundwater. An overwhelming majority of arsenate minerals but also As(III) containing minerals are found in the supergene zone (Fleischer and Mandarino, 1995; Bowell et al., 2014; Majzlan et al., 2014b).

The solubility behaviour plays the most important role in determining the nature of common secondary phosphate and arsenate minerals. Redox potential (Eh) and pH are the most important factors controlling As speciation in natural environments (Smedley and Kinniburgh, 2002). Under oxidizing conditions, $H_2AsO_4^-$ is predominant in acidic waters (less than pH 6.9), while in alkaline waters $HAsO_4^{2-}$ is predominant (Fig. 1-2). Therefore, secondary-As minerals are generally sensitive to changes in both Eh and pH. Phosphates and arsenates containing Cu(II) and Zn(II) ions, next to Pb(II), are often found in the oxide zone of ore bodies, also common are secondary iron-containing species (Palache et al., 1951). Some species are listed in Table 1-1. In the secondary phosphates and arsenates of these metals are solid solution phenomena omnipresent. The mimetite–pyromorphite ($Pb_5(AsO_4)_3Cl$–$Pb_5(PO_4)_3Cl$) series as well as the cornwallite–

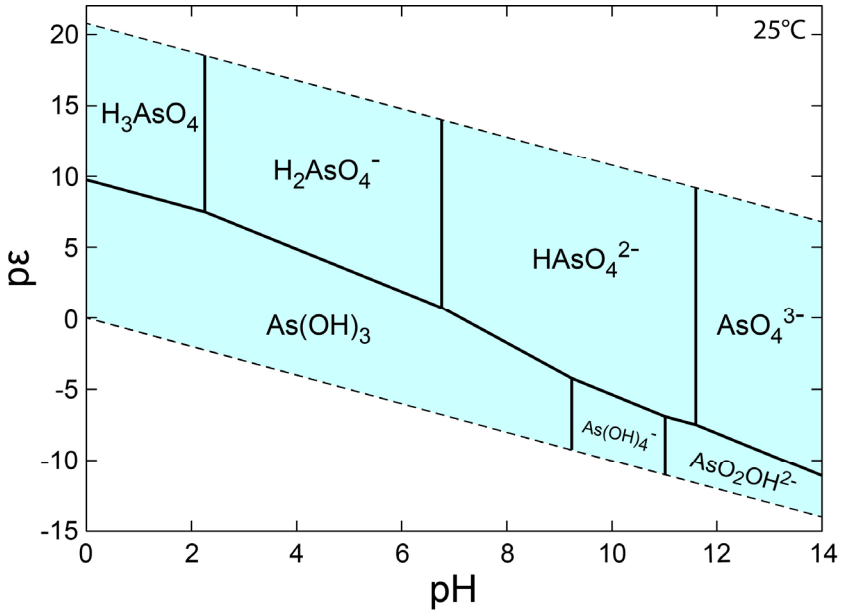

Figure 1-2. pH-pε phase diagram showing the stability of dissolved arsenic species in the supergene environment. T = 25 °C, P = 1 atm, log a[As(V)] = -4.

pseudomalachite ($Cu_5(AsO_4)_2(OH)_4$–$Cu_5(PO_4)_2(OH)_4$) series are two well-known examples of a complete arsenate–phosphate solid solution (Markl et al., 2014; Ciesielczuk et al., 2016). Solid solutions are not only found between the anion sites, but also to substitutions involving one or more of the cations. One example for this is the libethenite group (Strunz and Nickel, 2001) with a general formula $M_2(XO_4)(OH)$ (M = Cu, Zn; X = P, As). Extensive substitutions are known in this quaternary system (e.g., Braithwaite, 1983; Anthony et al., 2000; Braithwaite et al., 2005), for example with olivenite, $Cu_2(AsO_4)(OH)$, being frequently phosphatian with up to 15 mol% P (Braithwaite, 1983) and in other environments with up to 20 mol% of Zn (Southwood et al., 2020). Already in 1956, Guillemin suggested that a continuous solid solution might exist between olivenite and libethenite but no complete solid solution series is found in natural samples until today (see Chapter 3).

1.1.3 Copper

Copper is generally leached from ore above the water table by downward percolating groundwater so that upper levels of ore deposits are thus depleted in Cu (leached zone) (Ridley, 2013). The degree of leaching is controlled by acidity since the solubility of Cu is dependent on pH. Copper is then concentrated within the subjacent oxide zone. This mineralogically and compositionally complex layer is composed of a great amount of different copper minerals including oxides, sulfates, hydroxy-chlorides, carbonates, silicates, arsenates and phosphates. Some selected minerals are listed in Table 1-1.

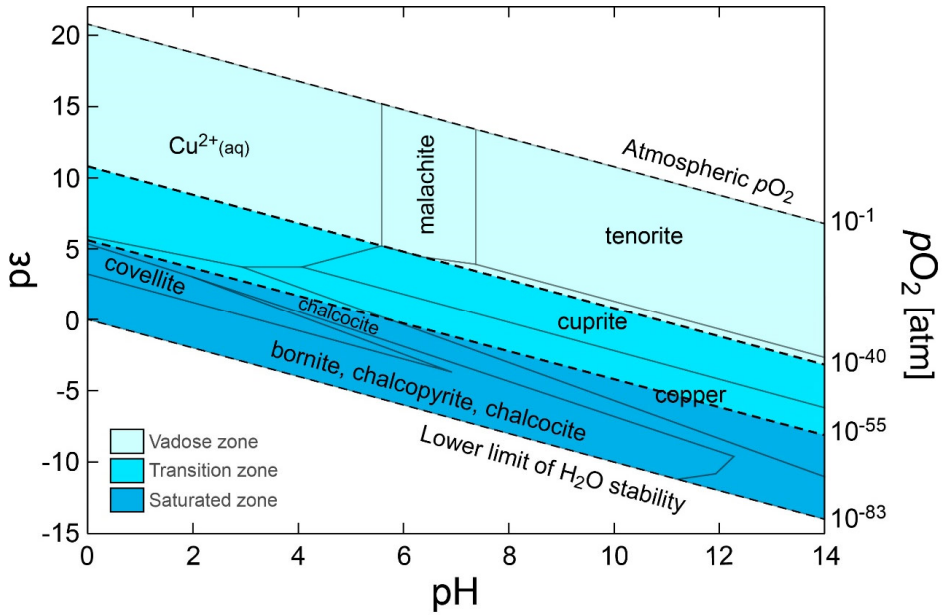

Figure 1-3. pH-pε phase diagram for a suite of of secondary copper minerals, including malachite, showing the stability of dissolved copper species and copper minerals in the supergene environment. Conditions shift vertically from the more reducing, saturated zone in middle blue at the bottom (below the water table), to the more oxidizing conditions towards the top of the profile (vadose zone, where the soil and rock pores contains air as well as water). T = 25 °C, log a[Cu(II)] = -4, log a[S(-II)] = -5, log a[Fe(III)] = -4, log f_{CO2} = -2.5. Self calculated and modified after Sillitoe (2013) and Reich and Vasconcelos (2015).

The precipitation in the oxide zone is largely controlled by the pH and the enclosing rock type (Fig. 1-3). Under more reducing conditions, the remaining Cu in the descending metal- and sulfate-rich solutions will form secondary sulfides in the saturated zone below the water table where free oxygen is almost absent (pO_2 below 10-40 atm) (Fig. 1-3). Malachite, for example, is stable at low temperatures, in slightly acidic conditions.

Other interesting features of copper are its isotopes and the isotopic differences between zones in ore deposits. Copper has two naturally occurring isotopes, ^{63}Cu and ^{65}Cu, with a relative abundance of 69.2% and 31.8%, respectively. In the leach cap, the enrichment zone and fluids of an ore deposit are distinct differences in the mean $\delta^{65}Cu$ value compared to the high temperature sulfides that comprise the primary ores (Mathur and Fantle, 2015). These differences occur due to the oxidative dissolution and precipitation of sulfides which can isotopically fractionate Cu (e.g. Mathur et al., 2005; Kimball et al., 2009).

1.2 Motivation and scope of the work

To get some idea about the mobility and availability of potential elements, it is important to use precise and accurate thermodynamic data, numeric modelling and to know the structure and composition of the minerals. Stability constants and thermodynamic data are available for only a few of the species listed in Table 1-1, mainly the more common ones. Olivenite, clinoclase, and euchroite are a few of the copper arsenates where the thermodynamic data are available. Data for rarer minerals like liroconite and geminite as well as solid solution members of series like olivenite–libethenite are missing.

Therefore, the thermodynamic properties of a suite of endmember copper arsenate (liroconite, geminite, pushcharovskite, olivenite), zinc arsenate (adamite) and copper phosphate (libethenite) minerals as well as of the solid solutions of olivenite–libethenite and olivenite–adamite were determined. For the acquisition of precise thermodynamic data, it is important to have pure phases with no impurities. Consequently, the phases of interest were synthesized under clean conditions and carefully characterized by powder X-ray diffraction, infrared spectroscopy, electron microprobe analysis, thermogravimetric analysis and optical emission spectrometry, as needed. Standard thermodynamic properties were obtained by a combination of acid-solution (enthalpy of formation) and relaxation (entropy) calorimetry. The mixing parameters for selected solid solutions were derived by calorimetry and used to get a better understanding of the exchange mechanisms between As and P. The calculated possible miscibility gaps are critically compared to the composition of natural solid solutions. Additionally, we integrated the thermodynamic data into an internally consistent thermodynamic database to model the evolution of oxidation zones and copper arsenates precipitation with a more expanded database than before. Eh-pH stability relationships will be discussed for some minerals in order to interpret conditions of formation of these minerals. Another factor to understand the formation of secondary minerals are isotopic studies. Therefore, we investigated the isotopic fractionation of copper, hydrogen and oxygen in malachite, a common secondary mineral in the oxidation zone of ore deposits. Since stable isotope characterization can contribute needed information on the formation of malachite by establishing the isotopic composition of the formation waters.

2 Thermodynamic properties, crystal structure and phase relations of pushcharovskite [$Cu(AsO_3OH)(H_2O)\cdot 0.5H_2O$], geminite [$Cu(AsO_3OH)(H_2O)$] and liroconite [$Cu_2Al(AsO_4)(OH)_4\cdot 4H_2O$]

A. M. Plumhoff[1], J. Plášil[2], E. Dachs[3], A. Benisek[3], J. Sejkora[4], M. Števko[4], M. S. Rumsey[5], J. Majzlan[1]

[1]Institute of Geosciences, Friedrich-Schiller University, Burgweg 11, 07749 Jena, Germany
[2]Institute of Physics ASCR, v.v.i., Na Slovance 1999/2, 18221 Praha 8, Czech Republic
[3]Department of Chemistry and Physics of Materials, University of Salzburg, Jakob-Haringer-Strasse 2a, 5020 Salzburg, Austria
[4]Department of Mineralogy and Petrology, National Museum, Cirkusová 1740, 19300 Praha 9, Czech Republic
[5]Department of Mineralogy, Natural History Museum, Cromwell Road, London SW7 5BD, Great-Britain

Submitted to European Journal of Mineralogy, 6th December 2019

Revised 4th March 2020

Accepted 18th March 2020

Published 11th May 2020

The involved co-authors and their contribution to the respective manuscript are listed:

The conceptual design of the experiments evolved in discussion with Juraj Majzlan. I was responsible for the preparation, the conduction of the experiments and the data evaluation. The single X-ray diffraction measurement were done by Jakub Plášil as well as the data evaluation of these X-ray data. Jiří Sejkora collected and processed the electron microprobe analyses. Edgar Dachs and Artur Benisek collected and processed the data of the relaxation and differential scanning calorimetry. The preparation of the manuscript was in my responsibility in close collaboration with all co-authors.

2.1 Abstract

The phases pushcharovskite, geminite, and liroconite were synthesized or acquired and characterized by powder X-ray diffraction, infrared spectroscopy, electron microprobe analysis, thermogravimetric analysis and optical emission spectrometry, as needed. Their thermodynamic properties were determined by a combination of acid-solution calorimetry and relaxation calorimetry, resulting in Gibbs free energies of formation ($\Delta_f G^o$, all values in kJ·mol^{-1}) of –1036.4±3.8 [pushcharovskite, $Cu(AsO_3OH)(H_2O)\cdot 0.5H_2O$] and –926.7±3.2 [geminite, $Cu(AsO_3OH)(H_2O)$]. For the natural liroconite $[Cu_2Al[(AsO_4)_{0.83}(PO_4)_{0.17}](OH)_4\cdot 4H_2O]$, $\Delta_f G^o$ = –2996.3±9.2 kJ·mol^{-1}. The estimated $\Delta_f G^o$ for the endmember $Cu_2Al(AsO_4)(OH)_4\cdot 4H_2O$ is –2931.6 kJ·mol^{-1}. The crystal structure of liroconite was refined (R_1 = 1.96% for 962 reflections with [$I > 3\sigma(I)$]) by single-crystal X-ray diffraction and the positions of H atoms, not known previously, were determined. Liroconite is a rare mineral, except for several localities, notably Wheal Gorland in England. Thermodynamic modelling showed that liroconite will be preferred over olivenite if the Al(III) concentration in the fluid reaches levels needed for saturation with X-ray amorphous $Al(OH)_3$. We assume that such fluids are responsible for the liroconite formation during contemporaneous oxidation of primary Cu–As ores and pervasive kaolinization of the host peraluminous granites. pH had to be kept in mildly acidic (5-6) and the activities of dissolved silica were too low to form dioptase. The main stage with abundant liroconite formation was preceded by an acidic episode with scorodite and pharmacosiderite and followed by a late neutral to mildly basic episode with copper carbonates. Geminite and pushcharovskite, on the other hand, are minerals typical for very acidic solutions. At the studied site in Jáchymov (Czech Republic), extremely acidic water precipitates arsenolite; sulfate is removed by formation of gypsum. Geminite associates with other acidic minerals, such as slavkovite, yvonite, and minerals of the lindackerite group. Pushcharovskite is metastable with respect to geminite and probably converts quickly to geminite under field conditions.

2.2 Introduction

Variability in the chemical composition and crystal chemical properties of secondary copper minerals lends them for the understanding of the formation and evolution of oxidation zones of ore deposits (Magalhães et al., 1986; Magalhães et al., 1988; Williams, 1990). Among others, copper arsenates are also common and widely distributed minerals in such oxidation zones (e.g., Števko et al., 2017; Southwood et al., 2020) where they form through weathering of sulfidic minerals. Copper arsenates are capable of taking up and releasing not only copper and arsenic but also other elements such as lead, zinc and selenium (e.g. Ingwersen, 1990). Release of such elements can lead to deterioration of the natural environment. Thermodynamic and crystallographic data, combined into internally consistent thermodynamic databases, can help to predict and explain the occurrence and assemblages of copper arsenates and associated minerals. Geminite was reported as a new species by Sarp and Perroud (1990) on material from Cap Garonne (Var, France) as $Cu(AsO_3OH)(H_2O)$. Pushcharovskite was described later by Sarp and Sanz-Gysler (1997) on material from the same site with the same ideal chemical composition and space group P-1. They concluded that pushcharovskite is a polymorph of geminite and structurally related to yvonite $[Cu(AsO_3OH)(H_2O)\cdot H_2O]$.

The crystal structure of pushcharovskite was determined by Pushcharovsky et al. (2000) on a sample from the type locality using a synchrotron radiation source. Revision of the chemical data (electron microprobe) after the structure solution and refinement allowed the conclusion that the ideal formula is $Cu(AsO_3OH)(H_2O)\cdot 0.5H_2O$. Hence, pushcharovskite and geminite are not polymorphs but a series of hydrates of $Cu(AsO_3OH)(H_2O)$.

Liroconite was named by Wilhelm Karl von Haidinger in 1825 (Mohs and Haidinger, 1825), and before this it was known as octahedral arsenate of copper (Bournon, 1801). One of the first descriptions of the crystal structure of liroconite was in 1962 as $Cu_2Al[(As_1P)O_4)(OH)_4]\cdot 4H_2O$ by Giuseppetti et al. (1962).

In this work, we report the thermodynamic properties of the copper arsenates pushcharovskite [ideally $Cu(AsO_3OH)(H_2O)\cdot 0.5H_2O$], geminite [$Cu(AsO_3OH)(H_2O)$] and liroconite [$Cu_2Al(AsO_4)(OH)_4\cdot 4H_2O$]. Pushcharovskite and geminite were synthesized in our laboratory and characterized by X-ray powder diffraction, Fourier-transform infrared spectroscopy, thermogravimetric analyses and inductively coupled optical emission spectroscopy. The natural samples of geminite and liroconite were characterized by X-ray powder diffraction and an electron microprobe. Enthalpies of formation were measured by acid-solution calorimetry. Additionally, the standard entropy of pushcharovskite was measured by relaxation calorimetry and combined with the enthalpy of formation to calculate its Gibbs free energy of formation. The standard entropies of geminite and liroconite were estimated. Using the thermodynamic data, we then assign specific conditions of formation to these and associated minerals.

2.3 Materials

Pushcharovskite was synthesized by a modified wet chemical procedure after Majzlan et al. (2015), Guillemin (1956), and Toman (1978). All solutions were prepared with deionized water. The first starting solution for this synthesis was 100 mL of 0.1 M As_2O_5 which was heated to approximately 60 °C so that the arsenic oxide powder dissolved completely. The solution was allowed to cool down and later brought to the desired temperature (20, 30, 40, 50 or 80 °C) for the synthesis. The second starting solution was 100 mL of 0.1 M $Cu(OH)_2$ heated separately to the desired temperature (20, 30, 40, 50 or 80 °C), noting that $Cu(OH)_2$ does not completely dissolve. After reaching the desired temperature, the arsenical solution was poured in to the cupric suspension under constant stirring. The glass beaker with the final mixture was covered with aluminium foil and left in an oven for 60 minutes. The resulting suspension was filtered hot and washed several times with deionized water. This synthesis is sensitive to temperature; its sensitivity to the cover is also peculiar. If the suspension is left uncovered and under constant stirring, olivenite [$Cu_2(AsO_4)(OH)$] will form.

Geminite was synthesized by reacting 0.92 g As_2O_5 powder with 0.35 g powder of malachite [$Cu_2CO_3(OH)_2$] in 10 mL of deionized water. First, the arsenic oxide powder was mixed with the deionized water and dissolved (see above). After the arsenical solution cooled down to room temperature, the malachite powder was added into the beaker. The mixture was stirred shortly and then left standing for 20 hours at room temperature. The final product was filtered and washed with deionized water and dried at room temperature (synthesis after Guillemin, 1956).

The malachite used for the geminite synthesis was synthesized after Tanaka and Yamane (1992). The starting solutions of 100 mL of 0.1 M $Cu(NO_3)_2$ and 100 mL of 0.15 M Na_2CO_3 were filled into borosilicate glass bottles and heated separately in a water bath to 35 °C with a thermostat. After temperature stabilization (~24 hours), both solutions were mixed into one flask and left in the water bath for another 24 hours. The final product was filtered and washed with deionized water and dried at room temperature.

The natural sample of geminite (private collection) is from Jáchymov, Czech Republic. The specimen originates from the Geschieber vein at the Daniel adit level in the Svornost mine. Geminite is associated with minor arsenolite [As_2O_3] and lavendulan [$NaCaCu_5(AsO_4)_4Cl{\cdot}5H_2O$] on the specimen, growing on milky-white quartz without any apparent hypogene sulfidic mineral. Additional specimens studied also originate from Jáchymov, from the Giftkies adit (Unruhe area) situated at the north-eastern part of the ore district. The Jáchymov ore district is located on the southern slope of the Erzgebirge, approximately 20 km north of Karlovy Vary and belongs to the NW–SE striking Gera-Jáchymov fault zone (Viehweg, 1995) and most of the ore minerals were deposited during the Variscan mineralization from mesothermal fluids (Ondruš et al., 1997). The ore district is limited by several major fault zones and the Giftkies adit is located in the north-eastern corner of this fault-bound area.

The natural liroconite sample grows on aggregates of older strashimirite and is from the type locality Wheal Gorland at St. Day, Cornwall, UK, from the collection of the National Museum in Prague (cat. no. P1N 26.818). The mine Wheal Gorland is part of the Camborne-Redruth mining district which is situated in Cornwall, the south-western part of Great Britain, approximately 90 km west of Plymouth. The Variscan granitic pluton in Cornwall is peraluminous, and the small granite bodies that host the mineralization, Carn Brea and Carn Marth, are more aluminous than the average Cornubian granite (Charoy, 1986). Several types of ore mineralisation were emplaced in these granitic rocks in Variscan and late Variscan times (Chesley et al., 1993). The last stage of significant mineralogical changes is the pervasive kaolinization, placed in the Cretaceous–Tertiary period (Sheppard, 1977). The kaolin deposits are thought to be trough- or funnel-shaped and may reach depths of 200 m. The copper mine Wheal Gorland is located on the east contact zone of the Carn Marth granite, working within both the intrusion and the altered country rock, known as 'killas'. The oxidation zone of this arseniferous copper mine reaches 180 m depth and was the subject of extensive mineral collecting in the late 18th and early 19th centuries.

2.4 Methods

Powder X-ray diffraction (pXRD) patterns of all samples were collected with a Bruker D8 ADVANCE DaVinci diffractometer (Institute of Geosciences, Friedrich-Schiller-University Jena, Germany) employing CuKα radiation (λ = 1.54058 Å). The patterns were collected at room temperature between 5 and 90 °2θ with a step size of 0.02 °2θ, and a time per step of 1.0 s. Lattice parameters were refined with the software TOPAS (Bruker, 2009; Coelho, 2018).

Single-crystal X-ray diffraction data were acquired with a Rigaku SuperNova single-crystal diffractometer (Institute of Physics, ASCR, v.v.i., Prague, Czech Republic) equipped with an Atlas S2 detector and using the mirror-monochromatised MoKα radiation (λ = 0.71073 Å) from a microfocus X-ray tube, providing a high-flux brilliant beam. Corrections for background, Lorentz effect and polarization were applied to the data during reduction in the CrysAlis package (Rigaku, 2019). The correction for absorption was carried out using Gaussian correction combined with empirical scaling in the JANA2006 software (Petříček et al., 2014). Single-crystal XRD data were collected for a tabular 0.080 mm × 0.065 mm × 0.045 mm large single crystal of liroconite from Cornwall (also used for calorimetric study). The structure has been solved independently of previous structure investigations (Burns et al., 1991) using a charge-flipping algorithm of the program SHELXT (Sheldrick, 2015) and subsequently treated by the least-squares refinement in JANA2006 (Petříček et al., 2014). Another single-crystal XRD data set was collected for a fragment of geminite crystal from Jáchymov, of a prismatic shape and approximate dimensions of 0.060 mm × 0.013 mm × 0.009 mm.

The chemical composition was determined by wavelength dispersive analyses using a Cameca SX100 electron microprobe (Laboratory of Electron Microscopy and Microanalysis of Masaryk University and the Czech Geological Survey in Brno, Czech Republic) with an acceleration

voltage of 15 kV, a sample current of 5 nA and a beam diameter of 10 μm. The following lines and standards were used: Kα: albite (Na), almandine (Fe), Co (Co), gahnite (Zn), lammerite (Cu), Mg_2SiO_4 (Mg), Ni_2SiO_4 (Ni), sanidine (Al, K, Si), $ScVO_4$ (V), spessartine (Mn), $SrSO_4$ (S), topaz (F), fluorapatite (P, Ca), vanadinite (Cl); Lα: lammerite (As); Lβ: Sb (Sb); Mα: vanadinite (Pb); Mβ: Bi (Bi). Peak counting times (CTs) were 20 s for main elements and 60 s for minor elements; the CT for each background was one-half of the peak time. The raw intensities were converted to the concentrations automatically using PAP (Pouchou and Pichoir, 1985) matrix-correction software.

The Cu and As concentration in the fine-grained pushcharovskite sample was analysed with a simultaneous radial inductively coupled optical emission spectrometer (ICP-OES) 725ES (Agilent, University of Jena, Germany) with a charge-coupled device (CCD) detector and an ASX 520 autosampler (Teledyne CETAC). The sample (~10 mg) was diluted in 10 mL of 20 % HNO_3.

Fourier-transform infrared (FT-IR) transmission spectra were recorded using a Nicolet iS10 spectrometer (University of Jena, Germany). The samples (1-2 mg) were mixed with KBr (FT-IR spectroscopy grade, Merck), gently ground and pressed to pellets. The pellets were measured at wavenumbers from 4000 to 400 cm^{-1} with 64 scans per spectrum at a resolution of 4 cm^{-1}. The spectra were baseline-corrected and normalized to maximum intensity.

The thermogravimetric analysis (TGA) was performed on a Setaram TG 92 (University of Jena, Germany), flushed with argon gas and a heating rate of 10 K/min. Samples ground to fine powder were filled in corundum ceramic cups (15-30 mg) and subjected to the TG analysis.

The acid-solution calorimeter (University of Jena, Germany) is a commercial IMC-4400 isothermal microcalorimeter (Calorimetry Sciences Corporation), modified for the purposes of acid-solution calorimetry (Majzlan, 2017a). The liquid water bath of the calorimeter is held at constant temperature of 298.15 K with fluctuations smaller than 0.0005 K. The solvent was 25 g of 5 N HCl and is contained in a polyetheretherketone (PEEK) cup with a total volume of 60 mL. The PEEK cup is then closed with a PEEK screw lid and inserted into the calorimeter well where it stabilizes for about 8 hours. During the stabilization and the experiment, the solvent is stirred by a SiO_2 glass stirrer by a motor positioned about 40 cm from the active zone of the instrument. The samples were pressed into a pellet and weighed on a microbalance with a precision of 0.002 mg. The pellets are then dropped through an SiO_2 glass tube into the solvent and the heat produced or consumed during the dissolution was measured. The heat flow between the reaction cup and the constant temperature reservoir was then integrated to calculate the caloric effect. A typical experiment lasts 40-60 minutes and the end of the experiments is judged from the return of the baseline to the pre-experiment position. The pellet mass of each measured phase was calculated according to the stoichiometry of the thermochemical cycle.

Heat capacity was measured with a commercially designed relaxation calorimeter (Physical Properties Measurement System by Quantum Design) at Salzburg University, Austria. With due

care, accuracy can be within 1% for 5 to 300 K, and 5% for 0.7 to 5 K (Kennedy et al., 2007). The powdered sample was wrapped in a thin Al foil and compressed to produce a 0.5 mm thick pellet, which was then placed onto the sample platform of the calorimeter for the measurement. Measurements were conducted in the temperature interval 2 to 300 K. The heat capacity between 260 and 280 K was measured by differential scanning calorimetry (DSC) using a PerkinElmer Diamond DSC. Details of the method are described in Benisek et al. (2012).

The programs Geochemist's Workbench® (Bethke, 2011; Bethke et al., 2019) and PHREEQC (Parkhurst and Appelo, 1999) with the Lawrence Livermore National Laboratory (LLNL) thermodynamic database were used for some of the thermodynamic calculations performed in this work. The database was extended with the data for geminite, pushcharovskite, liroconite (this work), olivenite (Majzlan et al., 2015), euchroite (Majzlan et al., 2017b), cornubite and clinoclase (Magalhães et al., 1988).

Table 2-1. Unit cell parameters for geminite and pushcharovskite from this work, compared to values from studies on natural material.

	a [Å]	b [Å]	c [Å]	α [°]	β [°]	γ [°]	V [Å^3]	SG
geminite								
synthetic, this work	6.421(1)	8.089(1)	15.725(1)	86.71(1)	84.48(1)	84.48(1)	808.3(1)	P–1
natural, this work	6.447(5)	8.073(6)	15.754(9)	86.84(6)	84.55(6)	84.38(6)	811(1)	P–1
Prencipe et al. (1996)	6.433(1)	8.093(2)	15.764(3)	86.65(3)	84.35(3)	84.47(3)	811.9(3)	P–1
Cooper and Hawthorne (1995)	9.841(2)	10.818(2)	15.733(3)	95.71(2)	90.94(2)	103.11(2)	1621.9(6)	C–1
pushcharovskite								
synthetic, this work	13.614(2)	15.775(2)	19.285(2)	107.57(1)	90.88(1)	98.21(1)	3900.3(8)	P–1
Sarp and Sanz-Gysler (1997)	6.435(2)	11.257(4)	18.662(9)	79.40(6)	86.48(7)	83.59(4)	1319.3(7)	P–1
Pushcharovsky et al. (2000)	13.616(1)	15.667(1)	19.187(1)	106.93(1)	91.53(1)	98.40(1)	3863.3(3)	P–1

2.5 Results

All of the studied samples consist of a single phase, except for the natural geminite which contains a minor arsenolite impurity. The full-profile fit of the pXRD data of geminite indicates 1.1 mass % of arsenolite in the mixture. The quality of the geminite crystal prevented us from the collection of a dataset with reasonable intensity statistics. Therefore, we report here only the unit cell parameters (Table 2-1). The lattice parameters of pushcharovskite (refined after Pushcharovsky et al., 2000) are shown in Table 2-1. The potassium atom, which is in the structure of the natural sample of Pushcharovsky et al. (2000), was deleted for the refinement to account for the lack of potassium in this sample of pushcharovskite.

The structure solution of liroconite revealed nearly all atomic positions except for hydrogen atoms; those were localized from the difference Fourier maps and refined keeping soft constraints of 0.98(4) Å on the O–H distances as well as H–O–H angles, 105(1)° within the H_2O molecules and with the U_{iso} of each H set to 1.2 times that of the donor O atom. The final refinement including 94 parameters, 8 restraints and 11 constraints smoothly converged to R = 0.0196 and wR = 0.0519 for 962 unique observed reflections, having $I > 3\sigma(I)$, with GOF = 1.40. Crystallographic details, data collection and refinement parameters are given in Table 2-2. Atom coordinates and displacement parameters are listed in Table 2-3. The bond-valence analysis (after Brown, 2002), based on refined interatomic distances (Table 2-4) is provided in Table 2-5 using the bond-valence parameters given by Gagné and Hawthorne (2015) and Brown (2002). The crystallographic information file (CIF) and the structure factor list were deposited in the Supplement.

Table 2-2. Crystal data, collection and refinement parameters for liroconite.

Structural formula	$Cu_2Al(OH)_4[(AsO_4)_{0.86}(PO_4)_{0.14}](H_2^{[4]}O)_4$
Unit cell parameters	a = 12.6428(11) Å
	b = 7.5684(7) Å
	c = 9.8796(12) Å
	β = 91.276(8)°
V	945.10(17) Å^3
Z	4
Space group	$I2/c$
$D_{calc.}$	2.999 g cm^{-3}
Temperature	297 K
Wavelength	Mo$K\alpha$, 0.71073 Å
Crystal dimensions	0.080 × 0.065 × 0.045 mm^3
Limiting θ angles	3.14–27.90°
Limiting Miller indices	$-13 \le h < 16$, $-9 \le k \le 7$, $-12 \le l \le 12$
No. of reflections	3547
No. of unique reflections	1067
No. of observed reflections (criterion)	962 [$I > 3\sigma(I)$]
Absorption coefficient, method	7.65 mm^{-1}, Gaussian
T_{min}/T_{max}	0.8874/0.9266
Completeness to θ_{max}, R_{int}	0.94, 0.0191
F_{000}	837
Refinement by Jana2006 on F^2	
Param. refined, constraints, restraints	94, 11, 8
R, wR (obs)	0.0196, 0.0519
R, wR (all)	0.0223, 0.0535
GOF (obs, all)	1.40, 1.43
Weighting scheme	$1/(\sigma^2(I) + 0.0004I^2)$
$\Delta\rho_{min}$, $\Delta\rho_{max}$ (e Å^{-3})	–0.33, 0.35

Table 2-3. Atom coordinates and equivalent and anisotropic displacement parameters for liroconite.

	x/a	*y/b*	*z/c*	U_{eq}/U_{iso}	U^{11}	U^{22}	U^{33}	U^{12}	U^{13}	U^{23}
Cu	0.13086(3)	0.22215(5)	0.26999(3)	0.01060(12)	0.0066(2)	0.0170(2)	0.00827(18)	−0.00233(13)	0.00054(13)	−0.00472(12)
Al	0	0	0	0.0061(3)	0.0046(6)	0.0091(6)	0.0045(5)	−0.0015(4)	−0.0008(4)	−0.0001(4)
As/P	0.25	0.04577(5)	0	0.00562(13)	0.0043(2)	0.0079(2)	0.0046(2)	0	−0.00046 (15)	0
O1	0.85618(14)	0.0797(2)	0.00645(18)	0.0111(6)	0.0061(10)	0.0120(10)	0.0153(9)	0.0004(7)	−0.0003(8)	−0.0017(7)
O2	0.24534(15)	0.1739(3)	0.13824(18)	0.0111(6)	0.0083(10)	0.0163(11)	0.0089(9)	−0.0028(8)	0.0007(7)	−0.0066(7)
O3	0.02435(16)	0.0962(3)	0.17289(18)	0.0143(6)	0.0113(11)	0.0237(11)	0.0080(9)	−0.0091(8)	0.0015(8)	−0.0046(8)
O4	0.04158(15)	0.2232(2)	0.92236(18)	0.0112(6)	0.0085(10)	0.0129(11)	0.0121(9)	0.0021(7)	0.0015(8)	0.0036(7)
O5	0.6847(2)	0.1178(3)	0.3410(3)	0.0399(9)	0.0377(17)	0.0391(17)	0.0430(15)	0.0060(13)	−0.0003(13)	−0.0221(13)
O6	0.11033(19)	0.4928(3)	0.1219(2)	0.0259(8)	0.0261(14)	0.0282(13)	0.0236(12)	0.0084(10)	0.0081(10)	−0.0012(10)
H1O3	−0.0283(19)	0.053(4)	0.233(3)*							
H1O5	0.668(3)	0.216(3)	0.399(2)*							
H2O5	0.668(3)	0.158(4)	0.2518(17)*							
H1O4	−0.0178(17)	0.300(3)	0.905(3)*							
H1O6	0.1819(14)	0.533(4)	0.114(3)*							
H2O6	0.095(2)	0.432(4)	0.040(2)*							

* – atoms refined with isotropic displacement parameter se to 1.2*U_{eq} of the parent O atoms. Occupancy of the As/P site refined to 0.856(3)/0.144(3).

Table 2-5. Bond-valence analysis of the liroconite crystal structure.

	Cu	Al	As/P*	H1O3	H1O4	H1O5	H2O5	H1O6	H2O6	∑BV
O1		0.48×2↓	1.34×2↓			0.12	0.02			1.96
O2	0.41;0.47		1.23×2↓							2.11
O3	0.56	0.54×2↓		0.91						2.01
O4	0.48	0.47×2↓			0.91				0.07	1.93
O5	0.05					0.91	0.93	0.11		2.00
O6	0.09			0.11	0.09			0.91	0.93	2.13
∑BV	2.06	2.98	5.14	1.02	1.00	1.03	0.95	1.02	1.00	

All values are given in valence units (*vu*). * refined As/P occupancies taken into consideration.

Table 2-4. Selected interatomic distances (Å) and polyhedral-distortion measures in the structure of liroconite.

Cu–O2	2.001(2)	Al–O1^{vi}	1.9179(13)
Cu–O2^{i}	1.957(2)	Al–O1^{vii}	1.9179(13)
Cu–O3	1.894(2)	Al–O3	1.876(2)
Cu–O4^{ii}	1.946(2)	Al–O3^{viii}	1.876(2)
Cu–O5^{iii}	2.748(2)	Al–O4^{ix}	1.9329(17)
Cu–O6	2.527(2)	Al–O4^{x}	1.9329(17)
<Cu–O>	2.18	<Al–O>	1.91
Octahedral distortion	0.141	Octahedral distortion	0.012
Effective coordination number	3.98	Effective coordination number	5.97
As–O1^{vii}	1.645(1)		
As–O1^{iii}	1.645(1)		
As–O2	1.677(2)		
As–O2^{xi}	1.677(2)		
<As–O>	1.66		

Symmetry codes: (i) –x+1/2, –y+1/2, –z+1/2; (ii) x, –y+1/2, z–1/2; (iii) x–1/2, –y, z; (iv) –x, y+1/2, –z+1/2; (v) x, –y+1/2, z+1/2; (vi) x–1, y, z; (vii) –x+1, –y, –z; (viii) –x, –y, –z; (ix) x, y, z–1; (x) –x, –y, –z+1; (xi) –x+1/2, y, –z.

The results of the electron microprobe analyses of liroconite are shown in Table 2-6. The concentrations of Mn, Ca, Pb, Co, Ni, Zn, Fe, Mg, Na, K, Sb, V, S, Si and Cl were below the detection limits. Totals much below 100 % (Table 2-6) are caused by the presence of H_2O in the structure of liroconite but they do not correspond to the expected H_2O content of ~25 wt.%. Desiccation patterns, seen as numerous cracks in the liroconite crystals, confirm that the sample lost much H_2O (at least 4 H_2O per formula unit) under the vacuum inside the instrument. The weight percent of each oxide is CuO 44.18 ± 0.41, Al_2O_3 15.01 ± 0.16, As_2O_5 27.35 ± 0.61 and P_2O_5 3.54 ± 0.15. Based on (As + P) = 1 apfu, the average empirical formula for the studied liroconite is $Cu_{1.93}Al_{1.02}[(AsO_4)_{0.83}(PO_4)_{0.17}](OH)_4 \cdot 4H_2O$. As deficiencies on the Cu and Al positions in the structure are unlikely, we consider the values of 1.93 and 1.02, respectively, for these two positions with an analytical uncertainty. The slight difference in the formula between the crystallographic refinement, $Cu_2Al(OH)_4[(AsO_4)_{0.86}(PO_4)_{0.14}](H_2O)_4$, and the electron microprobe analysis is within analytical uncertainty. For the calorimetry work, we adopt the formula of $Cu_2Al[(AsO_4)_{0.83}(PO_4)_{0.17}](OH)_4 \cdot 4H_2O$ with the corresponding molecular mass of 425.6088 $g \cdot mol^{-1}$.

Table 2-6. Electron microprobe analysis of liroconite.

weight %					atoms per formula unit			
CuO	**Al_2O_3**	**As_2O_5**	**P_2O_5**	**Total**	**Cu**	**Al**	**As**	**P**
44.29	14.85	27.28	3.38	89.81	1.953	1.022	0.833	0.167
43.49	15.20	28.23	3.44	90.36	1.859	1.014	0.835	0.165
44.45	15.13	27.35	3.59	90.51	1.936	1.028	0.825	0.175
44.49	14.85	26.52	3.76	89.61	1.972	1.027	0.813	0.187

The As and Cu contents of pushcharovskite are 28.96 ± 0.15 wt.% As and 31.70 ± 0.39 wt.% Cu. This leads to $Cu_{0.96}(As_{1.04}O_3OH)(H_2O)\cdot 0.5H_2O$. The deviations of the stoichiometric coefficients of Cu and As from 1 are within analytical uncertainties. For calorimetry, we adopt the ideal formula $Cu(AsO_3OH)(H_2O)\cdot 0.5H_2O$ with the corresponding molecular mass 230.4945 $g\cdot mol^{-1}$.

The infrared spectra of pushcharovskite and the wavenumbers of the bands are displayed in Fig. 2-1. This spectrum is comparable to the one shown in Chukanov (2014). Some of the weak bands described by Chukanov (2014) are not seen in our spectra but the strong bands are comparable. Bands observed in the range of 400 to 560 cm^{-1} are assigned to bending vibrations of the AsO_4 groups, and those in the range of 750 to 950 cm^{-1} are assigned to AsO_4 stretching vibrations (Frost et al., 2002; Martens et al., 2003). The bands around 1632 cm^{-1} and 3426 cm^{-1} are attributed to the O–H stretching and bending modes of water. Furthermore, the bands around 3315 cm^{-1} and 3572 cm^{-1} correspond to the hydroxyl ions (Frost et al., 2002; Martens et al., 2003). Pushcharovskite was also investigated by thermogravimetric analysis (Fig. 2-2). Molecular H_2O is released at temperatures less than 127 °C and the sample seems to be completely dehydrated at 530 °C. One of the experiments was stopped at 900 °C (point 1 in Fig. 2-2) and the powder XRD showed that the sample contained a mixture of $Cu_2As_2O_7$ and $Cu_3(AsO_4)_2$. After heating to 1600 °C (point 2 in Fig. 2-2), the sample consisted of metallic copper, some arsenic and minor

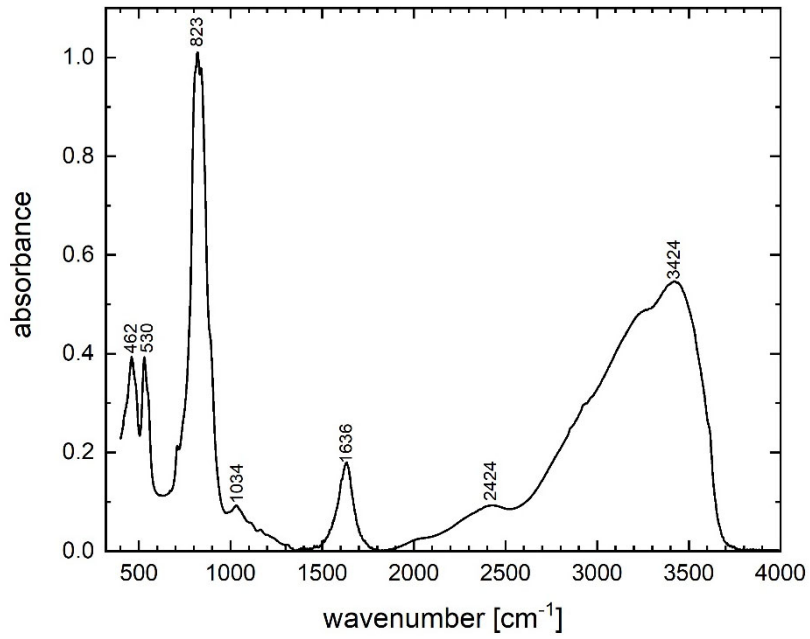

Figure 2-1. FT-IR spectrum of pushcharovskite. Bands are marked with their positions in cm^{-1}.

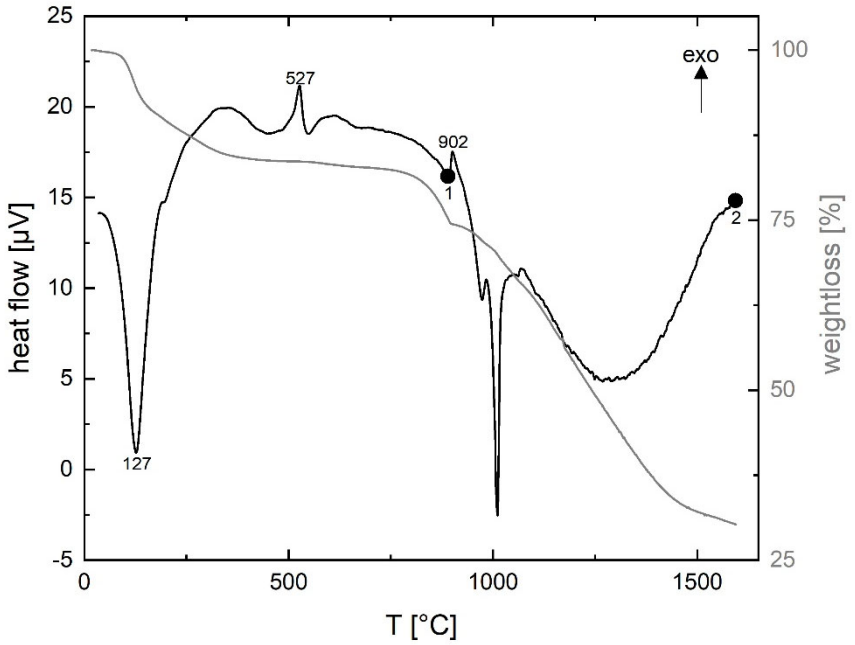

Figure 2-2. Thermogravimetric analysis of pushcharovskite. The extrema in the heat flow are labelled with the corresponding temperature (°C). Two separate runs were stopped at temperatures, marked by circles on the heat flow curve, and the products were investigated by pXRD. Details are in the text.

arsenic copper (As_2Cu) and cuprite (Cu_2O). The measured mass loss is 17.34 ± 1.41 wt.%. If all expected water (total $2H_2O$) is released, the mass loss should be around 15.6% (after stoichiometric calculations). This difference between the measured and the calculated mass loss could be due to water adsorption of H_2O onto the fine-grained sample.

2.5.1 Crystal structure and hydrogen-bonding network in liroconite

The crystal structure of liroconite revealed by the current work corresponds to the structural model proposed by Kolesova and Fesenko (1968) and Burns et al. (1991); nevertheless, it contains one substantial difference (see below). Moreover, here, we additionally present the positions of the H atoms, which were not localized by the previous structural studies.

Unlike previous studies (*I*2/*a*), we present our model in the space group *I*2/*c* (non-standard setting of the *C*2/*m*). Our choice was driven by the minute difference in reflection statistics that were present. While our space group choice was violated by five reflections (having $I/\sigma(I)$~4), the space group *I*2/a was contradicted by nine reflections (including 4 *h*0*l* reflections with *h* = odd) of the approximately same $I/\sigma(I)$. The refinement led to satisfactory results (Table 2-2); therefore, we decided to retain this space group choice.

The structure of liroconite is a heteropolyhedral framework that consists of infinite octahedral-tetrahedral $[Al_2(AsO_4)_2(OH)_4]$ chains running parallel to [100] decorated by edge-sharing $[Cu_2O_2(OH)_4(H_2O)_4]$ dimers that are cross-linking these chains. The Al^{3+} cations are in a regular octahedral coordination. The Cu^{2+} cations are six-fold coordinated in strongly distorted manner (Table 2-4).

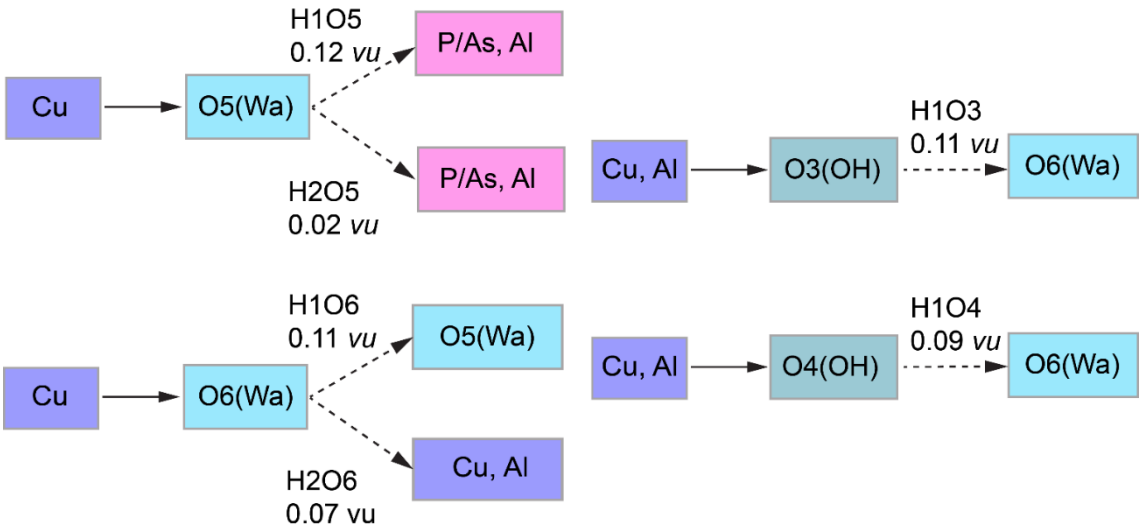

Figure 2-3. Hydrogen bonding in the structure of liroconite: Cu/Al – octahedrally coordinated cations; Wa – H_2O molecule; OH – hydroxyl group; ---> H bond; bond strengths are given in valence units (vu).

Types and the distinct roles of the H_2O in structures of hydrated oxysalts were described and reviewed in detail and can be found elsewhere (Hawthorne, 1992, 2012; Hawthorne and Schindler, 2008; Hawthorne and Sokolova, 2012; Schindler and Hawthorne, 2008). Generally, there are several types of H_2O moieties in crystal structures, and each of them plays a slightly distinct role in structure bonding. Particular types of H_2O can be distinguished based on the coordination number of O atoms in these H_2O groups. In the structures of oxysalts, there are *transformer*, *non-transformer* and *inverse-transformer* H_2O groups with [3], [4], and [5]-fold coordinated O atoms, respectively. Their role is generally to transfer the bond valence from cations (Lewis acids) to anions (Lewis bases), keeping the structure together, as the strengths of these components are equal or similarly matching, following the valence-matching principle of the bond-valence theory (Hawthorne, 2012; Brown, 2002, 2009).

The structure of liroconite contains two symmetrically independent H_2O molecules and two symmetrically independent OH groups. Those two H_2O molecules (with O5 and O6 atoms) are linked to the Cu site, forming elongated vertices of the $Cu(H_2O)_2O_2(OH)_2$ octahedron, which is strongly distorted (Table 2-4) due to the Jahn–Teller effect on Cu^{2+}, which leads to the

Table 2-7. Hydrogen-bond geometry (in Å and °) in the structure of liroconite.

D–H···A	D–H	H···A	D···A	D–H···A (°)
O3–H1O3···O6^{xxi}	0.96(3)	1.85(3)	2.788(3)	167(3)
O5–H1O5···O1^{xix}	0.96(2)	1.84(2)	2.795(3)	173(2)
O5–H2O5···O1^{xiv}	0.95(2)	2.63(2)	3.472(4)	148(2)
O4–HO4···O6^{xxiii}	0.96(2)	1.97(2)	2.909(3)	164(2)
O6–H1O6···O5^{xxx}	0.96(2)	1.85(2)	2.776(4)	161(3)
O6–H2O6···O4^{ix}	0.95(2)	2.07(3)	2.954(3)	156(2)

(*4+2*) configuration (Burns and Hawthorne, 1995a). Both H_2O molecules extend linkage between Cu dimers and infinite *M–T* chains. The typology of the H_2O groups in the structure of liroconite is particularly interesting, since the H_2O groups linked to the Cu site are in fact not transformer groups with [3]-coordinated O central atoms, but *inverse-transformer* H_2O groups, since each H_2O accepts one additional H-bond (and thus it is [4]-coordinated) from the OH groups (Fig. 2-3). The geometry of hydrogen bonds in the crystal structure of liroconite is summarized in Table 7. The structural formula of liroconite is $Cu_2Al(OH)_4[(AsO_4)_{0.86}(PO_4)_{0.14}](H_2^{[4]}O)_4$, with Z = 4 and $D_{calc.}$ = 2.9992 g cm^{-3}.

2.5.2 Enthalpies of formation

The enthalpies of formation were determined by acid solution calorimetry. Heat consumed or released by the system was measured by dissolving pellets of each sample in 5 N HCl. Reference compounds are needed to construct the thermodynamic cycle from which the enthalpies of formation will be determined. The enthalpies of formation of the reference compounds must be known accurately, so we used KCl, $HCl{\cdot}9.96H_2O$, KH_2AsO_4 and CuO as the references; $HCl{\cdot}9.96H_2O$ is the composition of the calorimetric solvent, 5 N HCl. The choice of these reference compounds was explained, discussed and justified by Majzlan (2017a). No problems were encountered with the dissolution of the studied or reference phases. Application of the appropriate thermochemical cycles (Table 2-9) gave the enthalpies of formation summarized in Table 2-8.

Table 2-8. Thermodynamic properties of the studied phases.

	Δ_fH°	S^o	Δ_fS° [b]	Δ_fG°	log K_{sp}
Pushcharovskite	–1250.5±3.0	176.4±2.1	–718.0±2.3	–1036.4±3.8	–17.21[c]
Geminite (natural)	–1110.4±3.0[a]	158.2	–619.5	–925.7±3.2	–18.58[d]
Geminite (synth.)	–1111.4±3.0	158.2	–619.5	–926.7±3.2	–18.75[d]
Liroconite (natural)	–3516.6±9.1	401.1±4.8	–1745.1±4.9	–2996.3±9.2	–4.92[e]
Liroconite (estimate for the phosphate-free end-member)				–2931.6	–4.85[f]

The formation reactions are defined in table 10, reactions ΔH_{18}, ΔH_{19}, ΔH_{20}. All enthalpy and Gibbs free energy values are in kJ·mol^{-1}, all entropy values are in J·mol^{-1}·K^{-1}.
[a] corrected for the arsenolite impurity
[b] calculated from the entropies of elements in their standard state (from Robie and Hemingway, 1995)
[c-f] Solubility products were calculated with these auxiliary data (all in kJ·mol^{-1}): $\Delta_fG^o(Cu^{2+},aq)$ = +65.1±0.1 (Robie and Hemingway, 1995), $\Delta_fG^o(AsO_4^{3-},aq)$ = –647.6±1.5 (Nordstrom et al., 2014), $\Delta_fG^o(PO_4^{3-},aq)$ = –1025.5±1.6 (Grenthe et al., 1992), $\Delta_fG^o(H_2O,l)$ = –237.14±0.04 (Robie and Hemingway, 1995), $\Delta_fG^o(Al^{3+},aq)$ = –489.4±1.4 (Robie and Hemingway, 1995).

These equilibrium constants refer to the reactions:
[c] $Cu(H_2O)(AsO_3OH){\cdot}0.5H_2O = Cu^{2+} + AsO_4^{3-} + H^+ + 1.5H_2O$
[d] $Cu(H_2O)(AsO_3OH) = Cu^{2+} + AsO_4^{3-} + H^+ + H_2O$
[e] $Cu_2Al[(AsO_4)_{0.83}(PO_4)_{0.17}](OH)_4{\cdot}4H_2O + 4H^+ = 2Cu^{2+} + Al^{3+} + 0.83AsO_4^{3-} + 0.17PO_4^{3-} + 8H_2O$
[f] $Cu_2Al(AsO_4)(OH)_4{\cdot}4H_2O + 4H^+ = 2Cu^{2+} + Al^{3+} + AsO_4^{3-} + 8H_2O$

Table 2-9. Thermochemical cycle for the studied minerals.

Reaction and reaction number	
KH_2AsO_4 (cr) = K^+ (aq) + 2 H^+ (aq) + AsO_4^{3-} (aq)	1
KH_2PO_4 (cr) = K^+ (aq) + 2 H^+ (aq) + PO_4^{3-} (aq)	1b
CuO (cr) + 2 H^+ (aq) = Cu^{2+} (aq) + H_2O (aq)	2
$HCl·9.96H_2O$ (l) = H^+ (aq) + Cl^- (aq) + $9.96H_2O$ (aq)	3
H_2O (l) = H_2O (aq)	4
KCl (cr) = K^+ (aq) + Cl^- (aq)	5
$CuSO_4·5H_2O$ (cr) = Cu^{2+} (aq) + SO_4^{2-} (aq) + $5H_2O$ (aq)	6
$Al_2(SO_4)_3$ (cr) = $2Al^{3+}$ (aq) + $3SO_4^{2-}$ (aq)	7
$Cu(AsO_3OH)·1.5H_2O$ (cr) = Cu^{2+} (aq) + AsO_4^{3-} (aq) + H^+ (aq) + $1.5H_2O$ (aq)	8
$Cu(AsO_3OH)·H_2O$ (cr) = Cu^{2+} (aq) + AsO_4^{3-} (aq) + H^+ (aq) + H_2O (aq)	9
$Cu_2Al[(AsO_4)_{0.83}(PO_4)_{0.17}](OH)_4·4H_2O$ (cr) = $2Cu^{2+}$ (aq) + Al^{3+} (aq) + $0.83AsO_4^{3-}$ (aq) + $0.17PO_4^{3-}$ (aq) + $4OH^-$ (aq) + $4H_2O$ (aq)	10
K (cr) + As (cr) + H_2 (g) + $2O_2$ (g) = KH_2AsO_4 (cr)	11
K (cr) + P (cr) + H_2 (g) + $2O_2$ (g) = KH_2PO_4 (cr)	11b
Cu (cr) + $(1/2)O_2$ (g) = CuO (cr)	12
10.46 H_2 (g) + 9.96 $(1/2)O_2$ (g) + $(1/2)Cl_2$ (g) = $HCl·9.96H_2O$ (l)	13
H_2 (g) + $(1/2)O_2$ (g) = H_2O (l)	14
K (cr) + $(1/2)Cl_2$ (g) = KCl (cr)	15
Cu (cr) + S (cr) + $(9/2)O_2$ (g) + $5H_2$ (g) = $CuSO_4·5H_2O$ (cr)	16
2Al (cr) + 3S (cr) + $6O_2$ (g) = $Al_2(SO_4)_3$ (cr)	17
Cu (cr) + As (cr) + $2H_2$ (g) + $2.75O_2$ (g) = $Cu(AsO_3OH)·1.5H_2O$ (cr)	18
Cu (cr) + As (cr) + $1.5H_2$ (g) + $2.5O_2$ (g) = $Cu(AsO_3OH)·H_2O$ (cr)	19
2Cu (cr) + Al (cr) + 0.83As (cr) + 0.17P (cr)+ $6H_2$ (g) + $6O_2$ (g) = $Cu_2Al[(AsO_4)_{0.83}(PO_4)_{0.17}](OH)_4·4H_2O$ (cr)	20
ΔH_1 = 24.748 ± 0.181	Majzlan (2017a)
ΔH_{1b} = 25.105 ± 0.332	Majzlan (2017a)
ΔH_2 = -51.526 ± 0.160	Majzlan (2017a)
ΔH_3 = 0	dissolution of $HCl·9.96H_2O$ in $HCl·9.96H_2O$
ΔH_4 = -0.54	calculated from Parker (1965)
ΔH_5 = 17.693 ± 0.058	Majzlan (2017a)
ΔH_6 = 49.713 ± 0.186	Majzlan et al. (2015)
ΔH_7 = -232.34 ± 2.01	Majzlan (2017a)
ΔH_8 = 6.13 ± 0.15	this work
ΔH_{9a} = 10.19 ± 0.21	this work
ΔH_{9b} = 9.14 ± 0.32	this work
ΔH_{10} = -98.81 ± 1.45	this work
ΔH_{11} = -1181.2 ± 2.0	Majzlan (2011)
ΔH_{11b} = -1573.6 ± 1.0	Majzlan (2011)
ΔH_{12} = -156.1 ± 2.0	Robie and Hemingway (1995)
ΔH_{13} = -3007.9 ± 1.0	calculated fromWagman et al. (1991)
ΔH_{14} = -285.8 ± 0.1	Robie and Hemingway (1995)
ΔH_{15} = -436.5 ± 0.2	Robie and Hemingway (1995)
ΔH_{16} = -2279.5 ± 3.4	Grevel and Majzlan (2011)
ΔH_{17} = -3441.8 ± 1.8	Robie and Hemingway (1995)
$\Delta H_{18} = \Delta_f H°$(pushcharovskite) = $\Delta H_1 + \Delta H_2 + \Delta H_3 - 9.46\Delta H_4 - \Delta H_5 - \Delta H_8 + \Delta H_{11} + \Delta H_{12} + \Delta H_{13} - 9.46\Delta H_{14} - \Delta H_{15}$	
$\Delta H_{19a} = \Delta_f H°$(geminite, syn) = $\Delta H_1 + \Delta H_2 + \Delta H_3 - 9.96\Delta H_4 - \Delta H_5 - \Delta H_{9a} + \Delta H_{11} + \Delta H_{12} + \Delta H_{13} - 9.96\Delta H_{14} - \Delta H_{15}$	
$\Delta H_{19a} = \Delta_f H°$(geminite, nat) = $\Delta H_1 + \Delta H_2 + \Delta H_3 - 9.96\Delta H_4 - \Delta H_5 - \Delta H_{9b} + \Delta H_{11} + \Delta H_{12} + \Delta H_{13} - 9.96\Delta H_{14} - \Delta H_{15}$	
$\Delta H_{20} = \Delta_f H°$(liroconite) = $0.83\Delta H_1 + 0.17\Delta H_{1b} + 3.5\Delta H_2 + \Delta H_3 + 2.04\Delta H_4 - \Delta H_5 - 1.5\Delta H_6 + 0.5\Delta H_7 - \Delta H_{10} + 0.83\Delta H_{11} + 0.17\Delta H_{11b} + 3.5\Delta H_{12} + \Delta H_{13} + 2.04\Delta H_{14} - \Delta H_{15} - 1.5\Delta H_{16} + 0.5\Delta H_{17}$	

2.5.3 Low-temperature heat capacity and entropies

Heat capacity of pushcharovskite and liroconite was measured by relaxation calorimetry from 2 K to 300 K (Fig. 2-4a, b). Data below 12 K, including an extrapolation to 0 K, were fitted with extended Debye polynomials. Data above 12 K were fitted with series of orthogonal polynomials. These fits were used to calculate the value of enthalpy and entropy increments at regular intervals by integrating C_p/T (Tables 2-10,2-11).

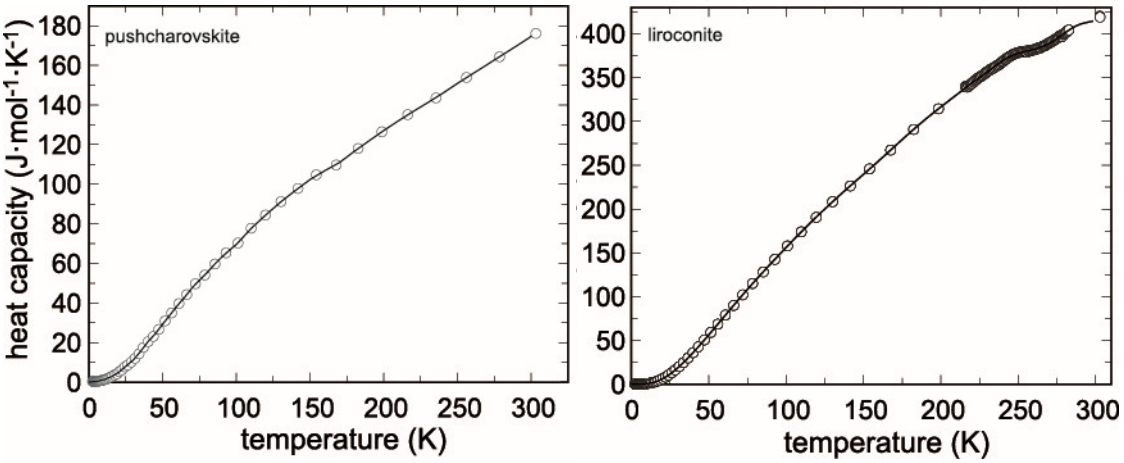

Figure 2-4. Low-temperature heat capacity of pushcharovskite and liroconite. Circles show the measured data, and the curves are the polynomials used for fitting.

There are no anomalies in the C_p data for pushcharovskite. For liroconite, there is a flat anomaly at around T = 250 K (Fig. 4b). This anomaly was confirmed by a detailed measurement with closely spaced temperature intervals. The nature and cause for this anomaly, however, are not clear.

The entropy of geminite was calculated (Table 2-9) based on the simple Kopp rule stating that the entropy of a phase is simply the sum of entropies of its components. The components and their entropy are CuO (S^o = 42.6 $J \cdot mol^{-1} \cdot K^{-1}$) (all Robie and Hemingway, 1995), As_2O_5 (105.44) (Nordstrom and Archer, 2003), and H_2O (ice, 41.94) (Majzlan et al., 2003). The entropy of pushcharovskite, calculated by the same algorithm, would be 179.2 $J \cdot mol^{-1} \cdot K^{-1}$, fairly close to the experimental datum of 176.4±2.1 $J \cdot mol^{-1} \cdot K^{-1}$.

Table 2-10. Molar thermodynamic functions for pushcharovskite, $Cu(AsO_3OH)(H_2O)\cdot 0.5H_2O$, molecular mass 230.4945 g·mol^{-1}.

T K	C_p J·mol^{-1}·K^{-}	H_T-H_0 J·mol^{-1}	S J·mol^{-1} K^{-}	G_T-G_0 J·mol^{-1}	T K	C_p J·mol^{-1}·K^{-}	H_T-H_0 J·mol^{-1}	S J·mol^{-1}·K^{-}	G_T-G_0 J·mol^{-1}
10	1.106	4.574	0.8421	-3.847	170	110.9	9562	97.67	-7041
20	4.96	32.15	2.603	-19.92	180	116.6	10700	104.2	-8050
30	11.27	112.1	5.757	-60.63	190	121.9	11892	110.6	-9124
40	20.48	269.3	10.21	-139.1	200	127.1	13138	117.0	-10263
50	29.41	516.0	15.68	-267.8	210	132.1	14433	123.3	-11464
60	38.82	857.4	21.87	-455.0	220	136.8	15778	129.6	-12729
70	47.74	1290	28.52	-706.6	230	141.3	17169	135.8	-14056
80	55.33	1806	35.40	-1026	240	145.9	18604	141.9	-15444
90	63.14	2399	42.38	-1415	250	150.9	20088	147.9	-16893
100	69.63	3064	49.38	-1874	260	155.7	21621	153.9	-18403
110	77.72	3800	56.39	-2402	270	160.3	23201	159.9	-19972
120	84.58	4612	63.45	-3002	273.15	161.8	23708	161.8	-20478
130	91.03	5490	70.47	-3671	280	165.0	24827	165.8	-21600
140	96.86	6430	77.43	-4411	290	169.8	26501	171.7	-23288
150	102.5	7426	84.31	-5220	298.15	173.7	27901	176.4	-24707
160	106.9	8475	91.08	-6097	300	174.6	28224	177.5	-25034

Table 2-11. Molar thermodynamic functions for liroconite, $Cu_2Al[(AsO_4)_{0.83}(PO_4)_{0.17}](OH)_4\cdot 4H_2O$, molecular mass 425.6088 g·mol^{-1}.

T K	C_p J·mol^{-1}·K^{-1}	H_T-H_0 J·mol^{-1}	S J·mol^{-1} K^{-1}	G_T-G_0 J·mol^{-1}	T K	C_p J·mol^{-1}·K^{-}	H_T-H_0 J·mol^{-1}	S J·mol^{-1}·K^{-}	G_T-G_0 J·mol^{-1}
10	0.6495	1.979	0.3667	-1.688	170	271.0	21290	206.3	-13770
20	6.008	29.11	2.043	-11.75	180	286.9	24080	222.2	-15920
30	18.60	146.8	6.645	-52.51	190	302.1	27030	238.1	-18220
40	36.11	417.4	14.31	-154.9	200	316.3	30120	254.0	-20680
50	56.11	877.2	24.49	-347.1	210	329.9	33350	269.8	-23300
60	77.04	1543	36.56	-650.9	220	343.5	36720	285.4	-26070
70	97.85	2418	50.00	-1083	230	356.1	40210	301.0	-29010
80	117.9	3497	64.39	-1654	240	369.0	43840	316.4	-32090
90	137.2	4774	79.40	-2373	250	377.6	47580	331.6	-35330
100	155.8	6239	94.83	-3244	260	382.1	51380	346.6	-38720
110	174.0	7889	110.5	-4270	270	388.8	55230	361.1	-42260
120	191.4	9717	126.4	-5455	273.15	392.1	56460	365.6	-43410
130	208.0	11710	142.4	-6799	280	400.5	59170	375.4	-45940
140	223.9	13870	158.4	-8303	290	410.7	63230	389.7	-49770
150	239.3	16190	174.4	-9967	298.15	414.4	66600	401.1	-52990
160	254.9	18660	190.3	-11790	300	415.6	67370	403.7	-53740

2.5.4 Gibbs free energies of formation and solubility products

Combining the entropies and enthalpies of formation, using the relationship of the thermodynamic functions $\Delta_f G° = \Delta_f H° - T\Delta_f S°$, results in the Gibbs free energies of formation for pushcharovskite, geminite and liroconite (Table 2-9). This table includes solubility products from these values.

The solubility products, just like the enthalpies of formation, are influenced by the choice of the auxiliary data. The calculation of solubility products requires the Gibbs free energies of formation of aqueous ions in their standard state. Herein lies the problem with the decision as to which values should be used. This issue becomes alarming in some cases, for example, for liroconite in this study. Using the values from Robie and Hemingway (1995) and the value for AsO_4^{3-} from Nordstrom et al. (2014), the solubility product for liroconite (natural sample with phosphate in its structure) is –5.57. Using the critical selection from Grenthe et al. (1992), the same variable changes to –4.92. The reason for the difference is the massive change in the Gibbs free energy of formation of the phosphate (PO_4^{3-}) ion. Here, to preserve consistency with our previous studies on copper phosphates and arsenates (Majzlan et al., 2015; Majzlan et al., 2017b), we adopt the same values as before (listed in footnote for Table 2-9). The users of thermodynamic databases who are performing geochemical calculations should be aware of such differences and their implications for their results.

2.5.5 Thermodynamics of the endmember liroconite

For geochemical modelling, it is desirable to possess the thermodynamic properties of the endmember liroconite, $Cu_2Al(AsO_4)(OH)_4 \cdot 4H_2O$. The estimate is based on the same reasoning as in the case of euchroite (Majzlan et al., 2017b). The copper phosphates appear to be less soluble than the copper arsenates and the difference in the solubility product for the olivenite–libethenite pair is 0.44 log units. Assuming the same difference between liroconite and its phosphate analogue, the solubility product for the endmember liroconite would be $-4.92 + (0.17 \cdot 0.44) = -4.85$.

2.6 Discussion

2.6.1 Liroconite: associated minerals and thermodynamic models

The oxidation zone at the Wheal Gorland mine in Cornwall is known for the occurrence of a number of copper arsenates (clinoclase, chalcophyllite, chenevixite, ceruleite, cornwallite, liroconite, olivenite), copper carbonates (azurite, malachite) and ferric arsenates (pharmacosiderite, scorodite). There are rich accumulations of cuprite and native copper and the gangue is mainly quartz and fluorite.

The most common supergene minerals directly associated with liroconite are other copper arsenates, especially olivenite, strashimirite and clinoclase. The temporal relationship of liroconite and all its associated phases is complex, with examples seen of liroconite both before and after the other copper arsenates (Fig. 2-5), including pseudomorphs of copper arsenates after liroconite (Fig. 2-5d). For instance, liroconite grows on clinoclase or *vice versa* (Fig. 2-5e). Overall trends can be observed, but one must allow for the appreciation that local conditions of formation moved in, out, and returned to areas of pH-pε that were suitable for liroconite growth, as seen on a few rare examples where a second generation of liroconite can be observed, ultimately indicating simplistic crystallization pathways possible in two directions. Many specimens showing a quartz-remnant sulfide vein assemblage where liroconite is present are characterized by an initial, presumed amorphous gel-like phase which has not been extensively studied, which may be followed by pharmacosiderite, which is never seen post liroconite. The main liroconite crystallization phase can additionally be preceded by malachite, parnauite, olivenite, strashimirite or clinoclase. Parnauite tends to be much more common pre-liroconite than the other phases, yet some examples post-liroconite are observed. Strashimirite and clinoclase are very intimately associated with liroconite and must have very similar conditions of formation, possibly co-genetic, although it is noteworthy that they tend to be slightly more prevalent in well-crystallized examples post-liroconite. Olivenite, the most frequently associated mineral, is also more common post liroconite, but has a clear role to play and is quite rich in some specimens pre-liroconite. Direct association of liroconite with cornwallite, and the other darker-green microcrystalline arsenates cornubite and cornwallite, is less common, but always post-liroconite. Malachite is slightly more dominant post-liroconite. Despite the fact that both liroconite and chalcophyllite were rather common minerals at Wheal Gorland, dominating the interest in the copper arsenates from here in the 18th and 19th centuries, surprisingly there are only a few specimens where liroconite is directly associated with chalcophyllite. In this case liroconite is younger and grows on chalcophyllite (Fig. 2-5f). There are also examples of liroconite growing on older crusts of ceruleite or being overgrown by ceruleite (Fig. 2-5b). Azurite is observed in association with liroconite at Gorland where it is generally post-liroconite (Fig. 2-5c), but at Ting

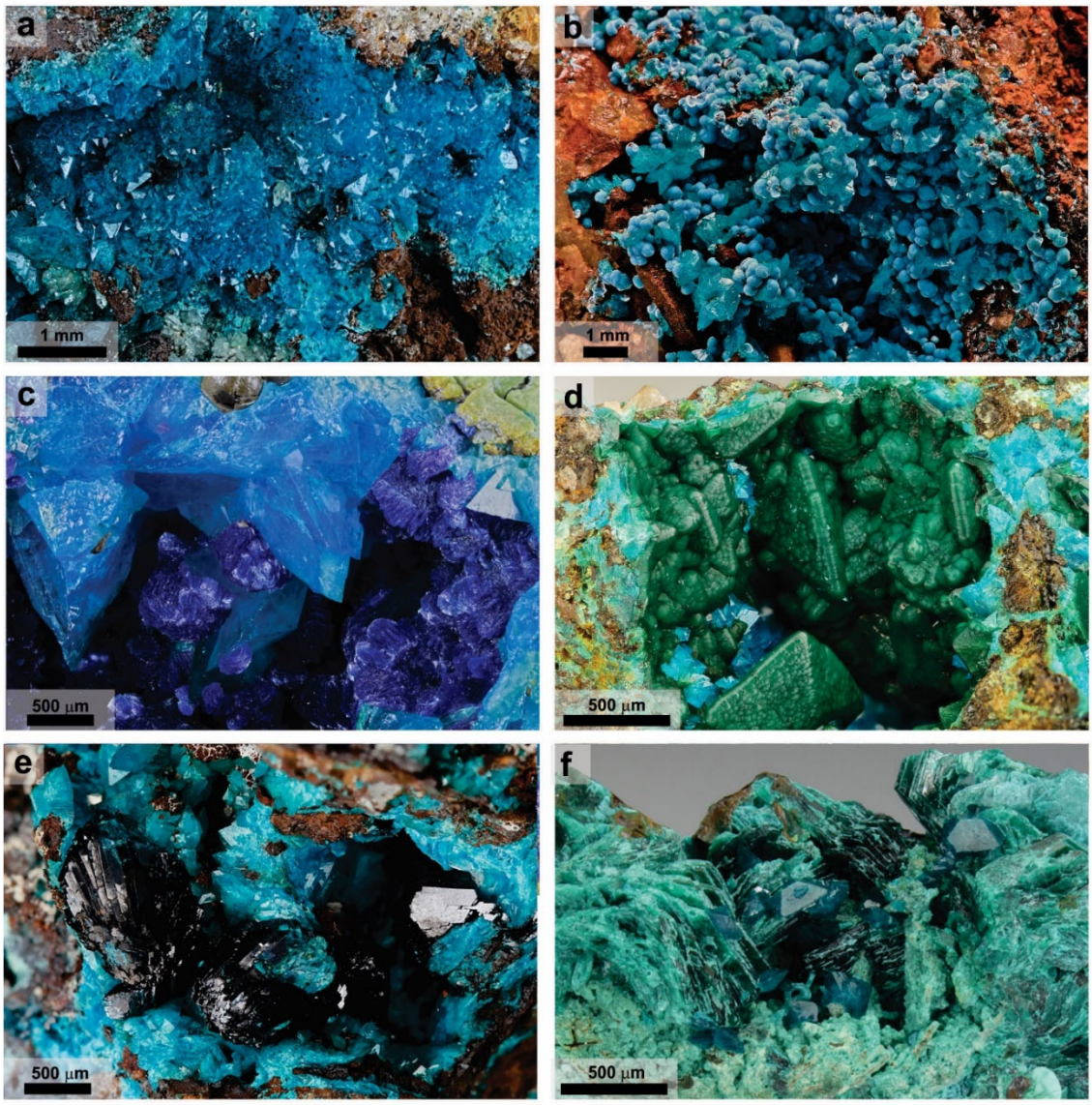

Figure 2-5. Liroconite growing on greenish scorodite. b) Ceruleite (spherical aggregates) with liroconite crystals. c) Liroconite overgrown by azurite crystals. d) Pseudomorphs of cornwallite after liroconite. e) Clinoclase growing on liroconite. f) crystals with chalcophyllite (greenish tabular crystals). All samples from Wheal Gorland, England.

Tang mine where azurite is especially common it may be older as well as younger than liroconite. Scorodite was only very rarely encountered in direct association with liroconite and is always older than liroconite (Fig. 2-5a).

Among the minerals associated with liroconite, accurate thermodynamic data are available for olivenite, azurite, and scorodite in particular. There are no data for some of the rarer minerals (e.g. parnauite, strashimirite) and they will not be considered further. Consider the dissolution reaction of liroconite,

$$Cu_2Al(AsO_4)(OH)_4{\cdot}4H_2O + 4H^+ \rightarrow 2Cu^{2+} + Al^{3+} + AsO_4^{3-} + 8H_2O \quad (1)$$

with log $K_1 = -4.85$. Combining with the dissolution reaction for olivenite (cf. Majzlan et al., 2015) gives a reaction that relates liroconite and olivenite,

$$Cu_2(AsO_4)(OH) + Al^{3+} + 7H_2O \rightarrow Cu_2Al(AsO_4)(OH)_4{\cdot}4H_2O + 3H^+ \quad (2)$$

with log $K_2 = -11.65$. The reaction quotient for this reaction is log $Q_2 = -3pH - \log a(Al^{3+})$.

In the acidic region, where Al^{3+} is the predominant Al(III) species, the concentrations of Al^{3+} necessary for the crystallization of liroconite, must be formidable. At pH = 3, for example, the equilibrium log $a(Al^{3+})$ = +2.6. The formation of liroconite under acidic conditions is essentially impossible. Using the equilibrium among the Al(III) species,

$$Al(OH)_3^0 + 3H^+ \rightarrow Al^{3+} + 3H_2O \quad (3)$$

with log K_3 = +16.17, the reaction can be rewritten as

$$Cu_2(AsO_4)(OH) + Al(OH)_3^0 + 4H_2O \rightarrow Cu_2Al(AsO_4)(OH)_4 \cdot 4H_2O \quad (4)$$

with log K_4 = +4.52 and log Q_4 = –log $a(Al(OH)_3^0)$. Hence, under circumneutral conditions, log $a(Al(OH)_3^0)$ = –4.52 for equilibrium between the two crystalline phases, both abundant at Wheal Gorland. This activity should be compared to activities expected when the aluminium solubility is controlled by common minerals. For gibbsite,

$$Al(OH)_3\ (cr,gibbsite) \rightarrow Al(OH)_3^0 \quad (5)$$

with log K_5 = –8.21 and log Q_5 = log $a(Al(OH)_3^0)$. This means that in the presence of gibbsite, the aluminium concentration should be much lower than that necessary for the crystallization of liroconite. Gibbsite may not directly precipitate from supersaturated aqueous solutions but X-ray amorphous Al oxides precipitate rapidly and may transform with time to gibbsite or a similar phase. These simple calculations hint that the formation of liroconite requires somewhat unusual conditions and explain its rarity. Fig. 2-6 shows that the aluminium concentrations, necessary for the crystallization of liroconite, are consistently several orders of magnitude higher than the aluminium solubility controlled by well crystallized gibbsite or even kaolinite. The Al(III) concentrations, needed to stabilize liroconite, are very close to Al(III) concentration needed to reach saturation with respect to X-ray amorphous $Al(OH)_3$. Herein lie the clues to the formation of liroconite and also to its rarity.

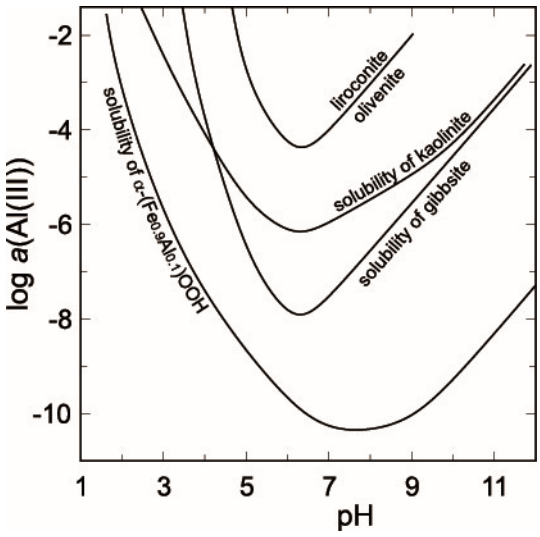

Figure 2-6. Solubilities of some common Al-Fe minerals, compared to the Al(III) concentrations needed to stabilize liroconite. All curves are calculated by PHREEQC (Parkhurst and Appelo, 1999). The curve for olivenite –liroconite was calculated by forcing a fluid to be in equilibrium with both phases simultaneously.

The granitic rocks in Cornwall are well known for their pervasive and deep kaolinization (e.g. Scott et al., 1996; Sheppard, 1977). An important observation is that kaolinization is especially intensive in the vicinity of the hydrothermal veins in the St Austell granite (Psyrillos et al., 1998), but this spatial association implies no genetic link. The much older veins and fracture zones provided channels for the weathering fluids. Sheppard (1977) wrote that "… the post-magmatic vein systems were critical in 'preparing the ground' for subsequent deep-weathering processes and generation of kaolinite". In a geochemical model of kaolinization (Psyrillos et al., 1998), feldspars were converted to assemblages of kaolinite, pyrophyllite or zeolite. The initial Al molality of the weathering fluids was set to 10^{-10} at pH = 5, much lower than that needed for the formation of liroconite. In this model, pyrophyllite was used as a representative mineral for the smectites which were also detected in the weathered rocks. We must also point out that Wheal Gorland is not located in the St Austell granite but in another outcropping granitic body in Cornwall that is even more rich in aluminium than the St Austell body (Charoy, 1986).

In the presence of a sufficient amount of dissolved silica, aluminium will be bound in minerals whose solubility is higher than that of gibbsite (Del Nero and Fritz, 1990), for example kaolinite or montmorillonite. Yet, for the formation of liroconite, even higher Al(III) concentrations than those controlled by kaolinite are needed (Fig. 2-6). Aqueous Al(III) concentrations, if controlled by montmorillonite, are higher than those for kaolinite, but still not sufficient for liroconite. According to Sheppard (1977) and Psyrillos et al. (1998), kaolinite formed in an environment rich in Al(III) and SiO_2(aq) at low temperatures (20 °C) and mildly acidic pH. Our calculations predict that the formation of kaolinite must have been preceded by the release of Al(III) and SiO_2(aq) from the rock-forming feldspars and precipitation of X-ray amorphous $Al(OH)_3$ as a precursor to kaolinite and gibbsite at Wheal Gorland. Only in this way could the Al(III) concentration have been sustained at levels high enough for precipitation of a large amount of liroconite.

An integral part of the model of Psyrillos et al. (1998) is the release of a large amount of SiO_2(aq). The dissolved silica must have been carried away because kaolinite veins contain neither quartz nor chalcedony. The modelled activities of SiO_2(aq) reached fairly high values, in some cases up to log $a(SiO_2(aq)) = -3.2$. The authors assert that the precipitation of quartz was kinetically hindered, even though supersaturation was reached (for quartz, saturation is reached at log $a(SiO_2(aq)) = -4.0$, for amorphous silica at log $a(SiO_2(aq)) = -2.7$). Under these conditions, two logical questions are whether the occurrence of copper silicates can be expected and why they are not reported from Wheal Gorland.

For dioptase, the dissolution reaction is

$$CuSiO_3 \cdot H_2O + 2H^+ \rightarrow Cu^{2+} + H_4SiO_4^0 \quad (6)$$

with log $K_6 = +3.78$, using the thermodynamic data for dioptase from Kiseleva et al. (1993). For this reaction, log $Q_6 = \log a(Cu^{2+}) + \log a(H_4SiO_4^0) + 2pH$.

Fixing log $a(Cu^{2+})$ at 10^{-4}, saturation would be reached at pH = 6 at log $a(H_4SiO_4^0)$ = –4.2 but at pH = 5 only at log $a(H_4SiO_4^0)$ = –2.2 (note that log $a(H_4SiO_4^0)$ = log $a(SiO_2(aq))$. Assuming that this copper activity is correct and the maximum activity of $SiO_2(aq)$ was that proposed by the models of Psyrillos et al. (1998), the formation of the main mass of liroconite at Wheal Gorland would have to be restricted to a narrow range of conditions between pH ≈ 5 (near the predominance field of $Al(OH)_3^0$ and precipitation of X-ray amorphous $Al(OH)_3$) and pH ≈ 6 (above which dioptase could precipitate). The conclusions regarding the formation conditions of dioptase conform to the results of Ingwersen (1990) who analysed the assemblages dioptase + azurite + malachite in Tsumeb (Namibia). He deduced that the environment conducive for the precipitation of dioptase is that with higher pH (8-9) and high copper and silica activities, typical for the silicified dolomitic rocks in Tsumeb. Such conditions were obviously not met at Wheal Gorland.

Another possible assemblage that does not occur in Wheal Gorland would be that of olivenite + mansfieldite. Its relationship to liroconite is expressed by

$$Cu_2Al(AsO_4)(OH)_4.4H_2O + H_2AsO_4^- + H^+ \rightarrow Cu_2(AsO_4)(OH) + AlAsO_4 \cdot 2H_2O + 5H_2O \quad (7)$$

with log K_7 = 14.48 and log Q_7 = pH – log $a(H_2AsO_4^-)$.

Liroconite is restricted to environments with higher pH and lower As(V) molalities (Fig. 2-7). At pH = 6, the log $a(H_2AsO_4^-) \approx$ –8.5, lower than expected for an oxidation zone with arsenates. This relationship suggests that pH may have been higher than 6 which is, however, not fully compatible with the formation conditions for kaolinite and possible precipitation for dioptase.

In summary, we propose that the main stages of the evolution of the oxidation zone in Wheal Gorland were contemporaneous with the pervasive kaolinization. The initial stages of weathering were probably marked by low pH, typical for initial sulfide weathering (so-called aggressive acid mine drainage), as witnessed by the older scorodite and pharmacosiderite. Fluctuations in the weathering and kaolinization intensity resulted in multiple liroconite generations, associated with

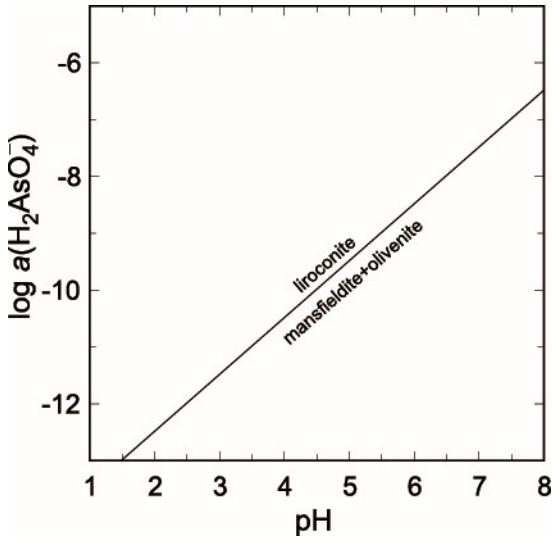

Figure 2-7. Stability fields of olivenite+mansfieldite versus liroconite, according to eq. 7 in text.

olivenite and other copper arsenates. They may have formed at mildly acidic to circumneutral conditions. Fluids were able to leach and remove SiO_2(aq) efficiently so that the amorphous $Al(OH)_3$ controlled the Al(III) solubility at high concentrations before the conversion of most Al and Si to kaolinite. This supposition is partially supported by the reports of gibbsite occurrence at Wheal Gorland (mindat.org) although the details are not known to us. On the other hand, pH and the Cu and SiO_2(aq) activities were kept below the threshold necessary for dioptase formation. The exhaustion of the acidity-generation capacity of the sulfides and cessation of kaolinization processes led to the terminal weathering stages, in near-neutral to mildly basic conditions with elevated $p(CO_2,g)$, with the resulting younger azurite. The meaning of the observation that the Cu–Al phases liroconite and chalcophyllite rarely occur together remains unclear. No information can be extracted from the other associated minerals as their formation conditions are unknown.

The evolution of an oxidation zone from strongly acidic to circumneutral or mildly basic values is a common phenomenon. Such evolution has been deduced for, among others, the copper-rich oxidation zones in Farbište (Slovakia) (Števko et al., 2011) or Bamba Kilenda (Congo) (Arne, 2014). The pH shift from early to mature stages also been observed also in general for oxidation zones generated by pyrite weathering (e.g. Jambor, 1994; Leverett et al., 2005; Velasco et al., 2013). It is interesting that kaolinite is mentioned repeatedly as a mineral associated with the weathering processes at sites worldwide (Leverett et al., 2005; Arne, 2014), but iron oxides may also be abundant. In that case, aluminium solubility could have been controlled by the AlOOH or Al_2O_3 component in the iron oxides. In addition, copper arsenates are particularly sensitive to the presence of other metal cations (e.g., Pb^{2+}) and are then replaced by Pb–Cu arsenates, such as in Tsumeb (Ingwersen, 1990). Hence, elevated concentrations of other metals (Fe^{3+}, Pb^{2+}, etc.) may hinder the crystallization of liroconite. In the case of Fe^{3+}, iron oxides control the Al solubility at very low concentrations. For Pb^{2+}, mixed Cu–Pb arsenates are preferred over Cu arsenates (see Ingwersen, 1990). The formation of liroconite requires circumneutral fluids in an Al-rich environment that is poor in Fe, Pb or other interfering metals.

2.6.2 Geminite: associated minerals and thermodynamic models

Despite the relatively large number of specimens, geminite belongs to less common arsenate minerals in Jáchymov, yet it has been reported in several distinctive weathering associations on different ore veins. Crystals used in the current study (Fig. 2-8a) were extracted from a specimen originating from the Geschieber vein at the Daniel adit level of the Svornost mine. The matrix is milky-white quartz without any sulfides. The supergene association is dominated by geminite, in prismatic crystals of greenish colour, with minor arsenolite and a sparse lavendulan. Lavendulan partly overgrows older geminite (Fig. 2-8b). The sources of Cu and As are probably tennantite, bornite and chalcocite, which occur in the vein nearby. Specimens with geminite were found on the floor of the adit and we conclude that Cu–As-bearing aqueous solutions were descending (dripping, flowing) down onto the floor from the parts of the vein and ore stope above. Similar

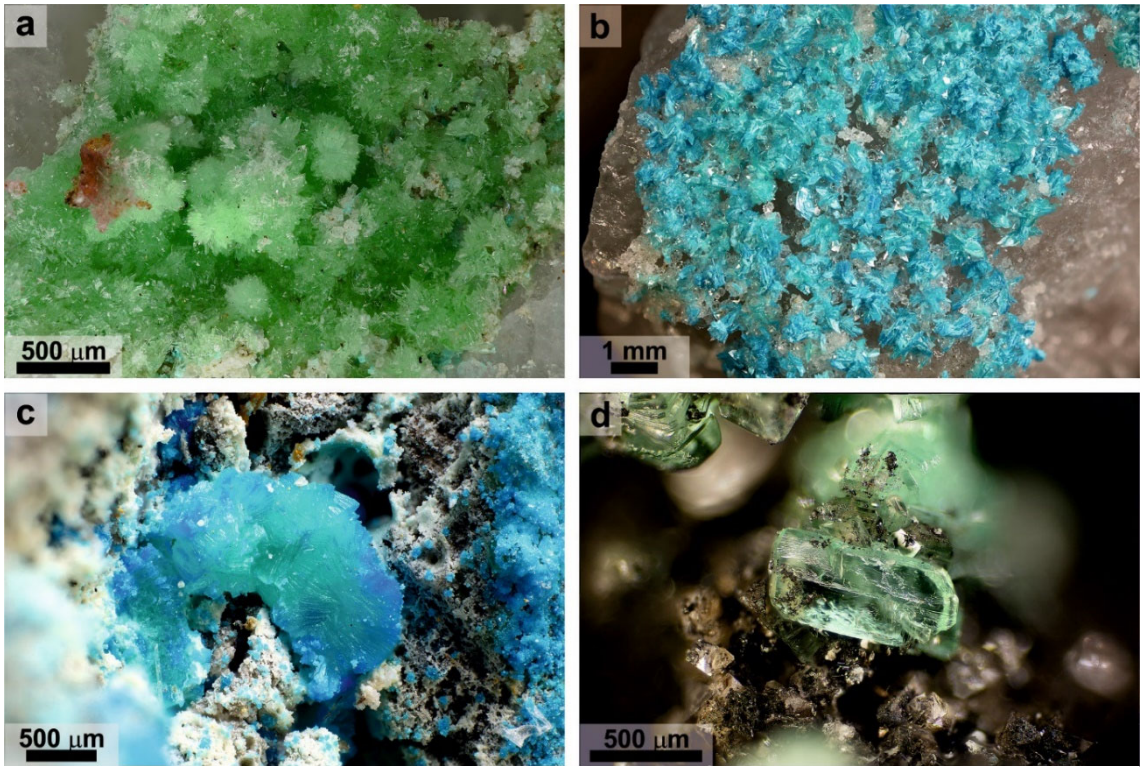

Figure 2-8. a) Geminite crystals on the milky-white quartz. Geschieber vein, Daniel level, Svornost mine, Jáchymov. b) Geminite crystals partially overgrown by bluish lavendulan. Matrix is represented by quartz. Geschieber vein, Daniel level, Svornost mine, Jáchymov. c) Geminite aggregate partially overgrown by bluish yvonite. White fine-grained phase is arsenolite. Giftkies adit, Jáchymov. d) Geminite crystal in a cavity of strongly altered native arsenic. Octahedral colourless crystals belong to arsenolite. Geister vein, sixth Geister level, Rovnost mine, Jáchymov. Photograph a) by Stephan Wolfsried and b-d) by Pavel Škácha.

mineral association has been encountered in the old mining workings of the Giftkies adit (Unruhe area, Jáchymov). Specimens containing geminite somewhat resemble those from the Svornost mine, but they contain fragments of surrounding mica schists and thinner white quartz veins. At Svornost, despite geminite being more common, it is only directly associated with arsenolite. On a few specimens from Giftkies, geminite is associated with additional yvonite (Fig. 2-8c).

The remainder of this association comprises lavendulan, slavkovite and cyanotrichite. In just one specimen, geminite forms directly upon/within weathered aggregates of tennantite. It is assumed that tennantite is the source of Cu and As. The third type of geminite occurrences in Jáchymov is its association with minor arsenolite on strongly weathered/corroded native arsenic (Fig. 2-8d). Such specimens originate from the Geister vein in the Rovnost mine in the western parts of the Jáchymov deposit. While the source of As is the native arsenic, Cu was probably derived from fine-grained tennantite that has been found in trace amounts within the massive arsenic.

In summary, geminite is a product of weathering of quartz–arsenic veins with minor amounts of other primary minerals. Carbonates are either not present or accessory. The most common minerals associated with geminite are arsenolite, gypsum, lavendulan and those of the lindackerite group.

The most faithful companion of geminite is arsenolite, with the dissolution reaction

$$As_2O_3\ (cr,arsenolite) + 3H_2O \rightarrow 2H_3AsO_3^0 \qquad (8)$$

with log K_8 = –1.37. At low pH, the solubility should therefore be remarkable and log $a(H_3AsO_3^0)$ = –0.69. Rough calculations, using the composition of sample J-2 in Majzlan et al. (2014a) show that log $a(H_3AsO_3^0)$ in this solution is +0.05. These calculations are only very approximate because the solution, with its high ionic strength (0.43 *m*), is well out of the range of applicability of the Debye–Hückel equation implemented in PHREEQC. Yet, they suggest that the solution is slightly supersaturated with respect to arsenolite, in good agreement with the field observations. We should also note that since the publication of Majzlan et al. (2014a), we were able to measure Eh in the field and input this value (pε = 9.63) into the PHREEQC calculations.

The second mineral that is close to saturation is gypsum, with a saturation index (SI) of –1.3 (slightly undersaturated). In the extremely acidic droplets with pH ~0, the concentration of sulfate reaches 30-50 g/L (Majzlan et al., 2014a), but it should be noted that the arsenate concentrations were about 10 times higher. A phase diagram for copper sulfates (Fig. 2-9) shows that under such conditions, all these phases are soluble. Upon slight pH increase, chalcanthite could precipitate but the solutions possess sufficient Ca to precipitate gypsum instead. Hence, even when pH should increase, the copper could not be scavenged and removed by sulfates. At higher pH and even moderate to low activity of Cu(II), devilline would be expected (Fig. 2-10) but does not occur in our samples from Jáchymov. The pH of these solutions was therefore maintained at very low values throughout the crystallization.

The droplets found directly on weathering arsenic (Majzlan et al., 2014a) certainly represent an extreme case of As enrichment and an environment conducive to the precipitation of arsenolite. Initially, most of the arsenic is found as As(III); X-ray absorption spectroscopy determined 87 % As(III) (Majzlan et al., 2014a) while thermodynamic predictions (PHREEQC) gave 64 %. The pentavalent arsenic is removed by minerals such as kaatialaite or the copper arsenates described here. Geminite is undersaturated (SI –5.2) in the acidic droplets but approaches saturation as more

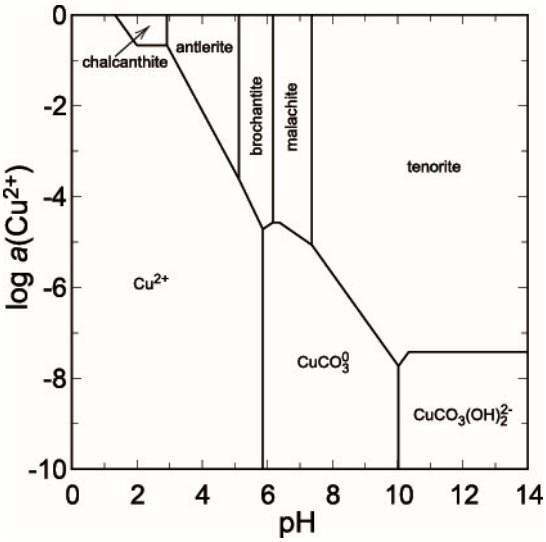

Figure 2-9. pε-pH diagram of the system CuO-SO_3-CO_2-H_2O for T = 298.15 K, log f(CO_2,g) = –2 and log a(S(VI)) = –2.

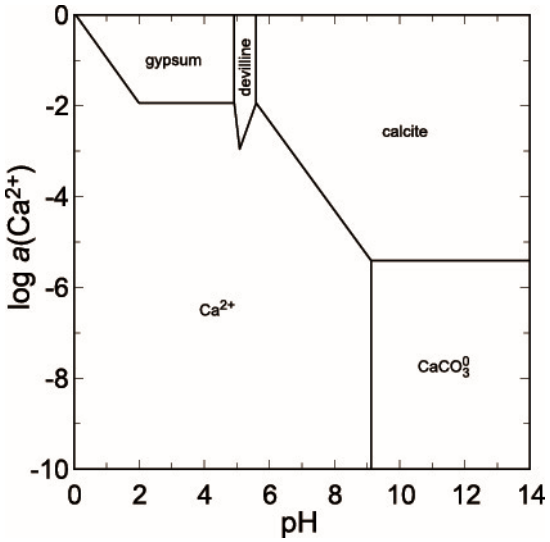

Figure 2-10. pε-pH diagram of the system CaO-CuO-SO_3-CO_2-H_2O for T = 298.15 K, log a(Cu(II)) = –2.5, log a(S(VI)) = –2.5, log a(HCO^{3-}) = –2.

As is oxidized or the solutions leach additional Cu from the primary ores. The dissolution reaction of geminite under acidic conditions is

$$Cu(H_2O)(AsO_3OH) + 2H^+ \rightarrow Cu^{2+} + H_3AsO_4^0 + H_2O \quad (9)$$

with $\log K_9 = 2.15$ and $\log Q_9 = \log a(Cu^{2+}) + \log a(H_3AsO_4^0) + 2pH$.

Although there are no thermodynamic data available for yvonite, slavkovite or lindackerite-group minerals, their chemical compositions attest that they are an integral part of the acidic assemblage with geminite. All of them contain protonated – acidic arsenate group in their formulae AsO_3OH (or $HAsO_4$), for slavkovite $Cu_{13}(AsO_4)_6(AsO_3OH)_4 \cdot 23H_2O$ (Sejkora et al., 2010a), for yvonite $Cu(AsO_3OH) \cdot 2H_2O$ (Sarp and Černý, 1998), and $ACu_4(AsO_4)_2(AsO_3OH)_2 \cdot 9H_2O$ for the lindackerite group, where A = Cu, Zn, Co, Ca, Ni, Mg, with lindackerite (Vogl, 1853), ondrušite (Sejkora et al., 2011), hloušekite (Plášil et al., 2014), and veselovskýite (Sejkora et al., 2010b) having their type locality in Jáchymov (see Škácha et al., 2019 for more information). From its type locality in the Salsigne mine (France, Sarp and Černý, 1998), yvonite was described in association with geminite, lindackerite, and pushcharovskite. All these minerals should be expected to crystallize from strongly acidic solutions, just like geminite. In agreement with the observations, the phase diagram shows a small field for geminite at very low pH and high Cu and As(V) molalities (Fig. 2-11).

Because carbonates are absent or extremely scarce, it has to be assumed that Ca in Jáchymov originated from acidic attack on rock-forming feldspars. This assumption is supported by the frequent presence of lavendulan for which Na is an essential component of its structure. In addition, Škácha et al. (2019) reported that many lavendulan specimens from Jáchymov contain an appreciable amount of K, hinting also at the dissolution of K-feldspars.

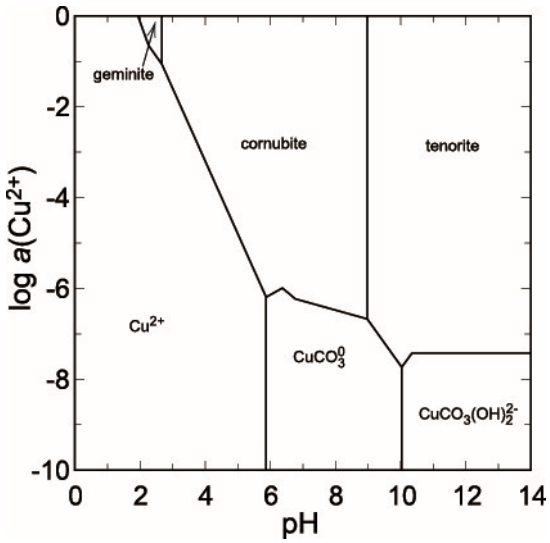

Figure 2-11. pε-pH diagram of the system CuO-As_2O_5-H_2O for T = 298.15 K, log $f(CO_2,g)$ = –2, log a(As(V)) = –2, olivenite is suppressed from the calculations.

2.6.3 Pushcharovskite: associated minerals and thermodynamic models

So far only two localities of pushcharovskite are known. The first is the type locality Cap Garonne, Var, France, where it is associated with geminite, lindackerite, yvonite and mahnertite in quartz gangue (Sarp and Sanz-Gysler, 1997). Pushcharovskite is also found in Salsigne in Aude, France, where it is associated with geminite, lindackerite and yvonite (Pushcharovsky et al., 2000).

Pushcharovskite is a higher hydrate of geminite, with the appropriate simple chemical reaction

$$Cu(AsO_3OH)\cdot H_2O + 0.5H_2O\ (g) \rightarrow Cu(AsO_3OH)\cdot 1.5H_2O \quad (10)$$

with $\Delta_rG^o_{10}$ = +3.8 kJ/mol showing that geminite is the stable phase even under standard conditions, that is, water vapour as an ideal gas with fugacity of 1 bar. In order to stabilize pushcharovskite, the pressure of water vapour and the relative air humidity would have to reach huge values which are not even worth discussion. The situation somewhat resembles the relationship between olivenite and euchroite

$$Cu_2(AsO_4)(OH) + 3H_2O\ (g) = Cu_2(AsO_4)(OH)\cdot 3H_2O \quad (11)$$

with $\Delta_rG^o_{11} = -13.4\ kJ\cdot mol^{-1}$,and calculated relative air humidities for equilibrium at near-surface conditions of 400 % (Majzlan et al., 2017b). Hence, pushcharovskite can be seen as a metastable precursor to geminite which is itself metastable with respect to olivenite but probably forms faster under acidic conditions. Because of its marked metastability, pushcharovskite should only be a transient phase that rapidly dehydrates to geminite. That would also explain its extreme rarity in nature.

2.7 Acknowledgements

We thank Taras L. Panikorovskii and the one anonymous reviewer for their constructive reviews. The work presented here was financially supported by a grant of the *Deutsche Forschungsgemeinschaft* MA 3927/26-1. Part of the research was supported through project no. 17-09161S of the Czech Science Foundation to JP and JS.

Data availability

The underlying research data are available at https://doi.org/10.22032/dbt.41075 (Plumhoff and Majzlan, 2020).

Supplement

The supplement related to this article is available online at: https://doi.org/10.5194/ejm-32-285-2020-supplement.

Author contributions

AMP conducted the research and investigation process, specifically performing the experiments and data collection for powder-X-ray diffraction, ICP-OES, FT-IR and acidsolution calorimetry. JP provided the natural sample of geminite and collected and described the single-crystal X-ray data. Additionally, he wrote parts about mineral associations of geminite. JS provided the natural sample of liroconite and collected and processed the electron microprobe analyses. ED and AB collected and processed the data of the relaxation and differential scanning calorimetry. MS and MSR wrote parts about the mineral associations where they have special knowledge. JM was responsible for the conceptualization, funding acquisition and the supervision. AMP prepared the initial draft and following manuscript with contributions from all co-authors.

Review statement

This paper was edited by Giuseppe Cruciani and reviewed by Taras Panikorovskii and one anonymous referee.

.

3 Thermodynamic properties and crystal structure of adamite [$Zn_2(AsO_4)(OH)$], zincolivenite [$CuZn(AsO_4)(OH)$] and the solid solution series olivenite [$Cu_2(AsO_4)(OH)$] – libethenite [$Cu_2(PO_4)(OH)$]

Alexandra M. Plumhoff[1*], Juraj Majzlan[1]

[1]Institute of Geosciences, Friedrich-Schiller University, Burgweg 11, 07749 Jena, Germany

3.1 Abstract

Adamite [$Zn_2(AsO_4)(OH)$], zincolivenite [$CuZn(AsO_4)(OH)$] and a complete solid solution series between olivenite [$Cu_2(AsO_4)(OH)$] and libethenite [$Cu_2(PO_4)(OH)$] were successfully synthesized and characterized by powder X-ray diffraction, infrared spectroscopy and optical emission spectrometry. The enthalpies of formation were determined by acid-solution calorimetry and resulted in Δ_fH^o (all values in $kJ \cdot mol^{-1}$ and $2\sigma = 3.2$) of –1401.7, –1211.6, –997.3, and –1384.4, for adamite, zincolivenite, olivenite and libethenite, respectively. The unit cell parameters of the olivenite–libethenite solid solution series, $Cu_2(PO_4)_x(AsO_4)_{1-x}(OH)$ [$0 \leq x \leq 1$], show a development following the size of the ionic radii from phosphor to arsenic as well as the bands of the infrared spectroscopy. The calculated ΔH^{MIX} values are positive for all values of X_{lib} with a maximum value around $X_{lib} = 0.59$ and a distinct step between $X_{lib} = 0.69$ and 0.79 which indicates the change in the crystal structure from monoclinic (olivenite) to orthorhombic (libethenite). Together with the thermodynamic excess properties of the olivenite–libethenite solid solution, we present a complete solid solution series without miscibility gap which shows an easier incorporation of phosphor than for arsenic.

3.2 Introduction

Adamite [$Zn_2(AsO_4)(OH)$], zincolivenite [$CuZn(AsO_4)(OH)$], olivenite [$Cu_2(AsO_4)(OH)$] and libethenite [$Cu_2(PO_4)(OH)$] belong to the libethenite group (Strunz and Nickel, 2001) with a general formula $M_2(XO_4)(OH)$ (M = Cu, Zn; X = P, As). The cations on the M site can be further substituted by e.g. Fe(II), Co(II), Mn(II). Minerals of the libethenite group occur mainly in the oxidation zone of polymetallic deposits enriched in copper and zinc and extensive substitution is recorded for this quaternary system (e.g., Braithwaite, 1983; Anthony et al., 2000; Braithwaite et al., 2005). Solid solutions of these minerals occur in a variety of geological settings but mainly in the oxidised zones of sulphide ore bodies, the composition being controlled by the physicochemical environment during mineral formation.

All minerals in the group except olivenite crystallize in the orthorhombic space group *Pnnm* (Hill, 1976; Kato and Miúra, 1977; Cordsen, 1978; Toman, 1978; Chukanov et al., 2007; Zema et al., 2010; Jinnouchi et al., 2016; Števko et al., 2017). Olivenite is the only mineral of this group with monoclinic space group $P2_1/n$, although the monoclinic angle is close to 90° (Toman, 1977; Burns and Hawthorne, 1995b; Li et al., 2008; Tarantino et al., 2018; Kösters et al., 2020). Natural samples of olivenite–libethenite show a small compositional gap (Szakáll et al., 1994; Jansa et al., 1998; Gołębiowska et al., 2006; Sejkora et al., 2006; Williams et al., 2006; Sejkora et al., 2008; Lafuente et al., 2015; Majzlan et al., 2015). Interestingly, Williams (1990) already mentioned complete miscibility between the phosphate and arsenate anions, giving their identical charge (-3) and similar radius of the [AsO_4] (248 pm) and [PO_4] (238 pm) tetrahedron. The mimetite–pyromorphite ($Pb_5(AsO_4)_3Cl$–$Pb_5(PO_4)_3Cl$) series as well as the cornwallite–pseudomalachite ($Cu_5(AsO_4)_2(OH)_4$–$Cu_5(PO_4)_2(OH)_4$) series are two well-known examples of a complete arsenate-phosphate solid solution (Markl et al., 2014; Ciesielczuk et al., 2016). Only a partial solid solution is confirmed for the olivenite–libethenite series in natural and synthetic samples so far (Szakáll et al., 1994; Gołębiowska et al., 2006; Sejkora et al., 2006; Williams et al., 2006; Sejkora et al., 2008; Majzlan et al., 2015). The olivenite–adamite solid solution was also documented by analyses of both natural and synthetic samples (Guillemin, 1956; Minčeva-Stefanova, 1964; Toman, 1978; Braithwaite, 1983; Gołębiowska et al., 2006; Southwood et al., 2020). There is an intermediate, ordered phase between olivenite and adamite, zincolivenite, with a suggested compositional range of $Cu_{0.5}Zn_{1.5}(AsO_4)(OH)$–$Cu_{1.5}Zn_{0.5}(AsO_4)(OH)$ (Chukanov et al., 2007). Toman (1978) showed that the symmetry change from monoclinic (olivenite) to orthorhombic (adamite) occurs at approximately 0.8 Cu/(Cu+Zn) (molar ratio).

In spite of the considerable amount of previous work on the libethenite group minerals, there are some points of interest which deserve further study. In this work, we synthesized the complete olivenite–libethenite solid solution series, adamite and zincolivenite. All phases were characterized by X-ray powder diffraction, Fourier-transform infrared spectroscopy and inductively coupled optical emission spectroscopy. Enthalpies of formation were measured by

acid-solution calorimetry and the standard entropies were estimated. Additionally, the thermodynamic mixing properties of the olivenite–libethenite solid solution were calculated.

3.3 Materials

Adamite was synthesized by a modified wet chemical method after Keller (1971). All solutions were prepared with deionized water. The starting solutions of 100 mL of 0.025 M KH_2AsO_4 and 100 mL 0.025 M $ZnSO_4$ were filled into a boro-silicate bottle and heated to 80 °C under constant stirring. pH was adjusted to 8 with 4% NaOH solution. The bottle was closed and placed into an oven at 80 °C for seven days. The final product was filtered hot, washed several times with deionized water and air dried at ambient temperature. Zincolivenite was synthesized with the same procedure as adamite, except the starting solutions were 100 mL of 0.025 M KH_2AsO_4, 50 mL 0.0125 M $ZnSO_4$ and 50 mL 0.0125 M $CuSO_4$, the pH was adjusted to 7 and it had to be placed in the oven for ten days.

All phases from the olivenite–libethenite solid solution were synthesized by a wet chemical procedure using analytical reagent grade chemicals. The syntheses were prepared to reach 100 mL of final solution by mixing 50 mL of 0.5 M $Cu(NO_3)_2$ solution with 50mL of a solution with $(NH_4)H_2PO_4$ and Na_2HAsO_4, in different proportions (Table 3-1). All reagents were dissolved in deionized water. For the synthesis of the end members, 50 mL of 0.5 M $Cu(NO_3)_2$ solution were mixed with 50 ml of 0.32 M $(NH_4)H_2PO_4$ solution for libethenite and 50 mL 0.19 M Na_2HAsO_4 solution for olivenite. For the intermediate members of the solid solution, prepared solutions of $(NH_4)H_2PO_4$ and Na_2HAsO_4 were mixed together in desired proportions, stirred and added to 50 mL of $Cu(NO_3)_2$ solution. The final solutions were stirred constantly while heating up to 70 °C and adjusting the pH to 3 using $(NH_4)OH$ (28-30 % NH_3). After stabilization of the pH, the used boro-silica bottles were closed and placed in a water bath with constant temperature of 70 °C controlled by thermostat. The pH was controlled and raised with $(NH_4)OH$

Table 3-1. Calculated quantities of reagents necessary for the synthesis of the olivenite-libethenite solid solution. H_2O = deionized water.

	$(NH_4)H_2PO_4$ [g]	H_2O [mL]	$Na_2HAsO_4 \cdot 7H_2O$ [g]	H_2O [mL]
olivenite	-	-	5.0550	50
10P90As	0.1866	25	4.5495	25
20P80As	0.3729	25	4.0439	25
30P70As	0.5593	25	3.5384	25
40P60As	0.7456	25	3.0329	25
50P50As	0.9319	25	2.5274	25
60P40As	1.1182	25	2.0218	25
70P30As	1.3045	25	1.5163	25
80P20As	1.4909	25	1.0108	25
90P10As	1.6772	25	0.5052	25
libethenite	1.8635	50	-	

(28-30 % NH_3) every few hours. After four days, the resulting suspension was filtered hot, washed several times with deionized water and air dried at ambient temperature.

3.4 Methods

All samples were identified with a powder X-ray diffractometer (pXRD) Bruker D8 Advance, employing CuKα radiation (λ = 1.54058 Å). The diffraction patterns were collected at room temperature between 5 and 120° 2θ, with a step size of 0.01 °2θ, and a time per step of 1.0 s. Indexing of the main reflections and lattice parameters were refined with the software JANA2006 (Petříček et al., 2014). Additionally, to examine the presence of possible compositional heterogeneities in the solid solution phases, the peak widths were analysed by considering the full width at half maximum intensity values (FWHM) of the two strongest (1 1 0 and 1 0 1) diffraction peaks. The values were determined after profile fitting to a Lorentzian function. Broadening effects can be attributed either to compositional heterogeneities, the presence of small crystallites (the size of the coherently diffracting domain) or lattice distortions. Heterogeneity can be assessed by comparing the FWHM values of the intermediate $Cu_2(PO_4)_x(AsO_4)_{1-x}(OH)$ phases relative to the equivalent reflections of the two end members. Since the pure $Cu_2(AsO_4)(OH)$ and $Cu_2(PO_4)(OH)$ phases are homogeneous in composition, any broadening effects observed in their diffraction peaks can only be ascribed to a crystallite size effect or strain. The crystallite size of all phases was roughly estimated using the Scherrer equation $L = \frac{K\lambda}{\beta \cos(\theta)}$ with L as crystallite size, the Scherrer constant K = 0.9, λ = 1.54058 Å, β as FWHM in radians and θ as peak position in radians.

The elemental composition of the fine-grained samples was analysed with a simultaneous radial inductively coupled optical emission spectrometer (ICP-OES) 725ES (Agilent, Germany) with CCD-detector and an ASX 520 autosampler (Teledyne CETAC, Omaha, USA). The sample (~10 mg) was dissolved in 10 mL of 20% HNO_3.

Fourier-transform infrared (FT-IR) transmission spectra were recorded using a Nicolet iS10 spectrometer (Thermo Fisher Scientific, Germany). The powdered samples (1-2 mg) were mixed with KBr (FT-IR spectroscopy grade, Merck), gently ground and pressed to pellets. The pellets were measured at wavenumbers from 4000 to 400 cm^{-1} with 64 scans per spectrum at a resolution of 4 cm^{-1}. The spectra were normalized to maximum intensity.

For the calorimetric experiments, we used a commercial IMC-4400 isothermal micro calorimeter (Calorimetry Sciences Corporation), modified for the purposes of acid-solution calorimetry (Majzlan, 2017a). The liquid water bath of the calorimeter is held at constant temperature of 298.15 K with fluctuations smaller than 0.0005 K. The calorimetric solvent was 25 g of 5 N HCl and is contained in a polyetheretherketone (PEEK) cup with a total volume of 60 mL. The PEEK cup is then closed with a PEEK screw lid and inserted into the calorimeter well. The calorimeter stabilizes after ~8 hours. During the stabilization and the experiment, the solvent is stirred by a

SiO_2 glass stirrer by a motor positioned about 40 cm from the active zone of the instrument. The samples were pressed into a pellet and weighed on a micro-balance with a precision of 0.002 mg. The pellets are then dropped through an SiO_2 glass tube into the solvent and the heat produced or consumed during the dissolution was measured. The heat flow between the reaction cup and the constant temperature reservoir was then integrated to calculate the caloric effect. A typical experiment lasts 60-80 minutes and the end of the experiments is judged from the return of the baseline to the pre-experiment position (Majzlan, 2017).

3.5 Results and discussion

In the following sections, the term "end members" will be applied to the end members libethenite, olivenite, adamite and the intermediate ordered phase zincolivenite since these are all IMA-approved minerals. The starting model for refinement of the libethenite structure was *Pnnm* (a,b,c; cell choice 1) by Cordsen (1978), but the setting was changed to *Pnnm* (b,a,-c; cell choice 2) in order to preserve a simple relationship with the monoclinic unit cell of olivenite, so that variations in unit cell parameters show the effect of the substitution.

Table 3-2. Unit cell parameters for olivenite [$Cu_2(AsO_4)(OH)$], libethenite [$Cu_2(PO_4)(OH)$], adamite [$Zn_2(AsO_4)(OH)$] and zincolivenite [$CuZn(AsO_4)(OH)$] from this work, compared to values from studies on natural material.

	a [Å]	*b* [Å]	*c* [Å]	α [°]	V[Å³]	SG
olivenite						
synthetic, this work	8.6426(1)	8.2459(1)	5.9422(1)	90.061(3)	423.4(1)	$P2_1/n$
Kösters et al. (2020)	8.6188(9)	8.2269(6)	5.9406(9)	90.000(6)	421.2	$P2_1/n$
Li et al. (2008)	8.5844(3)	8.2084(3)	5.9258(2)	90.130(2)	417.6(1)	$P2_1/n$
Burns and Hawthorne (1995)	8.5894(2)	8.2073(2)	5.9285(1)	90.088(3)	-	$P2_1/n$
Toman (1977)	8.615(5)	8.240(6)	5.953(4)	90.0(1)	422.6	$P2_1/n$
libethenite						
synthetic, this work	8.0630(2)	8.4035(2)	5.8881(2)		399.0(1)	*Pnnm*
Števko et al. (2017)	8.062(1)	8.393(2)	5.885(1)		398.2(1)	*Pnnm*
Zema et al. (2010)	8.0614(2)	8.3972(2)	5.8870(1)		398.5(1)	*Pnnm*
Cordsen (1978)	8.062(5)	8.384(4)	5.881(2)		397.5	*Pnnm*
adamite						
synthetic, this work	8.3191(4)	8.5334(5)	6.0551(3)		429.8(1)	*Pnnm*
Jinnouchi et al. (2016)	8.343(2)	8.566(1)	6.076(1)		434.3(1)	*Pnnm*
Kato and Miúra (1977)	8.386(5)	8.552(4)	6.036(4)		-	*Pnnm*
Hill (1976)	8.306(4)	8.524(6)	6.043(3)		427.9	*Pnnm*
zincolivenite						
synthetic, this work	8.4018(5)	8.4951(6)	5.9818(3)		427.0(1)	*Pnnm*
Chukanov et al. (2007)	8.583(2)	8.529(2)	5.970(1)		437.1(1)	*Pnnm*
Toman (1978)	8.50	8.52	5.99		433.8	*Pnnm*

3.5.1 Structure and composition of end members

All studied end member samples consist of one single phase. The refined lattice parameters (Table 3-2) compare well to values from studies on natural materials. For olivenite, the non-standard choice of the space group (e.g. Toman, 1977) with α as the monoclinic angle was retained. The compositions determined by ICP-OES are shown in Table 3-3. The Cu, As and P contents of olivenite and libethenite lead to $Cu_{2.06}(As_{0.94}O_4)(OH)$ and $Cu_{2.05}(P_{0.95}O_4)(OH)$, respectively. The deviations of the stoichiometric coefficients of Cu from 2 and As, P from 1 are within analytical uncertainties. For calorimetry, we adopt the ideal formulae $Cu_2(AsO_4)(OH)$ and $Cu_2(PO_4)(OH)$ with the corresponding molecular masses of 283.017 g·mol^{-1} and 239.069 g·mol^{-1}, respectively. The Cu, Zn and As contents of adamite and zincolivenite lead to $Zn_{2.06}(As_{0.94}O4)(OH)$ and $Cu_{0.99}Zn_{1.08}(As_{0.93}O_4)(OH)$, respectively. The deviations for the stoichiometric coefficients of Cu, Zn and As are within analytical uncertainties. For calorimetry, we adopt the formulae $Zn_2(AsO_4)(OH)$ and $Cu_{0.95}Zn_{1.05}(AsO_4)(OH)$ with the corresponding molecular mass of 286.685 g·mol^{-1} and 284.943 g·mol^{-1}.

Table 3-3. ICP-OES analyses of the end members adamite and zincolivenite as well as the solid solution series olivenite–libethenite.

	weight %			atoms per formula unit				
	Cu	**Zn**	**As**	**Cu**	**Zn**	**As**	**Cu**	**Zn**
adamite	-	47.69	25.03	-	2.06	0.94	-	2.00
zincolivenite	22.52	24.95	25.87	0.99	1.08	0.93	0.95	1.05
	Cu	**P**	**As**	**Cu**	**P**	**As**	**P**	**As**
olivenite	47.88	-	25.88	2.06	-	0.94	-	1.00
10P90As	49.08	1.07	23.80	2.06	0.09	0.85	0.10	0.90
20P80As	50.45	2.23	21.91	2.06	0.19	0.76	0.20	0.80
30P70As	49.81	3.34	19.34	2.05	0.28	0.67	0.29	0.71
40P60As	52.47	4.46	16.75	2.08	0.36	0.56	0.39	0.61
50P50As	50.94	5.80	14.40	2.04	0.48	0.49	0.49	0.51
60P40As	52.23	6.93	11.65	2.05	0.56	0.39	0.59	0.41
70P30As	54.35	8.28	8.98	2.07	0.65	0.29	0.69	0.31
80P20As	56.53	9.68	6.05	2.08	0.73	0.19	0.79	0.21
90P10As	57.45	11.72	3.24	2.05	0.86	0.10	0.90	0.10
libethenite	54.93	12.36	-	2.05	0.95	-	1.00	-
				normalized to 3			normalized to 1	

The FT-IR spectra of all end members from this work (Figure 3-1) are comparable to the ones shown in Chukanov (2014). Additionally, the spectrum of olivenite is similar to the one shown in Martens et al. (2003), the spectrum of libethenite to the one in Martens and Frost (2003), the spectrum of zincolivenite to the one in Chukanov et al. (2007) and the spectrum of adamite to the one of Hill (1976). For all spectra, some of the weak bands described by these authors are not seen in our spectra but the strong bands are comparable. Bands observed in the range of 400 to 560 cm^{-1} are assigned to bending vibrations of the AsO_4 groups and in the range of 750 to 945 cm^{-1} to AsO_4 stretching vibrations (Frost et al., 2002; Martens et al., 2003). The band around 945 cm^{-1} is only visible for olivenite and is shifting towards lower wave numbers , around

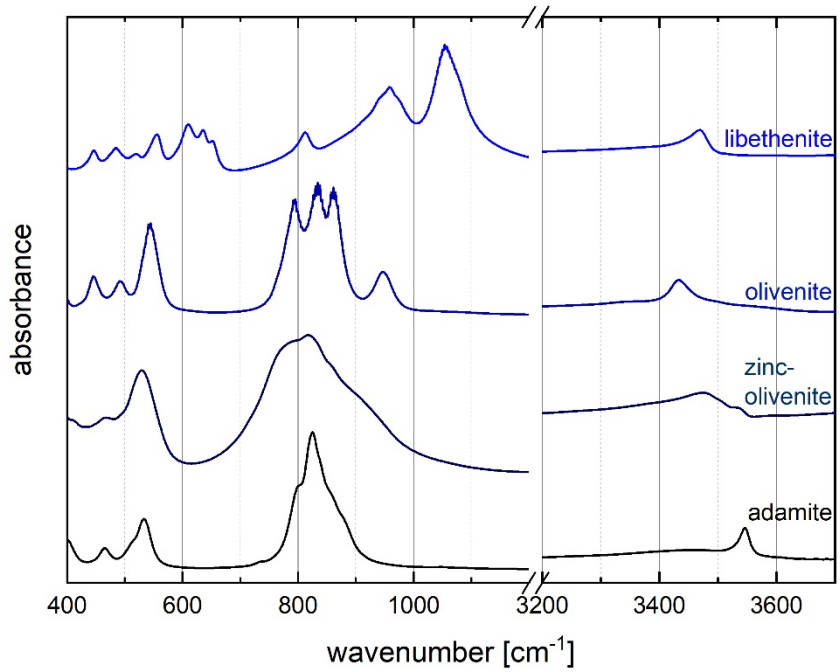

Figure 3-1. FT-IR spectra of the end members libethenite, olivenite, zincolivenite and adamite.

850 cm^{-1}, with higher Zn content (Braithwaite, 1983; Gołębiowska et al., 2006). The band around 3430 cm^{-1} for olivenite is attributed to the OH bending mode of water (Martens et al., 2003), whereas the bands around 3470 cm^{-1} and 3540 cm^{-1} for zincolivenite and adamite are assigned to OH stretching vibrations (Hill, 1976; Chukanov, 2014). Bands around 958 cm^{-1} and 1056 cm^{-1} are assigned to the symmetric and asymmetric stretching vibrations of the PO_4 groups (Martens and Frost, 2003). The bands of the OH stretching vibrations in libethenite are around 3470 cm^{-1} (Martens and Frost, 2003).

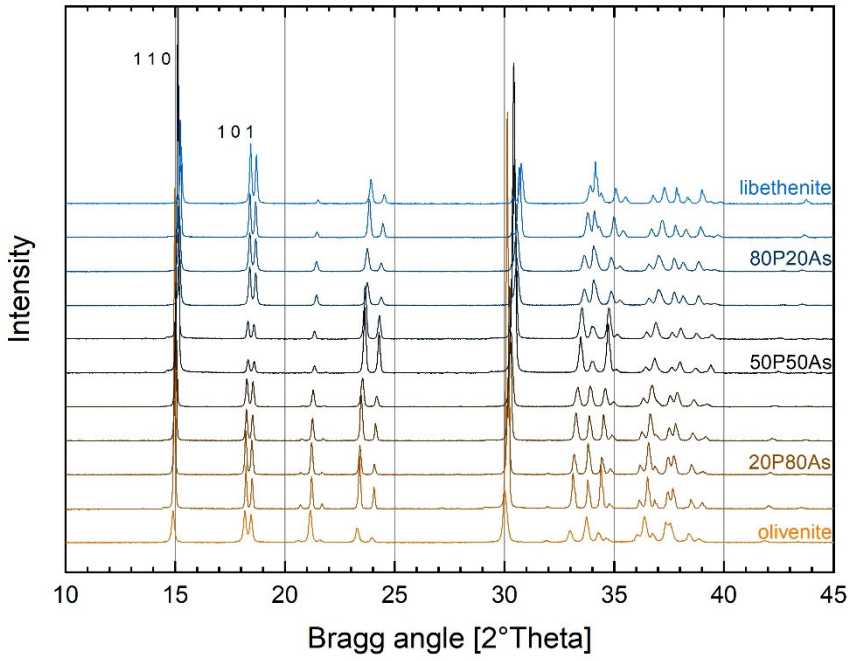

Figure 3-2. Powder XRD patterns of the solid solution series olivenite-libethenite. e.g. 20P80As = $Cu_2(PO_4)_{0.2}(AsO_4)_{0.8}(OH)$

Table 3-4. Unit cell parameters for the solid solution series olivenite–libethenite.

	a [Å]	*b* [Å]	*c* [Å]	α [°]	V[Å³]	SG
olivenite	8.6426(1)	8.2459(1)	5.9422(1)	90.061(3)	423.4(1)	$P2_1/n$
10P90As	8.6072(2)	8.2212(2)	5.9358(2)	90.094(2)	420.0(1)	$P2_1/n$
20P80As	8.5838(2)	8.2006(2)	5.9271(1)	90.094(1)	417.2(1)	$P2_1/n$
30P70As	8.5651(3)	8.1825(3)	5.9219(3)	90.088(3)	415.0(1)	$P2_1/n$
40P60As	8.5498(1)	8.1718(1)	5.9204(1)	90.073(4)	413.6(1)	$P2_1/n$
50P50As	8.5265(2)	8.1527(2)	5.9235(3)	90.171(5)	411.8(1)	$P2_1/n$
60P40As	8.5013(2)	8.1332(2)	5.9125(2)	90.111(5)	408.8(1)	$P2_1/n$
70P30As	8.4896(2)	8.1265(2)	5.9093(1)	90.011(7)	407.7(1)	$P2_1/n$
80P20As	8.4630(2)	8.1085(3)	5.9070(2)		405.4(1)	*Pnnm*
90P10As	8.4379(2)	8.0886(2)	5.8989(1)		402.6(1)	*Pnnm*
libethenite	8.4035(2)	8.0630(2)	5.8881(2)		399.0(1)	*Pnnm*

3.5.2 Structure and composition of the olivenite–libethenite solid solution

Figure 3-2 shows pXRD patterns of members of the olivenite–libethenite solid solution series. They show systematic changes with variable P/(P+As) ratio, namely peak shift to higher angle with increasing P^{5+} content. This shift occurs because the unit cell shrinks as a result of substitution of As^{5+} by the smaller P^{5+}. The unit cell parameters and volume (Table 3-4, Figure 3-3) reflect these systematic changes and change linearly with composition. This result is in good agreement with the trend in radius getting smaller from As^{5+} with 0.335 Å to P^{5+} with 0.17 Å. The studied phases were also checked for compositional homogeneity by considering the broadening of the powder diffraction peaks corresponding to the 1 1 0 and 1 0 1 reflection. The FWHM of the 1 1 0 reflection was 0.145 (°2θ) for pure olivenite (x=0) and 0.095 (°2θ) for pure libethenite (x=1). Since the pure end member phases are homogeneous in composition, the large difference

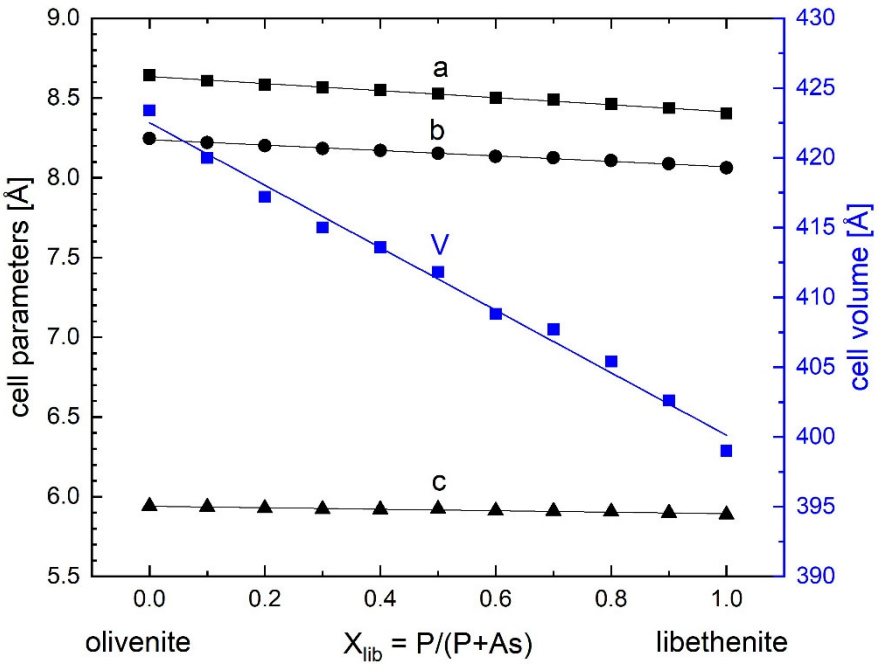

Figure 3-3. Evolution of the lattice parameters and cell volume for $Cu_2(PO_4)_x(AsO_4)_{1-x}(OH)$ [0≤x≤1] from Rietveld refinement (error bars are smaller than symbols).

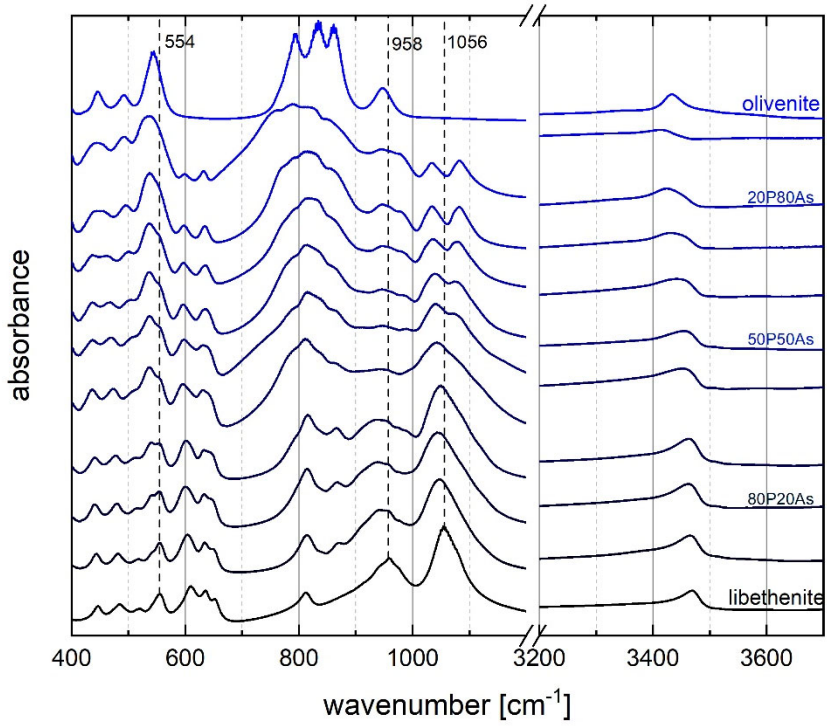

Figure 3-4. FT-IR spectra of the solid solution series olivenite-libethenite. e.g. 20P80As = $Cu_2(PO_4)_{0.2}(AsO_4)_{0.8}(OH)$

between these values can most probable be attributed to changes in crystallite size. The same is true of the 1 0 1 reflection (FWHM of 0.146 and 0.106 (°2θ) for the pure olivenite and libethenite -phase, respectively). Based on the FWHM of the five strongest reflections below 25 °2θ, the crystallite sizes were estimated to be 103.2 ± 12.0 nm for pure olivenite and 226.6 ± 34.4 nm for pure libethenite. The peak broadening varies in a regular way with the composition and can most probably be attributed to changes in the crystallite size, and thus compositional inhomogeneities can be considered irrelevant for the present purposes.

We were able to synthesize the olivenite-libethenite solid solutions series mixed phases in steps of 0.10 ± 0.01 apfu for the P and As content which was determined by ICP-OES is shown in Table 3-3.

Additionally, the infrared spectra of the olivenite–libethenite solid solution series are displayed in Fig. 3-4. The spectra of the solid solution phases show that some bands are moving due to the increasing As- or P-content. For example, the band around 1056 cm^{-1} is assigned to the asymmetric stretching vibrations of the PO_4 groups (Martens and Frost, 2003) and moves toward 1032 cm^{-1} with increasing As-content which indicates a change in the vibrational movement due to the increasing arsenic in the structure (Figure 3-5b). The same trend is shown for the band around 958 cm^{-1} which is assigned to the PO_4 symmetric stretching (Martens and Frost, 2003) with the difference that it moves towards 946 cm^{-1} (OH vibrations of olivenite, Martens et al., 2003). The overlapping of these two bands in the solid solution members leads to weak bands and displays as a plateau in the spectra. The bands of the Cu-O out-of-plane bending modes in the range from 541 to 555 cm^{-1} (Sumin de Portilla, 1974; Braithwaite, 1983; Martens et al., 2003;

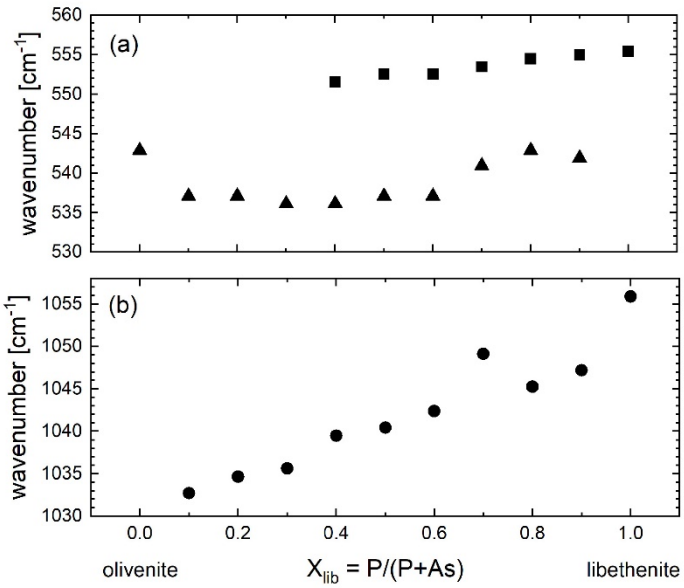

Figure 3-5. Positions of a) absorption maxima around 545 cm^{-1} and b) asymmetric stretching vibrations of the PO_4 groups in the FT-IR spectra of members of the olivenite–libethenite solid solution series.

Chukanov, 2014) show that the incorporation of an additional cation changes the bending behaviour (Figure 3-5a).

Additionally, the bands of the OH stretching vibrations are moving from 3470 cm^{-1} for libethenite to 3430 cm^{-1} for olivenite (Braithwaite, 1983; Martens and Frost, 2003; Martens et al., 2003).

3.5.3 Thermodynamic properties of end members

Enthalpies of formation

The enthalpies of formation of all studied phases were determined by acid solution calorimetry. Heat released or consumed by the system was measured by dissolving pellets of each sample in 5 N HCl. The reference compounds are needed to construct the thermodynamic cycle from which the enthalpies of formation will be determined. We used KCl, $HCl{\cdot}9.96H_2O$, KH_2AsO_4, KH_2PO_4, ZnO, CuO as the references; $HCl{\cdot}9.96H_2O$ is the composition of the calorimetric solvent, 5 N HCl. The choice of these reference compounds was explained, discussed and justified by Majzlan (2017a) and Majzlan et al. (2016). All compounds, including the studied samples, dissolved rapidly and completely, in the calorimetric solvent. Using thermochemical cycles (Table 3-5), based on the Hess' law, gave the enthalpies of formation summarized in Table 3-6.

Entropies

The entropies of the end members were calculated (Table 3-6) based on the Kopp rule stating that the entropy of a phase is simply the sum of entropies of its components. The components and their entropy are CuO (S^o = 42.6 $J{\cdot}mol^{-1}{\cdot}K^{-1}$), ZnO (43.2), P_2O_5 (114.4) (all Robie and Hemingway, 1995), As_2O_5 (105.44) (Nordstrom and Archer, 2003) and H_2O (ice, 41.94) (Majzlan et al., 2003).

Table 3-5. Thermochemical cycle for the studied minerals. x = P/(P+As). All enthalpies in kJ·mol^{-1}.

Reaction and reaction number	
KH_2AsO_4 (cr) = K^+ (aq) + 2 H^+ (aq) + AsO_4^{3-} (aq)	1a
KH_2PO_4 (cr) = K^+ (aq) + 2 H^+ (aq) + PO_4^{3-} (aq)	1b
ZnO (cr) + 2 H^+ (aq) = Zn^{2+} (aq) + H_2O (aq)	2a
CuO (cr) + 2 H^+ (aq) = Cu^{2+} (aq) + H_2O (aq)	2b
$HCl·9.96H_2O$ (l) = H^+ (aq) + Cl^- (aq) + $9.96H_2O$ (aq)	3
H_2O (l) = H_2O (aq)	4
KCl (cr) = K^+ (aq) + Cl^- (aq)	5
$Zn_2(AsO_4)(OH)$ (cr) = $2Zn^{2+}$ (aq) + AsO_4^{3-} (aq) + OH^- (aq)	6
$CuZn(AsO_4)(OH)$ (cr) = Cu^{2+} (aq) + Zn^{2+} (aq) + AsO_4^{3-} (aq) + OH^- (aq)	7
$Cu_2(AsO_4)(OH)$ (cr) = $2Cu^{2+}$ (aq) + AsO_4^{3-} (aq) + OH^- (aq)	8
$Cu_2(PO_4)_x(AsO_4)_{1-x}(OH)$ (cr) = $2Cu^{2+}$ (aq) + xPO_4^{3-} (aq) + $(1-x)AsO_4^{3-}$ (aq) + OH^- (aq)	9x
$Cu_2(PO_4)(OH)$ (cr) = $2Cu^{2+}$ (aq) + PO_4^{3-} (aq) + OH^- (aq)	10
K (cr) + As (cr) + H_2 (g) + $2O_2$ (g) = KH_2AsO_4 (cr)	11a
K (cr) + P (cr) + H_2 (g) + $2O_2$ (g) = KH_2PO_4 (cr)	11b
Zn (cr) + $(1/2)O_2$ (g) = ZnO (cr)	12a
Cu (cr) + $(1/2)O_2$ (g) = CuO (cr)	12b
10.46 H_2 (g) + 9.96 $(1/2)O_2$ (g) + $(1/2)Cl_2$ (g) = $HCl·9.96H_2O$ (l)	13
H_2 (g) + $(1/2)O_2$ (g) = H_2O (l)	14
K (cr) + $(1/2)Cl_2$ (g) = KCl (cr)	15
2Zn (cr) + As (cr) + $0.5H_2$ (g) + $2.5O_2$ (g) = $Zn_2(AsO_4)(OH)$ (cr)	16
Cu (cr) + Zn (cr) + As (cr) + $0.5H_2$ (g) + $2.5O_2$ (g) = $CuZn(AsO_4)(OH)$ (cr)	17
2Cu (cr) + As (cr) + $0.5H_2$ (g) + $2.5O_2$ (g) = $Cu_2(AsO_4)(OH)$ (cr)	18
2Cu (cr) + xP (cr) + (1-x)As (cr) + $0.5H_2$ (g) + $2.5O_2$ (g) = $Cu_2(PO_4)_x(AsO_4)_{1-x}(OH)$ (cr)	19x
2Cu (cr) + P (cr) + $0.5H_2$ (g) + $2.5O_2$ (g) = $Cu_2(PO_4)(OH)$ (cr)	20
ΔH_{1a} = 24.748 ± 0.181	Majzlan (2017)
ΔH_{1b} = 25.105 ± 0.332	Majzlan (2017)
ΔH_{2a} = -70.24 ± 0.11	Majzlan et al. (2016)
ΔH_{2b} = -51.526 ± 0.160	Majzlan (2017)
ΔH_3 = 0	dissolution of $HCl·9.96H_2O$ in $HCl·9.96H_2O$
ΔH_4 = -0.54	calculated from Parker (1965)
ΔH_5 = 17.693 ± 0.058	Majzlan (2017)
ΔH_6 = -47.046 ± 0.135	this work
ΔH_7 = -34.721 ± 0.189	this work
ΔH_8 = -25.202 ± 0.311	this work
ΔH_9 = see Table 3-6	this work
ΔH_{10} = -30.162 ± 0.143	this work
ΔH_{11a} = -1181.2 ± 2.0	Majzlan (2011)
ΔH_{11b} = -1573.6 ± 1.0	Majzlan (2011)
ΔH_{12a} = -350.5 ± 0.3	Robie and Hemingway (1995)
ΔH_{12b} = -156.1 ± 2.0	Robie and Hemingway (1995)
ΔH_{13} = -3007.9 ± 1.0	calculated fromWagman et al. (1991)
ΔH_{14} = -285.8 ± 0.1	Robie and Hemingway (1995)
ΔH_{15} = -436.5 ± 0.2	Robie and Hemingway (1995)
$\Delta H_{16} = \Delta_f H°$(adamite) = $\Delta H_{1a} + 2\Delta H_{2a} + \Delta H_3 - 10.96\Delta H_4 - \Delta H_5 - \Delta H_6 + \Delta H_{11a} + 2\Delta H_{12a} + \Delta H_{13} - 10.96\Delta H_{14} - \Delta H_{15}$	
$\Delta H_{17} = \Delta_f H°$(zincolivenite) = $\Delta H_{1a} + \Delta H_{2a} + \Delta H_{2b} + \Delta H_3 - 10.96\Delta H_4 - \Delta H_5 - \Delta H_8 + \Delta H_{11a} + \Delta H_{12a} + \Delta H_{12b} + \Delta H_{13} - 10.96\Delta H_{14} - \Delta H_{15}$	
$\Delta H_{18} = \Delta_f H°$(olivenite) = $\Delta H_{1a} + 2\Delta H_{2b} + \Delta H_3 - 10.96\Delta H_4 - \Delta H_5 - \Delta H_8 + \Delta H_{11a} + 2\Delta H_{12b} + \Delta H_{13} - 10.96\Delta H_{14} - \Delta H_{15}$	
$\Delta H_{19x} = \Delta_f H°$(solid solution oliv-lib) = $(1-x)\Delta H_{1a} + x\Delta H_{1b} + 2\Delta H_{2b} + \Delta H_3 - 10.96\Delta H_4 - \Delta H_5 - \Delta H_{9x} + (1-x)\Delta H_{11a} + x\Delta H_{11b} + 2\Delta H_{12b} + \Delta H_{13} - 10.96\Delta H_{14} - \Delta H_{15}$	
$\Delta H_{20} = \Delta_f H°$(libethenite) = $\Delta H_{1b} + 2\Delta H_{2b} + \Delta H_3 - 10.96\Delta H_4 - \Delta H_5 - \Delta H_{10} + \Delta H_{11b} + 2\Delta H_{12b} + \Delta H_{13} - 10.96\Delta H_{14} - \Delta H_{15}$	

Table 3-6. Thermodynamic properties of the end members adamite, zincolivenite, olivenite and libethenite.

	$\Delta_f H^o$	S^o	$\Delta_f S^o$	$\Delta_f G^o$	log K_{sp}
2σ	± 3.2	± 0.5	± 1.0	± 3.4	
adamite	–1401.7	160.1	–537.1	–1247.6	–10.90 ± 0.62[a]
zincolivenite	–1211.6	159.5	–529.6	–1053.7	–13.33 ± 0.62[b]
olivenite	–997.3	158.9	–521.3	–841.9	–15.30 ± 0.65[c]
libethenite	–1384.4	163.4	–522.2	–1228.7	–16.86 ± 0.65[d]

The formation reactions are defined in Table 3-6, reactions 16-20. All enthalpy and Gibbs free energy values are in kJ·mol^{-1}, all entropy values are in J·mol^{-1}·K^{-1}. Entropies of formation calculated from the listed entropy values and the entropies of elements in their standard state are from Robie and Hemingway (1995).
[a-d] Solubility products were calculated with these auxiliary data (all in kJ·mol^{-1}): $\Delta_f G^o(Cu^{2+},aq)$ = +65.1±0.1, $\Delta_f G^o(Zn^{2+},aq)$ = –147.3±0.2 (Robie and Hemingway, 1995), $\Delta_f G^o(AsO_4^{3-},aq)$ = –647.6±1.5 (Nordstrom et al., 2014), $\Delta_f G^o(PO_4^{3-},aq)$ = –1025.5±1.6 (Grenthe et al., 1992), $\Delta_f G^o(H_2O,l)$ = –237.14±0.04 (Robie and Hemingway, 1995).
These equilibrium constants refer to the reactions:
[a]$Zn_2(AsO_4)(OH) + H^+ = 2Zn^{2+} + AsO_4^{3-} + H_2O$
[b]$CuZn(AsO_4)(OH) + H^+ = Cu^{2+} + Zn^{2+} + AsO_4^{3-} + H_2O$
[c]$Cu_2(AsO_4)(OH) + H^+ = 2Cu^{2+} + AsO_4^{3-} + H_2O$
[d]$Cu_2(PO_4)(OH) + H^+ = 2Cu^{2+} + PO_4^{3-} + H_2O$

Gibbs free energy of formation and solubility products

Combining the entropies and enthalpies of formation, using the relationship of the thermodynamic functions $\Delta_f G° = \Delta_f H° - T\Delta_f S°$, results in the respective Gibbs free energies of formation for libethenite, olivenite, zincolivenite and adamite (Table 3-6, Table 3-7). These tables also include solubility products from these values. Solubility products had previously been reported for adamite, olivenite and libethenite (Magalhães et al., 1986; Magalhães et al., 1988; Majzlan et al., 2015). The data from the above mentioned researchers agree well with our results (Table 3-7). We are not aware of any thermodynamic data published for zincolivenite.

Table 3-7. Gibbs free energy of formation and solubility products of the end members adamite, zincolivenite, olivenite and libethenite from this work and other researchers.

	adamite	**olivenite**	**libethenite**
$\Delta_f G^o$	–1247.6 ± 3.4	–841.9 ± 3.4	–1228.7 ± 3.4
Magalhães et al. (1986, 1988)	–1252.9 ± 1.9	–846.4 ± 1.6	–1228.8 ± 3.0
Majzlan et al. (2015)		–848.7 ± 4.8	–1229.3 ± 4.5
log K_{sp}	–10.90 ± 0.62	–15.30 ± 0.65	–16.86 ± 0.65
Magalhães et al. (1986, 1988) [a]	–12.88	–16.18	–16.88
Majzlan et al. (2015)		–16.50 ± 0.88	–16.94 ± 0.82

[a] calculated from data in Magalhães et al. (1986, 1988)

3.5.4 Thermodynamic properties of the olivenite–libethenite solid solution

The nonideal character of a solid solution can be evaluated in terms of excess thermodynamic parameters, such as the excess free energy of mixing (ΔG^{EX}), the excess enthalpy of mixing (ΔH^{EX}), the excess molar volume (ΔV^{EX}) and the excess entropy of mixing (ΔS^{EX}). These excess parameters are defined by the difference between the thermodynamic mixing parameters (ΔG^{MIX}, ΔH^{MIX}, ΔV^{MIX}, ΔS^{MIX}) of the actual solid solution and the corresponding parameters of an equivalent ideal solid solution (G^{MIX}_{ideal}, $H^{MIX}_{ideal}=0$, $V^{MIX}_{ideal}=0$, S^{MIX}_{ideal}). For the following sections, X_{lib} and X_{oli} will represent the real moles of libethenite and olivenite, respectively, measured by the ICP-OES (Table 3-3).

Excess Volume of Mixing

The excess volume of mixing of the solid solution members can be determined from the unit cell parameters using this expression

$$\Delta V^{EX} = \Delta V^{MIX} = V_{real} - V_{ideal} = V_{SS} - [X_{lib}V_{lib} + X_{oli}V_{oli}] \quad (1)$$

where V_{SS} is the molar volume of a solid solution (SS) of X_{lib} moles of libethenite and X_{oli} moles of olivenite, and V_{lib}, V_{oli} are the molar volumes of end member libethenite and olivenite, respectively. V_{ideal} corresponds to the molar volume of a mechanical mixture of the two end members with the same composition. V_{lib} and V_{oli} were calculated during Rietveld refinement with JANA2006 (Petříček et al., 2014) and are shown in Table 3-4. Figure 3-6 shows the variation of ΔV^{EX} with composition. The negative values for the excess volume of mixing of the arsenic rich solid solution members indicate stronger interactions of mixed molecules than individual

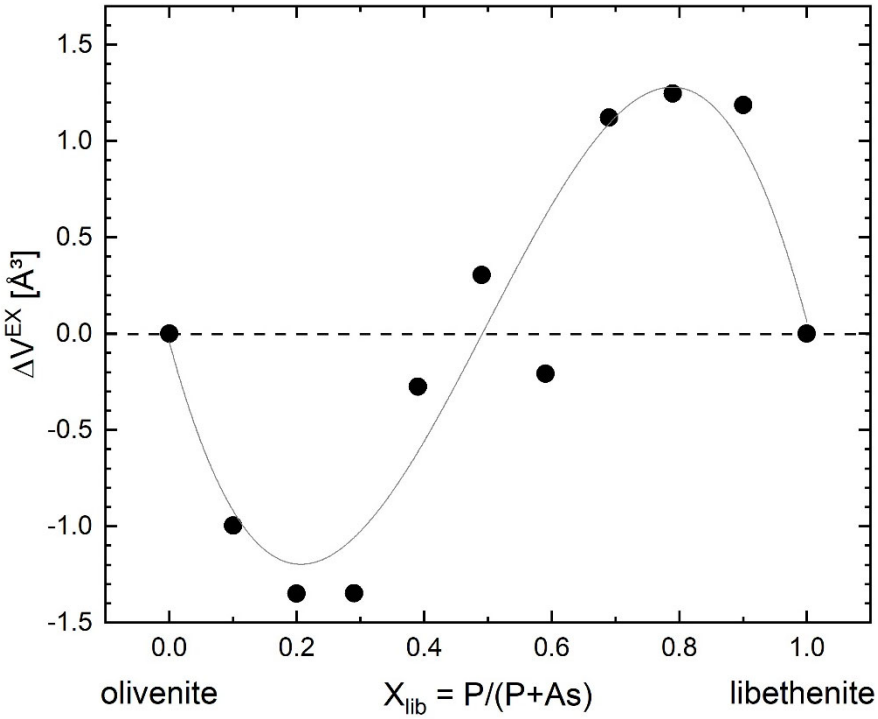

Figure 3-6. Excess volume of solid solution olivenite [$Cu_2(AsO_4)(OH)$] – libethenite [$Cu_2(PO_4)(OH)$]. The dashed line indicates ideal mixing.

molecules before mixing and therefore a smaller volume of the structure whereas the positive values of the phosphate rich solid solution members indicate a volume expansion on mixing and thus weaker interactions than the interactions of pure solvents. Due to the opposing values of ΔV^{EX} for the arsenic rich solid solution members and the phosphatian rich solid solution members, we should take into consideration that there could be two solid solutions, between olivenite and $X_{lib} = 0.5$ and $X_{lib} = 0.5$ and libethenite.

Enthalpies of mixing

The enthalpy of mixing or the heat of mixing of the components is the difference between the enthalpies of the components in solution and the enthalpies of the pure components before mixing. Thus for a solid solution composition with a certain X_{lib} and X_{oli} ($X_{oli} = 1 - X_{lib}$)

$$\Delta H^{EX} = \Delta H^{MIX} = H_{ideal} - H_{real} = [X_{lib}H_{lib}^{diss} + X_{oli}H_{oli}^{diss}] - \Delta H_{SS}^{diss} \quad (2)$$

where ΔH_{SS}^{diss} stands for the measured enthalpy of dissolution of a solid solution (SS) with composition X_{lib}. The derived enthalpies of mixing are shown in Figure 3-7 and Table 3-8. Although the relative error in ΔH_{SS}^{diss} is small, the result (ΔH^{EX}) of the subtraction (Eq. 2) is a smaller number with a larger relative error. This level of uncertainty is typical for calorimetric determination of excess parameters.

The positive enthalpies of mixing measured for the intermediate members of the olivenite–libethenite solid solution reflects the size mismatch of As^{5+} an P^{5+} in the structure and an

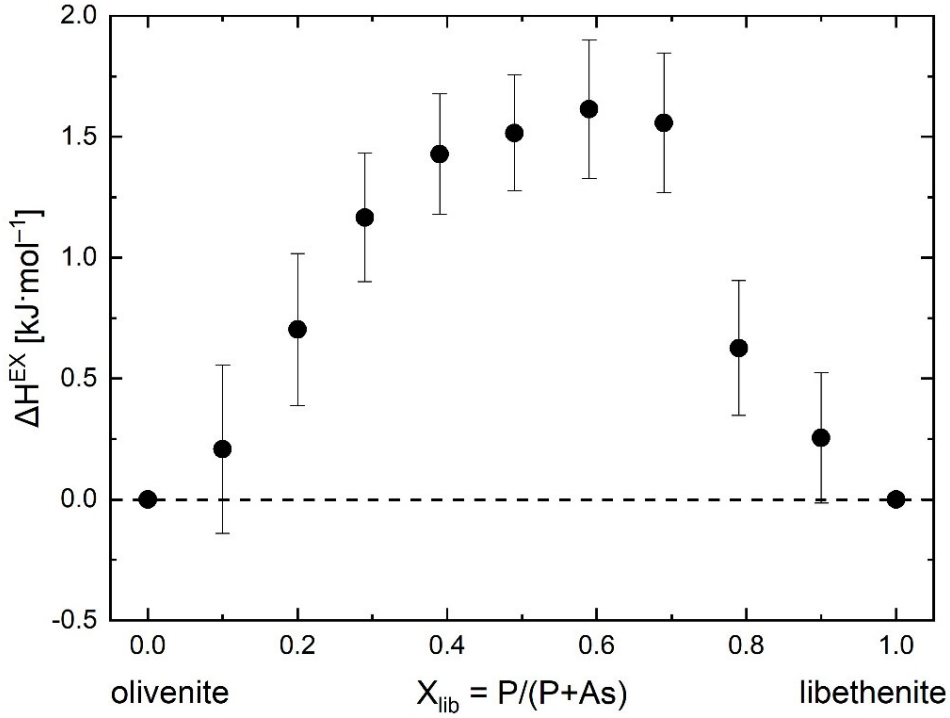

Figure 3-7. Excess enthalpy of solid solution olivenite [$Cu_2(AsO_4)(OH)$] – libethenite [$Cu_2(PO_4)(OH)$]. The dashed line indicates ideal mixing.

Table 3-8. Enthalpies of dissolution and thermodynamic properties of mixing of the solid solution olivenite [$Cu_2(AsO_4)(OH)$] – libethenite [$Cu_2(PO_4)(OH)$]

	ΔH^{diss}	$\Delta_f H^o$	ΔH^{EX}	S^{MIX}_{ideal}	ΔG^{MIX}	ΔV^{EX}
olivenite	–25.202 ± 0.311	–997.3	0	0	0	0 ± 0.01
10P90As	–25.906 ± 0.184	–1035.8	0.208 ± 0.348	2.703	–0.597 ± 0.348	–1.00 ± 0.02
20P80As	–26.897 ± 0.145	–1074.0	0.703 ± 0.315	4.161	–0.538 ± 0.315	–1.35 ± 0.01
30P70As	–27.806 ± 0.006	–1108.4	1.166 ± 0.266	5.007	–0.327 ± 0.266	–1.35 ± 0.02
40P60As	–28.565 ± 0.019	–1146.8	1.428 ± 0.250	5.560	–0.229 ± 0.250	–0.28 ± 0.01
50P50As	–29.148 ± 0.055	–1185.5	1.515 ± 0.239	5.761	–0.202 ± 0.239	0.30 ± 0.02
60P40As	–29.742 ± 0.188	–1224.1	1.614 ± 0.287	5.628	–0.064 ± 0.287	–0.21 ± 0.02
70P30As	–30.181 ± 0.208	–1262.8	1.557 ± 0.288	5.147	0.022 ± 0.288	1.12 ± 0.01
80P20As	–29.747 ± 0.211	–1302.5	0.626 ± 0.279	4.273	–0.648 ± 0.279	1.25 ± 0.02
90P10As	–29.920 ± 0.215	–1345.4	0.254 ± 0.269	2.703	–0.551 ± 0.269	1.19 ± 0.02
libethenite	–30.162 ± 0.143	–1384.4	0	0	0	0 ± 0.02

endothermic process. Additionally, the step between the values for X_{lib} = 0.69 and 0.79 (Figure 3-7) could be an indication for the change of the symmetry, from monoclinic (olivenite) to orthorhombic (libethenite). The maximum ΔH^{EX} is at X_{lib} = 0.6 which shows an asymmetric trend for the mixing enthalpies (Figure 3-7). This means that it is energetically less costly to substitute P^{5+} atoms into olivenite than vice versa. This probably occurs because substituting a smaller cation (P^{5+}) into a larger site may be easier than incorporating a larger cation (As^{5+}) into a site normally occupied by a smaller one. A similar asymmetry was shown by Majzlan et al. (2015) where they assume a preferred incorporation of the "libethenite molecule" into the solid solution, due to the lower solubility product of libethenite compared to that of olivenite (Table 3-6).

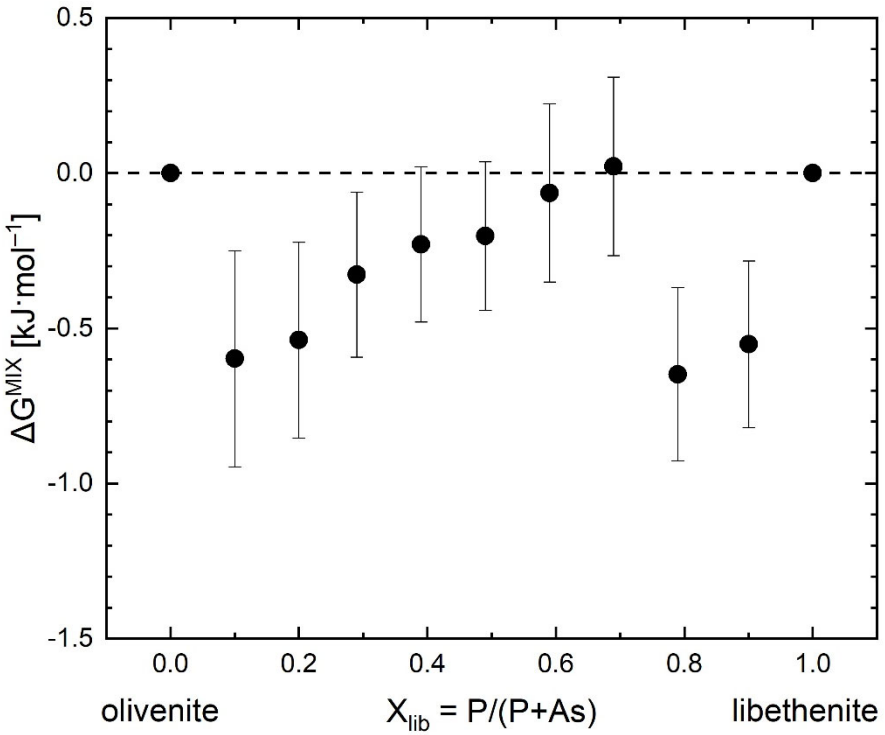

Figure 3-8. Gibbs free energy of mixing of solid solution olivenite [$Cu_2(AsO_4)(OH)$] – libethenite [$Cu_2(PO_4)(OH)$]. The dashed line indicates ideal mixing.

Gibbs free energy of mixing

We need to calculate the Gibbs free energy of mixing in order to detect a possible miscibility gap of the solid solution. The Gibbs free energy of mixing may be calculated assuming a subregular solution model and an ideal entropy of mixing. The ideal entropy of mixing of As^{5+} and P^{5+} at one cation site in the structure is

$$\Delta S^{mix}_{ideal} = -R[X_{lib} \ln X_{lib} + X_{oli} \ln X_{oli}] \quad (3)$$

with R = 8.314462 $J \cdot mol^{-1} \cdot K^{-1}$ (Table 3-8). Then the Gibbs free energy of mixing is

$$\Delta G^{mix} = \Delta H^{mix} - T\Delta S^{mix}. \quad (4)$$

A graphical representation of the Gibbs free energy of mixing is shown in Figure 3-8. Generally, negative values of the Gibbs free energy of mixing show that all synthesized samples of the olivenite–libethenite solid solution series are stable phases under atmospheric conditions. But in our case, the values of the Gibbs free energy of mixing do not seem to be realistic, so that the assumption of an ideal entropy of mixing is wrong. The non-ideal entropy of the solid solution members is not known so far but could be substantial for the elaborate analysis of those.

Data for olivenite-libethenite solid solution from natural samples show a gap between the compositions X_{lib} = 0.12 and 0.42 (Szakáll et al., 1994; Jansa et al., 1998; Gołębiowska et al., 2006; Sejkora et al., 2006; Williams et al., 2006; Sejkora et al., 2008; Lafuente et al., 2015; Majzlan et al., 2015). An explanation is most probably that no natural samples of this composition were found or analysed so far.

3.6 Conclusion

The enthalpies of dissolution of several members of the libethenite group $M_2(XO_4)(OH)$ (M = Cu, Zn; X = P, As), including the olivenite-libethenite solid solution series, were measured at 25 °C and the enthalpy of mixing was determined to be positive for the whole series. The synthesized phases were all characterized by pXRD, FT-IR and ICP-OES and confirmed to be compositionally homogeneous. Rietveld analysis suggests an evolution of the unit cell parameters following the size of the ionic radii. The IR-spectra show the evolution of the bands corresponding to the PO_4 and AsO_4 tetrahedron. Furthermore, the crystallographic analysis shows a negative excess volume of mixing for arsenic-rich solid solution members and a positive excess volume of mixing for phosphoric-rich phases which could be an indication that two solid solutions exist. Additionally, this would be complicated by the symmetry change from monoclinic (olivenite) to orthorhombic (libethenite) between X_{lib} = 0.69 and 0.79 which is shown by the calculated ΔH^{MIX} values. This asymmetry of the excess enthalpy of mixing shows the easier incorporation of a smaller cation (P^{5+}) into a larger site (As^{5+}) than vice versa. Taken all together, we have shown that a complete olivenite–libethenite solid solution exists without miscibility gap (Figure 3-9).

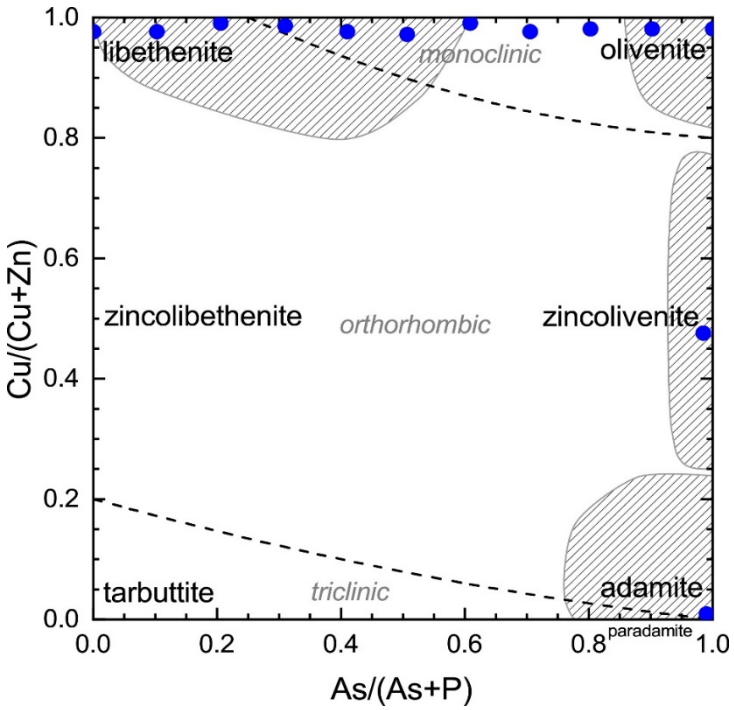

Figure 3-9. Compositional variability of the members of the composition $M_2(XO_4)(OH)$ (M = Cu, Zn; X = P, As). Our data are shown as blue points and data from literature as shaded areas. Literature data from: Southwood et al. (2020), Majzlan et al. (2015), Braithwaite et al. (2009), Sejkora et al. (2008), Williams et al. (2006), Sejkora et al. (2006), Gołębiowska et al. (2006), Szakáll et al. (1994). Modified after Andersen and Moulding (2009).

3.7 Special explanatory notes

Due to the unrealistic ΔG^{MIX} with the assumption of an ideal entropy of mixing, it is highly recommended to measure the heat capacity of all solid solution members. Therefore, we will get the non-ideal entropy of mixing and a better insight into the thermodynamic properties of the solid solution between olivenite and libethenite.

3.8 Acknowledgements

The work presented here was financially supported by a grant of the *Deutsche Forschungsgemeinschaft* MA 3927/26-1.

4 Fractionation of copper, oxygen and hydrogen isotopes between malachite and aqueous phase

Alexandra M. Plumhoff[1]*, Ryan Mathur[2], Rastislav Milovský[3], Juraj Majzlan[1]

[1]Institute of Geosciences, Friedrich-Schiller University, Burgweg 11, 07749 Jena, Germany
[2]Department of Geology, Juniata College, 1700 Moore St, Huntingdon, PA, 16652, USA
[3]Earth Science Institute, Slovak Academy of Sciences, Dumbierska 1, SK-974 11, Banská Bystrica, Slovakia

Submitted to Geochimica et Cosmochimica Acta, 18th May 2020

The involved co-authors and their contribution to the respective manuscript are listed:

The conceptual design of the experiments evolved in discussion with Juraj Majzlan. I was responsible for the preparation, the conduction of the experiments and the data evaluation. The Cu isotope measurements were done by Ryan Mathur. Rastislav Milovský collected and processed the H and O isotope measurements. The preparation of the manuscript was in my responsibility in close collaboration with all co-authors.

4.1 Abstract

Studies of the equilibrium isotope properties of stable isotopes of minerals have been initiated principally because of their application to the solution of geochemical problems. Therefore, we examined malachite, a common secondary mineral in the oxidation zone of ore deposits. Stable isotope characterization can contribute needed information on the formation of malachite by establishing the isotopic composition of the parental waters. The equilibrium oxygen and hydrogen isotope fractionations between malachite and solution were determined by precipitation experiments over the temperature range from 10 to 65 °C and could be distinguished in two sets of fractionation factors depending on the temperature: For 45-65 °C is $1000 \ln \alpha_{\mathrm{mal-sol}}^{\mathrm{oxygen}} = 2.87\ (10^6/\mathrm{T}^2) + 0.96$ and $1000 \ln \alpha_{\mathrm{mal-sol}}^{\mathrm{hydrogen}} = -1.47\ (10^6/\mathrm{T}^2) - 22.29$ with temperature (T) in Kelvin. With the application of the fractionation factors of oxygen and hydrogen of malachite onto source water from the meteoric water line, we were able to calculate the "malachite line" which represents the isotopic compositions of malachite that would precipitate from such water.

We also examined the copper isotope fractionation factors between solution and malachite from 10 to 65 °C: $1000 \ln \alpha_{\mathrm{sol-mal}}^{\mathrm{copper}} = 0.03\ (10^6/\mathrm{T}^2) - 0.19$ with fractionation shift of $\Delta^{65}\mathrm{Cu}_{\mathrm{malachite\text{-}solution}} = -0.16 \pm 0.05$ ‰. This fractionation shift implies that chemical reactions for oxide minerals without change of the redox state yield only minor copper isotope fractionation.

The calculated fractionation factors of oxygen and hydrogen were used to determine the oxygen and hydrogen isotopic composition of the parental waters of natural malachite samples from a number of localities worldwide. With $\delta^{18}\mathrm{O}_{\mathrm{VSMOW}}$ values of +22 to +29.5 ‰ and δD values of –132 to –61 ‰ for the natural malachite and $\delta^{18}\mathrm{O}_{\mathrm{VSMOW}}$ values of –14.5 to –7 ‰ and δD values of –107 to –36 ‰ for the parental water together with the Cu isotopes, it is to assume that all investigated malachite samples are supergene samples which formed from meteoric water. Even in massive malachite samples from Ural Mts. (Russia), no signs of other fluids were detected from the isotopic composition.

4.2 Introduction

Stable isotope techniques are an important tool in almost every branch of the Earth sciences. Central to many of these applications is a quantitative understanding of equilibrium isotope partitioning between substances. Therefore, knowledge about the equilibrium fractionation factors and isotopic disequilibrium could provide information on the processes during water-rock interactions. The isotopic exchange between a mineral and a solution can be achieved either by chemical reaction (dissolution-precipitation) or diffusion. To get good results and a reliable fractionation factor, it is important to have equilibrium fractionation which is temperature dependent and not kinetic fractionation of isotopes which is unidirectional, fast or incomplete. At equilibrium, isotopic shifts between minerals and fluids are a function of the origin of water and water/rock ratios (Taylor, 1977; Criss et al., 1987). Oxygen and hydrogen isotopes are particularly useful in interpreting water-rock interactions (Gregory and Criss, 1986). For example, the temperature-dependent oxygen isotope fractionations between pairs of cogenetic minerals often provide a very sensitive indicator of the temperature of formation of a mineral (Clayton and Epstein, 1961).

Isotopic exchange experiments have shown that the isotopic fractionation is a function of the classical parameters controlling rates of reactions: solution composition, temperature, pressure, surface area and mineral chemistry (Cole and Chakraborty, 2001). The most important variable influencing the magnitude of fractionation factors is temperature, which influences mainly the light isotopes (H, O). The copper isotopes only show a slight temperature dependence. Pressure effects can be significant for hydrogen isotope fractions but are generally negligible for oxygen isotope fractionation (Chacko et al., 2001).

The attention for Cu isotopes has risen in the last decades for its importance in a variety of natural processes such as ore-forming supergene processes (Larson et al., 2003; Mathur et al., 2005; Mathur and Fantle, 2015; Mathur et al., 2018), including copper isotopes as an indicator of the zone of origin of ore deposits (Mathur and Fantle, 2015), and fluid-rock chemical interaction (Rouxel et al., 2004; Markl et al., 2006; Asael et al., 2012). Such processes can lead to a large variation of the copper isotope composition in natural samples from –17 ‰ to +10 ‰ (e.g., Mathur et al., 2009). Even though there is a large shift of δ^{65}Cu during mineral formation along redox gradients (e.g., Zhu et al., 2002; Mathur et al., 2005; Qi et al., 2019), it is still questioned if the copper isotope fractionation occurs during redox reactions in solution or during the precipitation of the new phase.

Thus, the isotopic composition of malachite can be affected by a number of factors like the isotopic composition of the waters with which malachite may have come in contact during and after its formation, the temperature of the environment at any time during which malachite was subject to isotopic exchange and whether the mineral reached isotopic equilibrium with its environment. Also, it is important what effect the oxidation state of copper has for the copper

isotope fractionation factor. Additionally, there should also exist a relationship between the oxygen and hydrogen isotopic composition of malachite since the isotopic composition of secondary minerals like malachite depend on the isotopic composition of their parental water. And for most meteoric waters, Craig (1961) described the relationship between oxygen and hydrogen isotopes by the equation $\delta D = 8\ \delta^{18}O + 10$, the Global Meteoric Water Line (GMWL). Malachite has been previously successfully synthesized in the laboratory (e.g. Pollard et al., 1991; Tanaka and Yamane, 1992) and the isotope geochemistry of other synthetic carbonates has been investigated by McCrea (1950) and O'Neil et al. (1969). Isotope fractionation factors for malachite are only known for carbon and oxygen so far (Melchiorre et al., 1999). Since malachite is a widely distributed mineral in copper deposits and to analyse the above mentioned points, we investigated the O, H and Cu isotope fractionation associated with the formation of malachite in laboratory under controlled experimental conditions. The isotopic equilibrium of the last element in malachite, carbon, was the focus of the experimental work of Melchiorre et al. (1999) and the measurements on carbon were given only marginal importance of this work. Additionally, natural malachite samples were analysed and application of this experimental work to the data of natural malachite provided quantitative evidence for the conditions of malachite formation.

4.3 Materials

Malachite was synthesized by a modified wet chemical procedure after Tanaka and Yamane (1992). Stock solutions, four liters each, of 0.1 M $Cu(NO_3)_2$ and of 0.15 M Na_2CO_3 were prepared at the beginning of the experiments. For each single synthesis, 100 mL of 0.1 M $Cu(NO_3)_2$ and 100 mL of 0.15 M Na_2CO_3 were filled into two separate borosilicate glass bottles and were heated separately in a water bath with thermostat to the desired temperature (Table 4-1). After temperature stabilization (~24 hours), both solutions were rapidly mixed, closed tightly in one bottle and left in the water bath for another 24-120 hours depending on the temperature. The final product was filtered and washed with deionized water and dried at room temperature.

Table 4-1. Overview of the syntheses with sample names, duration of the syntheses, temperature set and the average of the measured temperature.

sample	duration [h]	T_{set} [°C]	$T_{average}$ [°C]
Mal_N_10	120	10	9.65 ± 0.15
Mal_N_15	120	15	14.05 ± 0.15
Mal_N_20	120	20	18.95 ± 0.25
Mal_N_25	72	25	24.50 ± 0.30
Mal_N_30	24	30	29.30 ± 0.10
Mal_N_35	24	35	34.50 ± 0.10
Mal_N_40	24	40	39.45 ± 0.15
Mal_N_45	24	45	44.45 ± 0.15
Mal_N_50	24	50	49.00 ± 0.30
Mal_N_55	24	55	54.35 ± 0.05
Mal_N_60	24	60	59.30 ± 0.20
Mal_N_65	24	65	64.25 ± 0.25

4.3.1 Natural malachite samples

Malachite is a typical mineral in the oxidation zone of copper deposits which forms during the weathering of primary copper minerals, mainly chalcopyrite. Natural malachite is a very common mineral but occurs rarely in larger quantities. It forms typically as crusts or crystalline aggregates, often banded like agates and also as botryoidal clusters of radiating crystals. There are only a few known deposits of big masses of malachite (up to 50 t) in the Ural Mountains (e.g. Nizhny Tagil, Gumeshevskoe). The natural malachite samples were from 10 different locations (Table 4-4) which are broadly described in the following section.

The four samples from Russia were all from Variscan scarn deposits in the middle Ural Mountains. The most representative deposits are the Fe-Cu deposit around Nizhny Tagil and the malachite deposit of Gumeshevskoe. In Nizhny Tagil, the Fe-Cu-ores are hosted in Silurian limestone and volcanosedimentary rocks where the ore consists mainly of magnetite with minor hematite, chalcopyrite and pyrite. In Gumeshevskoe, magnetite ores, with disseminated chalcopyrite and pyrite formed in the contact of a quartz-diorite body which intruded into marbles. The most important copper mineral in the oxidation zone of the deposit is malachite but there is also native copper, azurite and chrysocolla (Kolesar and Tvrdý, 2006).

The Cu-Fe ore district of Ľubietová is located in the central part of the Western Carpathians in Slovakia. The ore veins are located in sedimentary Permian quartz and arcosic arenite, quartz porphyre, greywackes, shales, and conglomerates. The primary mineralization includes thin quartz-ankerite veinlets with dispersed chalcopyrite, tennantite and quartz. Gangue minerals are quartz with fewer amounts of carbonates (dolomite-ankerite, siderite, calcite) (Luptáková et al., 2016). The rich assemblage of secondary minerals consists of copper, dominated by phosphates and carbonates, especially pseudomalachite, libethenite and malachite, fine-grained red-coloured iron oxides, manganese oxides, Pb-Fe and Bi-Cu phosphates, Cu-sulfates and Bi-carbonates (Majzlan et al., 2018).

The Cu deposits in Schwatz, Tyrol are located in the Eastern Alps in Austria and hosted by several different rock types, including gneisses and dolomites. The most important primary ores consist of tetrahedrite-tennantite with veins of siderite, calcite and aragonite. Secondary minerals are mainly a wide variety of arsenates, Cu-carbonates malachite and azurite and other minerals (Grundmann and Martinek, 1994; Schnorrer, 1994).

Kamsdorf, Thuringia, is located on the SE border of the Thuringian basin in the middle of Germany. The primary ores of copper, iron and silver-bearing tetrahedrite are mainly hosted by limestones. The main sulfides in the metapelites are chalcopyrite, tetrahedrite, pyrite and marcasite. Secondary minerals are mainly limonite and a wide variety of copper minerals malachite, azurite and brochantite (Decker and Rüger, 1991).

The mine “Eisenzecher Zug” in Siegen, Germany, is located in the north-western parts of the Rhenish Massif. A post Variscan mineralization event formed chalcopyrite-quartz veins with

minor pyrite, sphalerite, tetrahedrite, galena and calcite. Typical secondary minerals are native copper, malachite and brochantite (Golze et al., 2013).

Chessy-les-Mines is a famous French locality near Lyon, France, and is located on the north-eastern border of the Massif Central. The primary mineralization with baryte, galena, sphalerite and chalcopyrite is hosted in altered dacites with a cover of Triassic clays and sandstones. There are secondary minerals of lead, zinc and especially copper (azurite, cuprite, malachite, agardite, chrysocolla).

The Wallaroo mine is located on the north end of the Yorke Peninsula in South Australia and is part of the largest iron oxide-copper-gold province on Earth (Conor et al., 2010). The host rocks of this region are mainly biotite schist partly intruded by porphyries and overlain by limestones and sandstones. The quartz-iron oxide veins have minor chalcopyrite and secondary Cu-mineralization including atacamite, cuprite, malachite and secondary sulfides like chalcocite and covellite (Keeling et al., 2003).

4.4 Methods

Powder X-ray diffraction (pXRD) patterns of all samples were collected with a Bruker D8 Advance DaVinci diffractometer employing CuKα radiation (λ = 1.54058 Å). The patterns were collected at room temperature between 5 and 90 °2θ, with a step size of 0.02 °2θ, and a time per step of 1.0 s.

Fourier-transform infrared (FT-IR) transmission spectra were recorded using a Nicolet iS10 spectrometer. The samples (1-2 mg) were mixed with KBr (FT-IR spectroscopy grade, Merck), gently ground and pressed to pellets. The pellets were measured from 4000 to 400 cm^{-1} with 64 scans per spectrum at a resolution of 4 cm^{-1}. The spectra were baseline-corrected and normalized to maximum intensity.

The thermogravimetric analysis (TGA) was performed on a Setaram TG 92, flushed with argon gas and heated at 10 °C/minute from 25 to 900 °C. Samples ground to fine powder were filled in corundum ceramic cups (25-40 mg) and subjected to the TG analysis.

Light stable isotopes were measured on isotope ratio mass spectrometer (IRMS) MAT253 at Slovak Academy of Sciences, Banská Bystrica, Slovakia. Oxygen and carbon isotopes were measured using an automated carbonate preparation system (KIEL IV) coupled to IRMS in dual-inlet mode. Powdered samples of ca. 100 μg were heated overnight at 70 °C in order to remove adsorbed water. The samples were then reacted with anhydrous H_3PO_4 at 70 °C in vacuum. The CO_2 yield was purified through two liquid nitrogen traps and introduced into the IRMS. Raw isotope values were calibrated using international reference material NBS18 with $\delta^{13}C = 5.014‰$, $\delta^{18}O = –23.2‰$ and two working standards with $\delta^{13}C = +2.48‰$, $\delta^{18}O = –2.40‰$ and $\delta^{13}C = –9.30‰$, $\delta^{18}O = –15.30‰$, respectively. Usual precision of the method is 0.02 ‰ for $\delta^{18}O$ and 0.01 ‰ for $\delta^{13}C$. The measured values are reported as $\delta^{13}C_{VPDB}$ and $\delta^{18}O_{VSMOW}$.

Hydrogen isotopes were measured using an elemental analyser (FLASH 2000 HT plus) coupled to the IRMS in continuous-flow mode. Powdered samples of ca. 250 - 700 µg were filled into silver capsules and pyrolysed on glassy-carbon chips in a stream of helium at 1400 °C. Evolved H_2 was purified from other gases on packed chromatographic column (5Å mol sieve) and led into IRMS. The δD values were calibrated by international reference materials USGS 57 and USGS 58 with δD = –91.00 and –28.00 ‰, respectively. The usual precision of the method is 3 ‰ for δD, values are reported in permil vs.d VSMOW.

For the determination of isotopic composition of copper, ~50 mg of malachite was placed into 15 ml Teflon beaker with 4 ml of ultrapure aquaregia. The solution was heated to 100 °C for 12 hours and complete dissolution was visually confirmed. The solutions were dried and then diluted to 100 ppb Cu isotope analysis. Since the synthetic phases were pure copper carbonates, no ion exchange chromatography was needed for the analyses (Mathur et al., 2005; Mathur et al., 2009; Zhu et al., 2000). The solutions were measured on the multicollector inductively coupled plasma mass spectrometer (MC-ICP-MS, Neptune) at Pennsylvania State University (State College, Pennsylvania, USA). On peak backgrounds were subtracted for each measurement. The total procedural copper blank is <0.8 nanograms. Mass bias was corrected by standard-sample bracketing with the NIST 976 international copper standard. Each measurement consisted of 30 $^{65}Cu/^{63}Cu$ ratios. Values are reported in the traditional per mil format in comparison to the NIST 976 standard. To assess error, the variation of the standard throughout the measurement session was monitored. The NIST 976 standard varied 0.06 ‰, 2σ, n=18. Samples were measured in duplicate during the session and all reported values fall within the reported error.

4.5 Results

All of the final synthesized samples consist of a single phase $Cu_2CO_3(OH)_2$, corresponding to the mineral malachite. The refined lattice parameters compare well to those reported for malachite previously (Table 4-2). The FT-IR spectrum (Fig. 4-1) is comparable to the malachite standard in Chukanov (2014). Some of the weak bands reported by Chukanov (2014) are not seen in our spectra but the strong bands are present.

The TG analysis (Fig. 4-2) shows mass loss in several steps. Around 110 °C, all H_2O is released and at 300 °C all CO_2 is lost. At ~350 °C, the samples completely decomposed to CuO. The

Table 4-2. Unit-cell parameters for synthetic malachite in comparison with specimen from Schwarzenberg, Saxony, Germany (Süsse, 1967).

	synthetic, this work	**natural, Schwarzenberg**
a (Å)	9.544(1)	9.502
b (Å)	11.929(1)	11.974
c (Å)	3.255(1)	3.240
β (°)	99.01(1)	98.75
V (Å³)	366.0	364.35
SG	*$P2_1/a$*	*$P2_1/a$*

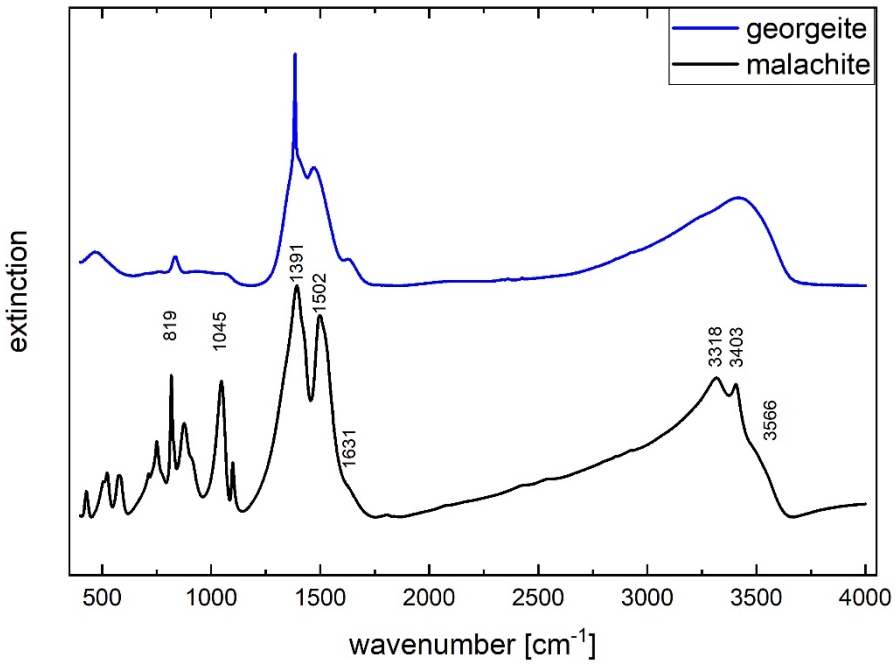

Figure 4-1. FT-IR spectra of malachite and georgeite, both $Cu_2CO_3(OH)_2$. Bands are marked with their positions in cm^{-1}.

measured mass loss is 26.6 ± 0.1 wt.%, lower than the nominal $H_2O + CO_2$ content of 28.1 wt.%. The results of the TG analyses are comparable with the result shown by Seguin (1975).

4.5.1 Transient phase during the synthesis of our samples

Upon rapid mixing of the two starting solutions, the solution effervesces and forms a light blue precipitate. This precipitate transforms completely into a green phase (malachite) after one to several hours (at 65 °C to 10 °C, respectively). Since the nature of this light blue transient phase

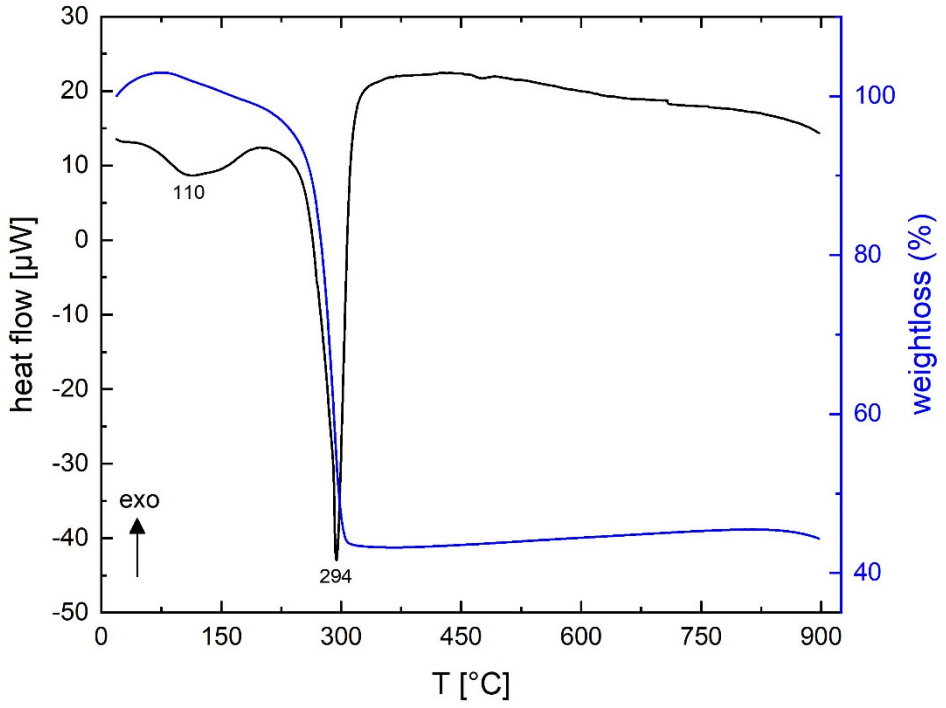

Figure 4-2. Thermogravimetric analysis of malachite. The extrema in the heat flow are labelled with corresponding temperature (in °C).

appears to be important for the understanding of the results, a separate set of experiments was conducted.

The starting solutions of 0.1 M $Cu(NO_3)_2$ and 0.15 M Na_2CO_3 were placed in an oven to equilibrate at the desired temperatures (25, 50, 60, 70, 80 and 90 °C). After temperature stabilization (~2 hours), both solutions, 2.5 ml of each, were mixed directly in a syringe (internal volume 6 mL) which was closed and shaken. A polyethersulfone filter cap (0.45 µm pore size) was screwed onto the syringe after ~30 s and the suspension was quickly pressed through the filter. The cap was cut open and the filter with the light blue precipitate was then placed in a freezer (-20 °C) and left there for ~60 min. Afterwards, the filter was put in a vacuum chamber to freeze dry the blue precipitate for ~2 hours. Attempts to carry out the filtration and drying at room temperature failed because the light blue precipitate turned always green and changed to malachite. PXRD showed that the light blue precipitate is X-ray amorphous. The FT-IR spectrum of the precipitate and the wavenumbers of the bands are displayed in Fig. 4-1. This spectrum is directly comparable to the ones for georgeite [$Cu_2CO_3(OH)_2$] shown in Chukanov (2014) and Pollard et al. (1991). These experiments show that georgeite forms at all temperatures between 25 to 90 °C as an initial, transient phase and transforms at different rates as a function of temperature to malachite.

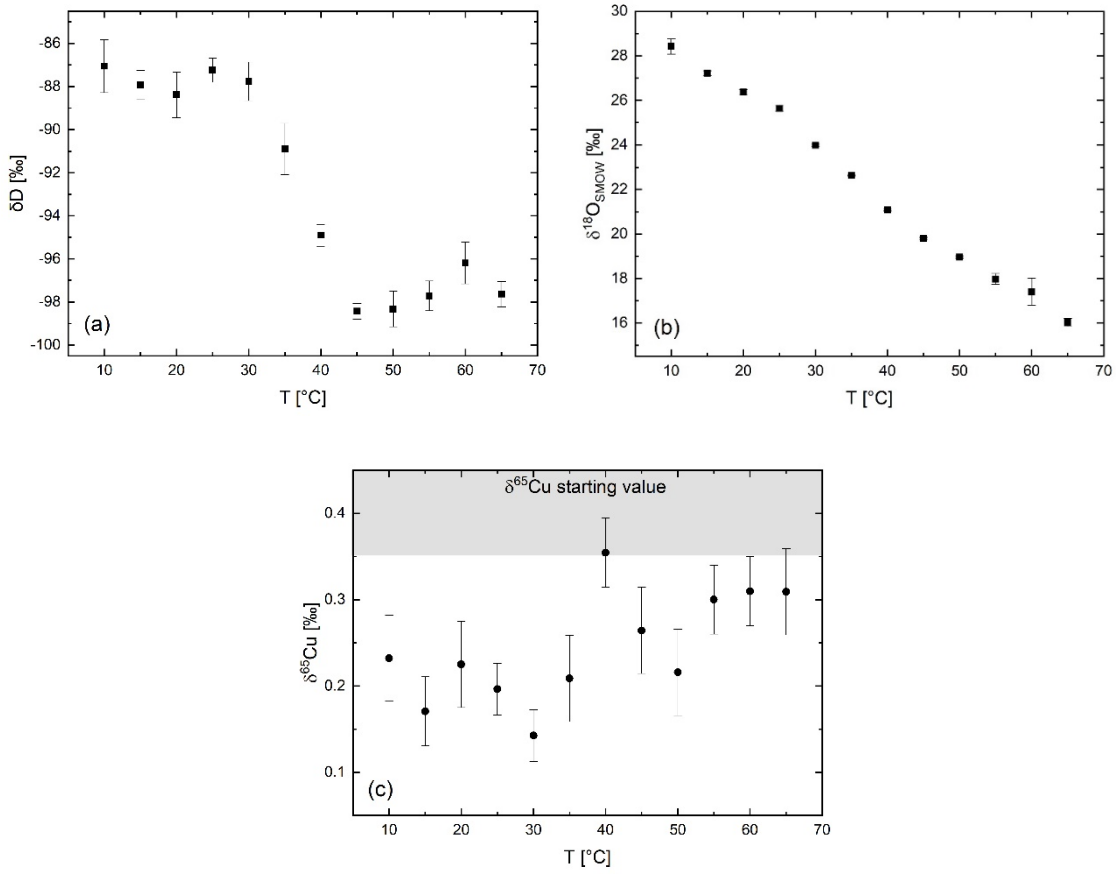

Figure 4-3. Isotopic values of a) deuterium (–62.04 ± 1.85 ‰) b) oxygen (–9.11 ± 0.63 ‰) and c) copper (0.4 ± 0.05‰) of the synthesized malachite samples. (Values of starting solution in brackets)

4.5.2 Isotopes

For the isotopic systems investigated in this paper, the data show a distinct pattern, most easily seen for δD (Fig. 4-3a) but detectable also for $\delta^{18}O$ (Fig. 4-3b). There are two sets of values that can be fit separately to linear functions in a $(10^6/T^2)$-1000 ln α space (e.g. Fig. 4-4). The first set are the values for the syntheses at 10-30 °C, the second set the values at 45-65 °C. At temperatures between the two sets, the isotopic values change rapidly and were not included in fitting. The isotopic fractionation factors can be described by equations of the form $1000 \ln \alpha = A\,(10^6/T^2) + B$ (eq. 1), where A and B are constants and T the temperature in Kelvin (e.g. O'Neil et al., 1969).

Oxygen isotope fractionation between malachite and the starting aqueous solution is shown in Fig. 4-4, together with two separate linear functions between 10 and 65 °C. Oxygen fractionation factors for malachite-solution ($\alpha_{mal\text{-}sol}$) were calculated from the $\delta^{18}O$ values of the malachite product ($\delta^{18}O_{mal}$) and the starting solution ($\delta^{18}O_{sol}$), using the well-known definition of α as a function of δ-values (Criss, 1999): $\alpha_{mal\text{-}sol} = (\delta^{18}O_{mal} + 1000 / \delta^{18}O_{sol} + 1000)$.

The isotopic composition of the final solution was not measured in this study, but Melchiorre et al. (1999) showed that the $\delta^{18}O$ values for the initial and final solution are practically identical. We define the fractionation factor for mineral-solution oxygen fractionation with two best-fit regressions combined as functions of temperature (e.g. Fig. 4-4). The equation for the fit from 10-35 °C is $1000 \ln \alpha^{oxygen}_{gg-sol} = 2.71\,(10^6/T^2) + 4.06$ and for 45-65 °C is $1000 \ln \alpha^{oxygen}_{mal-sol} = 2.87\,(10^6/T^2) + 0.96$ (Table 4-3).

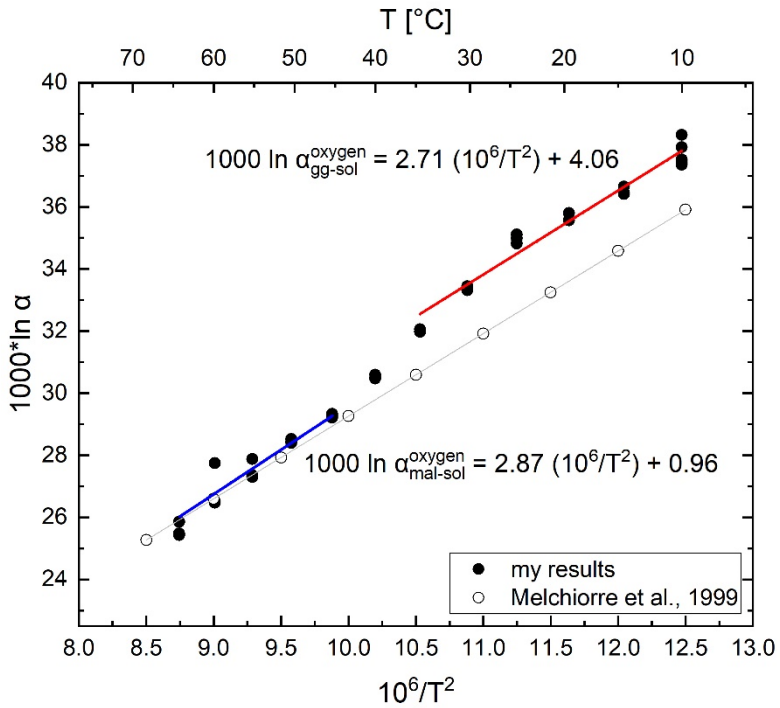

Figure 4-4. Mineral-solution oxygen isotope fractionation as a function of temperature for this study's results and for comparison, Melchiorre et al. (1999) experiment.

Table 4-3. Values for A and B of the equation for the isotopic fractionation factors of oxygen and hydrogen in the form of 1000 ln α = A (10^6 / T^2) + B, with T the temperature in Kelvin.

	temperature range	A	B
$oxygen_{georgeite\text{-}solution}$	10 – 35 °C	2.70511 ± 0.15634	4.06364 ± 1.78532
$oxygen_{malachite\text{-}solution}$	45 – 65 °C	2.86565 ± 0.32774	0.95654 ± 3.05483
$hydrogen_{georgeite\text{-}solution}$	10 – 35 °C	0.21408 ± 0.47287	–27.47327 ± 5.51852
$hydrogen_{malachite\text{-}solution}$	45 – 65 °C	–1.47184 ± 0.60706	–22.29443 ± 5.65062
$copper_{solution\text{-}malachite}$	10 – 65 °C	0.03256 ± 0.01294	–0.18548 ± 0.13613

Hydrogen isotope fractionation between malachite and aqueous solution is also represented by two linear functions in a $(10^6/T^2)$-$1000 \ln \alpha$ space (Fig. 4-5). The equations for the fits are $1000 \ln \alpha_{gg-sol}^{hydrogen} = 0.21\ (10^6/T^2) - 27.47$ for 10-30 °C experiments and $1000 \ln \alpha_{mal-sol}^{hydrogen} = -1.47\ (10^6/T^2) - 22.29$ for the 45-65 °C experiments (Table 4-3).

The copper isotope fractionation between malachite and the aqueous solution is represented by one straight line in the $(10^6/T^2)$-$1000 \ln \alpha$ space in Fig. 4-6. The equation for the line from 10-65 °C is $1000 \ln \alpha_{sol-mal}^{copper} = 0.03\ (10^6/T^2) - 0.19$ (Table 4-3). The only comparable datum so far is from Maréchal and Sheppard (2002) who describe a fractionation factor for solution ($Cu(NO_3)_2$)-malachite of 1.00020 and 1.00017 at 30 °C and 50 °C, respectively. With our fractionation factor $\alpha_{sol-mal}^{copper}$, matching values can be retrieved, 1.00026 and 1.00018 for 30 °C and 50 °C, respectively. Our results and those of Maréchal and Sheppard (2002) agree in that malachite is depleted in ^{65}Cu relative to the starting solution.

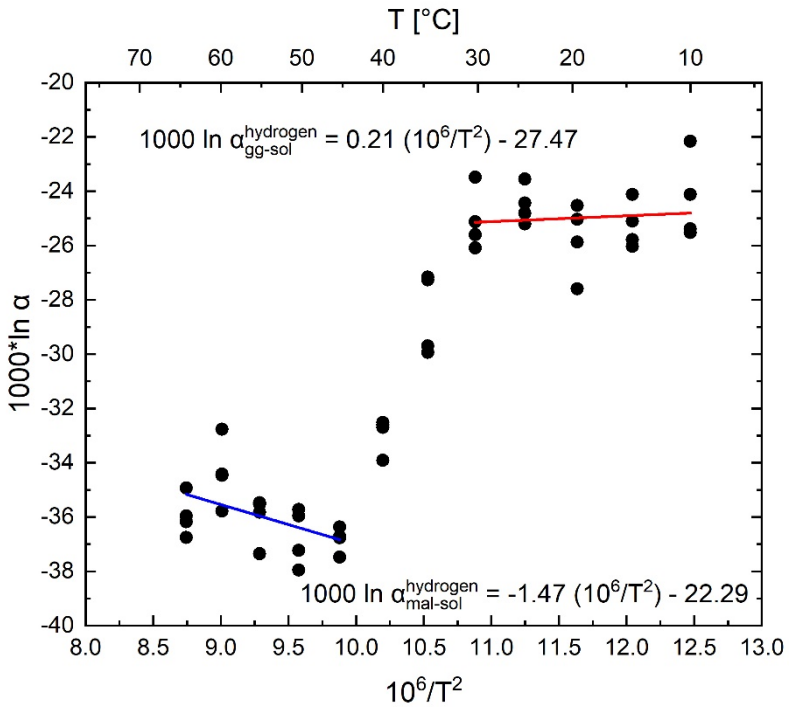

Figure 4-5. Mineral-solution hydrogen isotope fractionation as a function of temperature for this study's results.

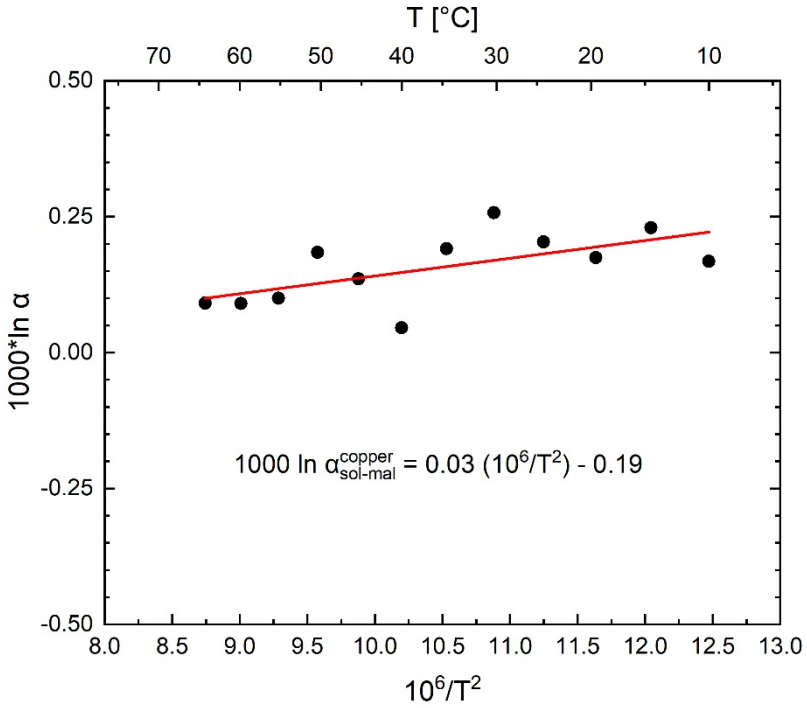

Figure 4-6. Solution-malachite copper isotope fractionation as a function of temperature for this study's results.

The $\delta^{18}O_{VSMOW}$ values of the natural malachites measured in this work range from +22.1 to +29.54 ‰ and the δD values from –132.06 to –65.04 ‰ (Table 4-4). The values for $\delta^{65}Cu$ range from -0.60 to 1.83 ‰ (Table 4-4). We used our calculated fractionation factors of oxygen and hydrogen to determine the oxygen and hydrogen isotopic composition of the parental waters of the malachite samples (Table 4-4).

We calculated the $\delta^{18}O^{wat}_{VSMOW}$ and δD^{wat}_{VSMOW} using the well-known definition of Δ as a function of δ-values $\Delta_{mal\text{-}wat} = \delta_{mal} - \delta_{wat}$ and also the relation $\Delta_{mal\text{-}wat}$=1000 ln $\alpha_{mal\text{-}wat}$ (Criss, 1999). The final equation is $\delta_{wat} = \delta_{mal} - (1000 \ln \alpha_{mal\text{-}wat})$ with the isotopic fractionation factors of oxygen and hydrogen at 15 °C.

*Table 4-4. Isotopic composition of the natural malachite samples. *calculated.*

country	location	malachite $\delta^{18}O_{SMOW}$ ‰	malachite δD_{SMOW} ‰	water* $\delta^{18}O_{SMOW}$ ‰	water* δD_{SMOW} ‰	malachite $\delta^{65}Cu$ ‰	sample name
Russia	Mine Jagowskoi, Ural	23.74	–122.85	–12.90	–97.95	–0.60	HS24510
	Nizhny Tagil, Ural	22.88	–129.21	–13.76	–104.31	–0.20	HS24494
	Gumeshevskoe, Ural	22.10	–132.06	–14.55	–107.17	0.84	HS24545
	Jekaterinenburg	22.97	–121.12	–13.67	–96.23	–0.59	FS4992/194
Slovakia	Ľubietová	26.64	–89.26	–10.00	–64.36	-	L32
	Ľubietová	26.59	–90.98	–10.05	–66.08	-	L43
	Ľubietová	26.52	–96.64	–10.12	–71.74	-	L42
Austria	Schwatz, Tirol	23.23	–109.7	–13.41	–84.83	–0.46	HS24465
Germany	Kamsdorf, Thuringia	26.61	–90.34	–10.03	–65.45	–0.33	HS24357
	Eisenzecher Zug, Siegen	29.39	–66.93	–7.25	–42.03	-	Siegen
France	Chessy-les-Mines	27.77	–65.04	–8.87	–40.15	1.83	HS 24460
	Chessy-les-Mines	26.06	–95.75	–10.58	–70.85	0.33	FS4973/177
Australia	Wallaroo mine	29.54	–61.12	–7.11	–36.22	0.21	HS24535

4.6 Discussion

4.6.1 Isotopic fractionation of Cu carbonate phases at various temperatures

Our data show that the isotopic fractionation data can be fitted to two linear functions, prominently for δD but also for $\delta^{18}O$. The initial hypothesis that malachite forms directly from the solution at higher temperatures, without the interfering georgeite was refuted by our experiments. Georgeite can be detected at all temperatures. Only the rate of its transformation to malachite varies with temperature. Hence, we conclude that the low-temperature data represent isotopic fractionation that was inherited from georgeite and not modified by its transformation to malachite. The higher-temperature data set, on the other hand, represents the isotopic fractionation inherent to malachite, as this phase was able to exchange isotopes rapidly at higher temperatures. These conclusions are supported by a very good match of our data to the precipitation data of Melchiorre et al. (1999), where isotopic equilibrium was also assumed (Fig. 4-4). The enrichment of ^{18}O in malachite compared to the aqueous solution is attributed to low formation temperature and slow precipitation rates (McCrea, 1950; O'Neil et al., 1969). O'Neil et al. (1969) already determined that the isotopic composition of a carbonate precipitated from solution varies with the precipitation rate. So with slow precipitation, the carbonate is markedly more enriched in ^{18}O, presumably as a consequence of the establishment of isotopic equilibrium between the solid and the solution (O'Neil et al., 1969; Urey, 1947). The strong temperature dependence of the oxygen isotope fractionation between malachite and aqueous

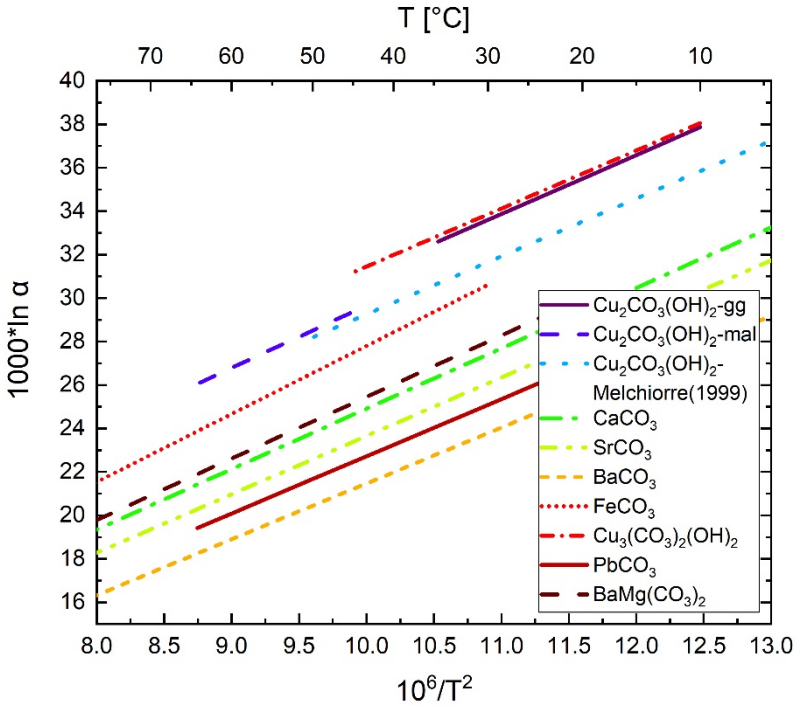

Figure 4-7. Comparison of our mineral-solution oxygen isotope fractionation factors with carbonate-H_2O factors, all plotted as a function of temperature. ($CaCO_3$, $SrCO_3$, $BaCO_3$: Friedman and O'Neil, 1977; $FeCO_3$: Carothers et al., 1988; $Cu_3(CO_3)_2(OH)_2$: Melchiorre et al., 2000; $PbCO_3$: Melchiorre et al., 2001, $BaMg(CO_3)_2$: Bötcher, 2000, details in appendix)

solution represented by $1000 \ln \alpha_{mal-sol}^{oxygen} = 2.87\ (10^6/T^2) + 0.96$ (Fig. 4-4) is well comparable with other oxygen fractionation factors for divalent cation carbonates (Fig. 4-7).

Melchiorre et al. (2000) showed with slow precipitation experiments that the oxygen isotope fractionation between azurite ($Cu_3(CO_3)_2(OH)_2$) and water at low temperatures (10-45 °C) has values for A and B (see eq. 1) of 2.67 and 4.75, respectively (Fig. 4-7), which is comparable to our A value of 2.87. Furthermore, Friedman and O'Neil (1977) have similar A values for calcite ($CaCO_3$, 2.78), strontianite ($SrCO_3$, 2.69) and witherite ($BaCO_3$, 2.57) and Bötcher (2000) for norsethite ($BaMg(CO_3)_2$, 2.83). Therefore, the trend and ranges of $1000 \ln \alpha_{min-sol}^{oxygen}$ functions observed for malachite are generally consistent with functions of oxygen fractionation observed for other divalent cation carbonates (Fig. 4-7).

The hydrogen isotope fractionation between malachite and aqueous solution, which is represented by $1000 \ln \alpha_{mal-sol}^{hydrogen} = -1.47\ (10^6/T^2) - 22.29$, is temperature dependent for temperatures of 45-65 °C. Hydrogen isotope fractionation between some minerals and water is independent of temperature for low temperature processes, e.g. for gibbsite (Vitali et al., 2001) (Fig. 4-8). On the other hand, Gilg and Sheppard (1996) showed that the hydrogen isotope fractionation between kaolinite ($Al_4Si_4O_{10}(OH)_8$) and water is temperature dependent between 0 and 330 °C (Fig. 4-8). Thus, our data matches quite well in the range with other secondary minerals like gibbsite and kaolinite.

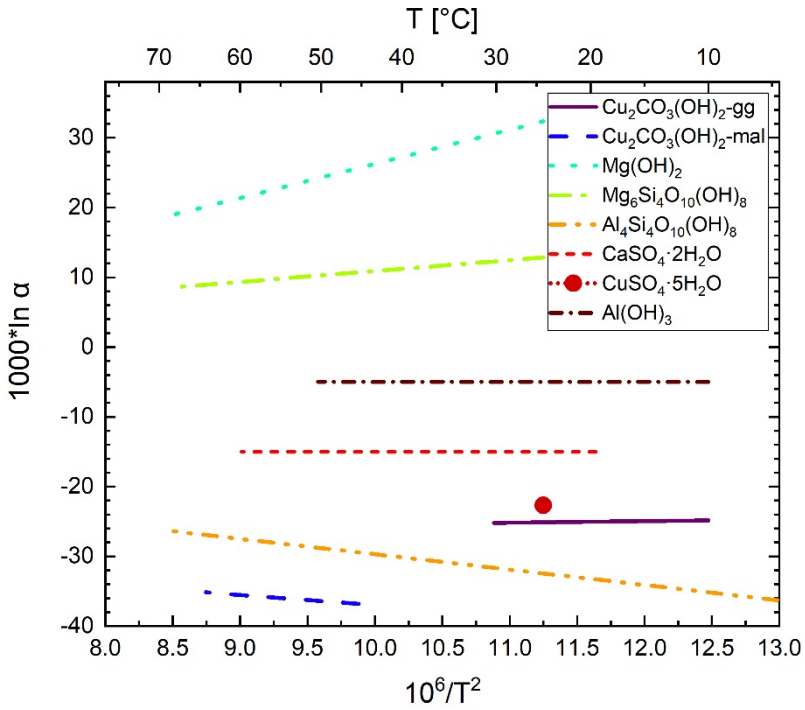

Figure 4-8. Comparison of our mineral-solution hydrogen isotope fractionation factors with mineral-H_2O factors, all plotted as a function of temperature. ($Mg(OH)_2$: Xu and Zheng, 1999; $Mg_6Si_4O_{10}(OH)_8$: Wenner and Taylor, 1973; $Al_4Si_4O_{10}(OH)_8$: Gilg and Sheppard, 1996; $CaSO_4 \cdot 2H_2O$: Fontes and Gonfiantini, 1967; $CuSO_4 \cdot 5H_2O$: Heinzinger, 1969; $Al(OH)_3$: Vitali et al., 2001; details in appendix)

Compared to the hydrogen and oxygen isotope fractionation is the copper isotope fractionation represented by only one linear function of $1000 \ln \alpha_{sol-mal}^{copper} = 0.03\ (10^6/T^2) - 0.19$ but it shows also a very small temperature dependence. For a better comparison of our data to other researchers' data, we applied the definition of the fractionation shift $\Delta^{65}Cu = \delta^{65}Cu_{product} - \delta^{65}Cu_{reactant} \approx 1000 \ln \alpha_{sol-mal}^{copper}$ to our data and yielded a mean value of all temperatures of $\Delta^{65}Cu = -0.16 \pm 0.05$ ‰.

The fractionation shift during the reaction $Cu(II)_{aq} \rightarrow Cu(II)_{malachite}$ is rather small with -0.16 ± 0.05 ‰ (Fig. 4-9, Table 4-5) which implies that chemical reactions without change of the redox state yield only minor copper isotope fractionation. In comparison to that, the fractionation is larger when copper is either oxidized, $\Delta^{65}Cu \approx 1.3$ to 3 ‰, or reduced, $\Delta^{65}Cu \approx -4$ to -2.7 ‰, during the formation process of new phases (Fig. 4-9, Table 4-5) (Ehrlich et al., 2004; Markl et al., 2006; Mathur et al., 2005; Pękala et al., 2011; Qi et al., 2019; Zhu et al., 2000). Zhu et al. (2002) assume that redox reactions are mainly responsible for the copper isotope fractionation. Ehrlich et al. (2004) emphasized the importance of redox reactions and low temperatures for producing significant isotopic fractionation in natural environments (Mathur et al., 2005; Mathur and Fantle, 2015; Zhu et al., 2002). Our experimental results confirm that the redox reactions are the main driving force for isotope fractionation. But Zhu et al. (2002) and Ehrlich et al. (2004) could not completely rule out kinetic fractionation effects. Maréchal and Sheppard (2002) fractionation factors and ours are an order of magnitude smaller than during redox processes. Therewith, it is to assumed that redox processes have by far the largest effect on copper isotope variations and that chemical reactions without change of redox state have only very small effects.

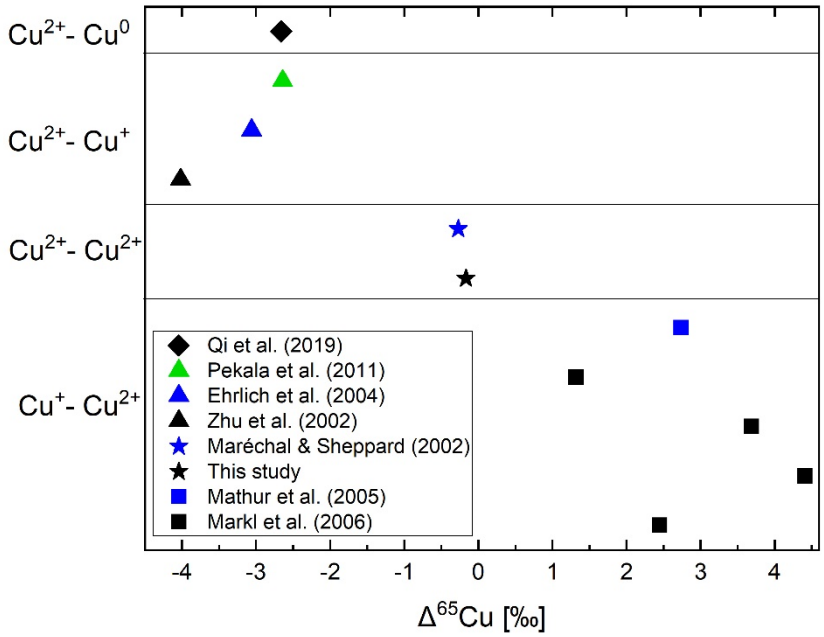

Figure 4-9. $\Delta^{65}Cu$ values that show the relative difference of original reactant to final product. More details in text.

With the oxygen and hydrogen fractionation factors strongly dependent on the inverse temperature, it is to assume that the isotopic fraction of these elements is mainly controlled by the temperature. Pressure has no influence on the oxygen, hydrogen and copper isotope fractionation, also when it is known that pressure can have an influence on hydrogen, experiments have shown that the pressure dependence of hydrogen isotopes were only at high temperatures above 200 °C and more than 0.2 kbar pressure (Chacko et al., 2001). The other parameters that can influence

Table 4-5. Overview of the fractionation pairs of $\Delta^{65}Cu$ values and the experimental methods.

fractionation pair (A-B)		$\Delta^{65}Cu_{B\text{-}A}$	Experimental method	source
Cu(II)-Cu(0)				
$Cu(II)_{aq}$	Cu(0)	–2.66 ± 0.02	reduction during electrodeposition	Qi et al. (2019)
Cu(II)-Cu(I)				
$Cu(II)_{aq}$	Cu(I) mineral	–2.64	reaction of aqueous solute. with Fe sulphides	Pękala et al. (2011)
$Cu(II)_{aq}$	covellite	–3.06 ± 0.14	precipitating CuS from aqueous solution	Ehrlich et al. (2004)
$Cu(II)_{aq}$	Cu(I)-iodide	–4.02 ± 0.06	precipitating from aqueous solution	Zhu et al. (2002)
Cu(II)-Cu(II)				
$Cu(II)_{aq}$	malachite	~ –0.27 ± 0.08	precipitating from aqueous solution	Maréchal and Sheppard (2002)
$Cu(II)_{aq}$	malachite	–0.166 ± 0.054	precipitating from aqueous solution	this work
Cu(I)-Cu(II)				
chalcocite	$Cu(II)_{aq}$	2.74		
chalcopyrite	$Cu(II)_{aq}$	1.32	oxidative leaching experiment	Mathur et al. (2005)
fahlore	olivenite	3.69		
chalcopyrite	malachite	4.41	calculated from mineral pairs of the same specimen	Markl et al. (2006)
chalcopyrite	chrysocolla	2.45		

the isotopic exchange fraction like solution composition, surface area and mineral chemistry were not the focus of this study.

4.6.2 Isotopic composition of natural samples

The isotopic compositions ($\delta^{18}O$ and δD) of our natural malachite samples are shown in Fig. 4-10 and Table 4-4. With this isotopic composition and our fractionation factors, we were able to calculate the isotopic composition of the solution that precipitated malachite in nature (Table 4-4, Fig. 4-10). Compared to their presumed source water, these malachites are enriched in ^{18}O and slightly depleted in deuterium which is a general trend for formation of supergene minerals (Savin and Epstein, 1970). This was also shown by Sheppard et al. (1969) who showed that supergene kaolinite is generally depleted in D and enriched in ^{18}O relative to hypogene clays from which they formed. In order to determine the source of the fluids, it is also helpful to compare the isotopic composition of the solutions to the isotopic composition of rain waters of nearby stations. The $\delta^{18}O$ and δD values for rain water used in this work were extracted from the Global Networks of Isotopes in Precipitation (GNIP) database (IAEA/WMO, 2019; Holko et al., 2012; Stumpp et al., 2014). The locations of the measuring stations of GNIP and of the natural malachite sites are given in Table 4-6.

In Fig. 4-11a, δD values of the rain water are plotted against δD values of the expected parental waters of the malachite samples. Most δD values for the expected parental waters of malachites are slightly heavier than the rain waters they are compared to (Fig. 4-11a). This slight difference is probably due to evaporation or condensation effects that occur during the pathway of the water from surface to underground (e.g. Hoefs, 2018; Ferronsky and Polyakov, 2012). The only exception from this trend is one sample from Chessy-les-Mines where the expected parental water is isotopically lighter. The exact location of the samples from Chessy-les-Mines is not known as

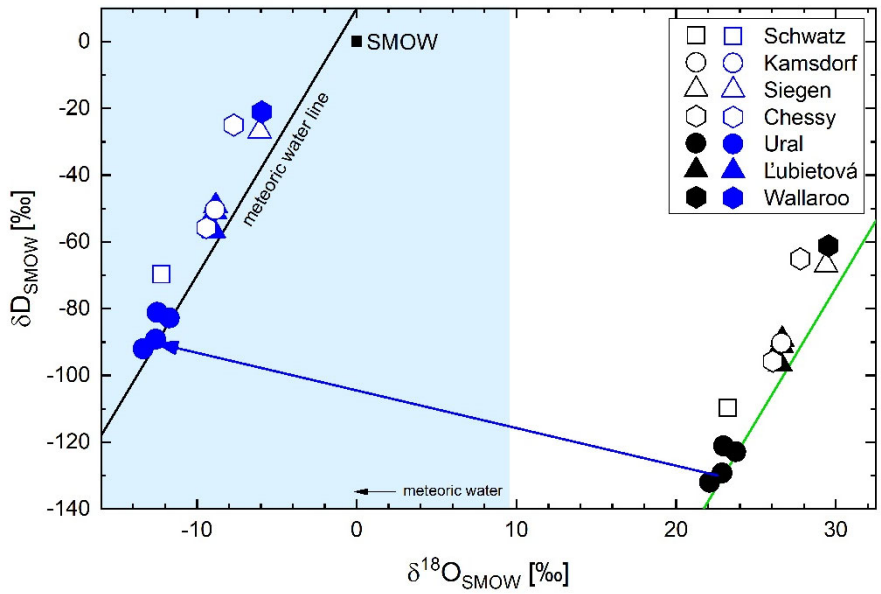

Figure 4-10. $\delta^{18}O$ vs. δD diagram, with the isotopic values of the malachite samples (black symbols) and their respective calculated parental waters (blue symbols). Meteoric water line after Craig (1963).

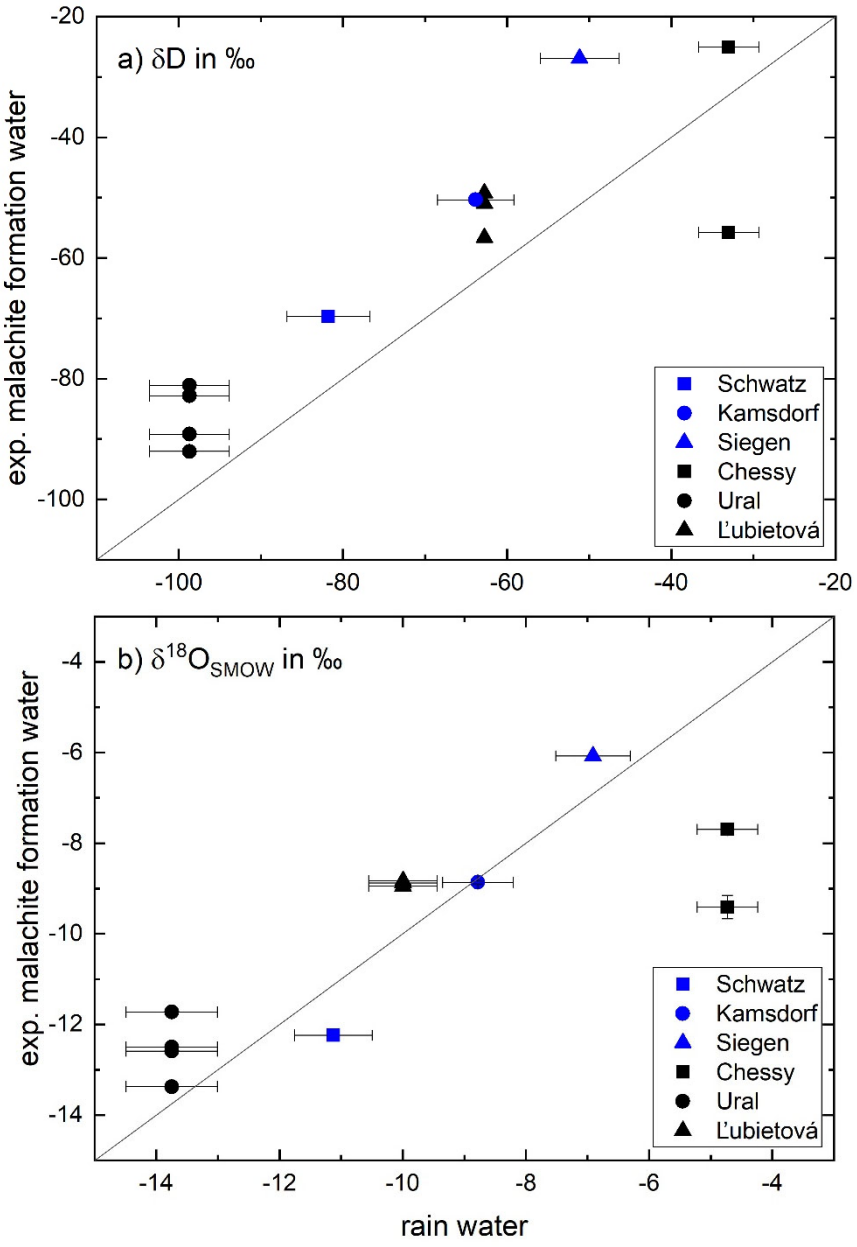

Figure 4-11. Comparison of the rain water (GNIP) and the expected values of the malachite fparental water of δD (a) and δ18O (b) (error bars in y-direction are smaller than data points).

these come from a historical collection without precise data. Therefore, it is not possible to give exact description of the formation of these samples and only a general description.

The comparison of the $\delta^{18}O$ values of the rain water and the expected parental waters of malachite is shown in Fig. 4-11b. The expected parental waters for the malachites from Siegen, Ľubietová and the Ural Mountains are slightly heavier in $\delta^{18}O$ which is probably due to water-rock interactions which will take out the light oxygen isotope and leave the water slightly heavier in ^{18}O (Hoefs, 2018). But also evaporation and condensation effects can lead to heavier $\delta^{18}O$ values (e.g. Hoefs, 2018; Ferronsky and Polyakov, 2012). The $\delta^{18}O$ values for the expected parental waters from Schwatz and Chessy-les-Mines are lighter than the $\delta^{18}O$ values of the compared rain waters. This is due to the fact that the two malachite locations are located in parts of mountain ranges (Schwatz in the Eastern Alps, Chessy-les-Mines in the eastern part of Massif Central)

compared to the locations of the rain water collection which are located in lower altitudes (e.g. Hoefs, 2018; Ferronsky and Polyakov, 2012).

Another implementation of the fractionation factors of malachite is the application onto some source water with which it is possible to predict the isotopic composition of the malachite that would precipitate. The basis of the calculation is the assumption that there is a relationship between the oxygen and hydrogen isotopic composition of malachites like there is for the oxygen and hydrogen isotopes for meteoric water since the isotopic composition of malachite depends on the isotopic composition of water. Therefore, we applied the fractionation factors of oxygen and hydrogen to a source water from the meteoric water line and assumed the same slope (for T = 15 °C). The result is the "malachite line" (Fig. 4-12) which is calculated at different temperatures. This lets us predict at what temperature the malachite samples formed. Something similar was already done before with the "kaolinite line" by Savin and Epstein (1970) and Sheppard et al. (1969). Hence, all our natural malachite samples lie in a temperature range from 15-30°C (Fig. 4-12) which implies meteoric water and not hydrothermal water formed these malachites.

Precautions should be taken by the selection of the samples, so that only well-crystallized minerals will be chosen to apply this method. Extremely fine grained minerals are much more sensitive so significant isotopic exchange at low temperatures and therefore for postdepositional isotopic exchange between the mineral and fluid that can alter the $\delta^{18}O$ value of a mineral. Additionally, these fractionation factors and the application as "malachite line" are only for pure malachite. Significant cation substitutions in natural malachites, like Zn for rosasite, $(Cu,Zn)_2(CO_3)(OH)_2$,

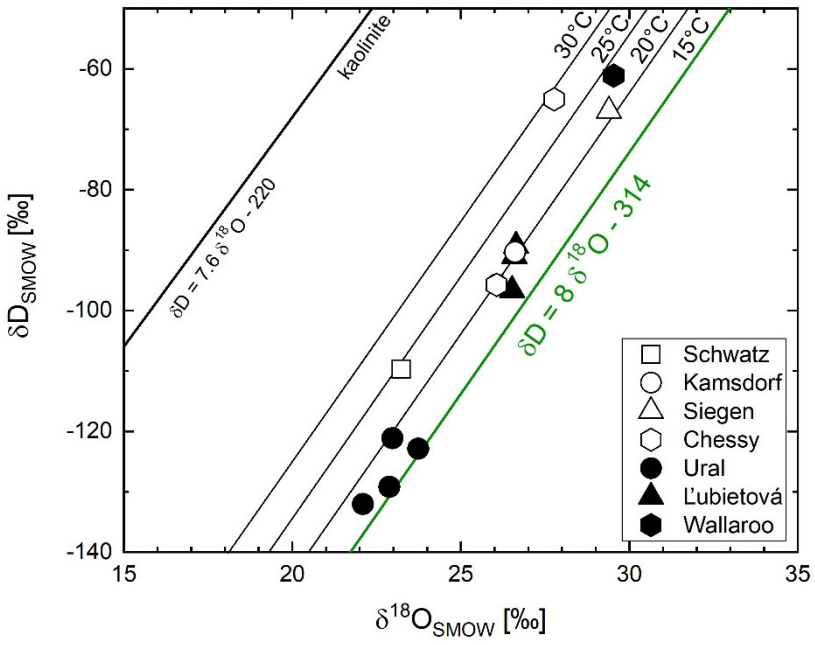

Figure 4-12. $\delta^{18}O$ vs. δD for the natural malachite samples with the calculated "malachite line" at different temperatures. The line "kaolinite" indicates the isotopic variations shown by kaolinites from surface weathering environments Savin and Epstein (1970).

Table 4-6. Natural malachite locations of the rain water measuring stations of GNIP for the comparison.

country	location	GPS location lat. (°)	GPS location long. (°)	measuring station	GPS location lat. (°)	GPS location long. (°)	elevation (m asl)	Reference for station
Russia	Mine Jagowskoi, Ural							
	Nizhny Tagil, Ural	57.92	59.97	Perm, Russia	58.01	56.18	161	GNIP
	Gumeshevskoe, Ural							
	Jekaterinenburg	56.83	60.58					
Slovakia	Ľubietová	48.75	19.37	Chopok, Slovakia	48.93	19.58	2008	(Holko et al., 2012)
Austria	Schwatz, Tirol	45.35	11.7	Garmisch-Partenkirchen, Germany	47.48	11.07	720	(Stumpp et al., 2014)
Germany	Kamsdorf, Thuringia	50.65	11.44	Hof, Germany	50.32	11.88	567	(Stumpp et al., 2014)
	Eisenzecher Zug, Siegen	50.82	7.99	Koblenz, Germany	50.35	7.58	97	(Stumpp et al., 2014)
France	Chessy-les-Mines	45.90	4.61	Carpentras, France	44.95	5.78	99	GNIP

may affect fractionation behaviour. As long as the magnitude of such effects is unclear, the fractionation factors can only be applied for pure end-member malachite.

The isotopic composition of copper in the natural malachite samples ranges from -0.6 to 1.83 ‰ (Table 4-4), with the majority of δ^{65}Cu between -0.6 and 0.84 ‰. It is important to mention that none of the δ^{65}Cu values are 0 ± 0.2 ‰ because this would be an indication for primary, unaltered Cu sulfide minerals (Maréchal et al., 1999; Zhu et al., 2000; Larson et al., 2003; Graham et al., 2004; Rouxel et al., 2004; Mason et al., 2005; Mathur et al., 2005; Markl et al., 2006; Asael et al., 2007). In comparison to that, δ^{65}Cu values which are greater or less than 0 ‰ are associated with formation during some type of low temperature process (Rouxel et al., 2004; Mathur et al., 2005; Markl et al., 2006) and therefore mainly supergene.

4.7 Summary and conclusion

Our experimental study of the copper, oxygen and hydrogen isotope fractionation during the precipitation of malachite from aqueous solution at 10 to 65 °C shows that isotopes are a strong tool for the determination of formation processes of secondary minerals in ore deposits.

Even so it is not possible to demonstrate conclusively that our synthetic malachites formed in isotopic equilibrium, available evidence suggests that equilibrium was attained or closely approximated in the precipitation experiments. For example, the application of the fractionation factors to data for natural samples suggests temperatures with the formation of malachite as a weathering product. Also the relationship between the oxygen and hydrogen isotope ratios of malachite results from the weathering with meteoric waters under conditions in which the fractionation factors are relatively constant. This also

strongly suggests that the fractionation factors are in equilibrium and that malachite forms in isotopic equilibrium with its environment.

Additionally, we have shown an inverse temperature dependence on $1/T^2$ for the hydrogen, oxygen and copper isotopic fractionation which is expected for equilibrium isotope fractionation by stable isotope theory (Bigeleisen and Mayer, 1947; Urey, 1947).

Our precipitation experiments in this work most probably reflect an abiogenic process by which copper carbonates form in low temperature natural environments. Thus, regardless of how closely equilibrium is approached in the experiments, the fractionation factors derived here can be considered to provide a valid proxy for the natural situation involving abiogenic malachite formation. During precipitation experiments like ours, copper isotope fractionation can occur either during redox reaction in solution or during the precipitation of the new phase. Since in our experiments occurs no redox reaction, the small fractionation of the copper isotopes is due to the precipitation of the new phase. Therewith, it is to assumed that redox processes have by far the largest effect on copper isotope variations and that chemical reactions without change of redox state have only very small effects.

In conclusion for the natural samples, we have shown that all investigated natural samples in this study are supergene samples which formed through meteoric water. Even in massive malachite samples from the Ural Mountains, we found no signs of other fluids based on the isotopic composition.

4.8 Acknowledgements

The work presented here was financially supported by a grant of the *Deutsche Forschungsgemeinschaft* MA 3927/26-1. We thank the Université d'Avignon et des Pays de Vaucluse staff in Avignon, France for help with performing the precipitation sampling and the measurements at Carpentras, France. We thank the Hydrometeorological Institute and Water Problems Inst., Acad. Of Sciences staff in Moscow, Russia for help with performing the precipitation sampling and the measurements at Perm, Russia.

5 Exposition of the results and perspective

In this chapter, the major conclusions and key findings of my work will be shown as well as work that still has to be done. This work aimed

(i) to determine the thermodynamic properties of a suite of endmember copper arsenate (liroconite, geminite, pushcharovskite, olivenite), zinc arsenate (adamite) and copper phosphate (libethenite) minerals
(ii) to determine the thermodynamic properties of the olivenite–libethenite solid solution series
(iii) to clarify the ideal or nonideal character of the olivenite–libethenite solid solution series
(iv) to further understand the exchange mechanism between As and P
(v) to integrate the thermodynamic data into an internally consistent thermodynamic database to model the evolution of oxidation zones and copper arsenate precipitation
(vi) to clarify the isotopic fractionation of copper, hydrogen and oxygen between malachite and an aqueous phase.

5.1 Major conclusions and key findings

5.1.1 Thermodynamic properties

Of the widespread and variable group of copper arsenates and related minerals, we determined the thermodynamic properties of liroconite ($Cu_2Al(AsO_4)(OH)_4 \cdot 4H_2O$), geminite ($Cu(AsO_3OH)(H_2O)$), pushcharovskite ($Cu(AsO_3OH)(H_2O) \cdot 0.5H_2O$), olivenite ($Cu_2(AsO_4)(OH)$), libethenite ($Cu_2(PO_4)(OH)$), adamite ($Zn_2(AsO_4)(OH)$) and zincolivenite ($CuZn(AsO_4)(OH)$).

Liroconite is a rare mineral, except for several localities, notably Wheal Gorland in England. The most common supergene minerals directly associated with liroconite are other copper arsenates, especially olivenite, strashimirite and clinoclase. The temporal relationship of liroconite and all its associated phases is complex with local conditions of formation that moved in, out and returned to areas of pH-pε that were suitable for liroconite growth. Thermodynamic modelling showed that the initial stage of weathering was probably marked by low pH, typically for initial sulfide weathering or acid mine drainage. Fluctuations in the weathering and kaolinization intensity resulted in multiple liroconite generations, associated with olivenite and other copper arsenates which may have formed at mildly acidic to circumneutral conditions. In the main stage, we assume that Al(III) rich fluids are responsible for the liroconite formation during contemporaneous oxidation of primary Cu–As ores and pervasive kaolinization of the host peraluminous granites. In detail, our calculations predict that the formation of kaolinite must have been preceded by the release of Al(III) and $SiO_2(aq)$ from the rock-forming feldspars and

precipitation of X-ray amorphous $Al(OH)_3$ as a precursor to kaolinite and gibbsite. pH had to be kept in mildly acidic (5-6) conditions and the activities of dissolved silica were too low to form dioptase. Due to the exhaustion of the acidity-generation capacity of the sulfides and cessation of kaolinization processes, the condition were near-neutral to mildly basic with elevated $p(CO_2,g)$ and led to the formation of copper carbonates. In sum, the formation of liroconite requires circumneutral fluids in an Al-rich environment that is poor in Fe, Pb or other interfering metals.

Geminite and pushcharovskite, on the other hand, are minerals typical for very acidic solutions. At the studied site in Jáchymov (Czech Republic), geminite belongs to the less common arsenate minerals, yet it has been reported in several distinctive weathering associations on different ore veins. The sources of Cu and As are probably tennantite, bornite and chalcocite, which occur in the nearby veins. Geminite associates with other acidic minerals, such as slavkovite, yvonite, and minerals of the lindackerite group ($ACu_4(AsO_4)_2(AsO_3OH)_2{\cdot}9H_2O$ with A = Cu, Zn, Co, Ca, Ni, Mg) but also with arsenolite and lavendulan. From its type locality in the Salsigne mine (France, Sarp and Černý, 1998), geminite was described in association with yvonite, lindackerite, and pushcharovskite. All these minerals should be expected to crystallite from strongly acidic solutions. Sulfate is removed by formation of gypsum. Carbonates are either not present or accessory.

So far only two localities of pushcharovskite are known including its type locality Cap Garonne, Var, France, where it is associated with geminite, lindackerite, yvonite and mahnertite in a quartz gangue (Sarp and Sanz-Gysler, 1997). Our calculations show that pushcharovskite is metastable with respect to geminite. Hence, pushcharovskite can be seen as a metastable precursor to

Table 5-1. Overview of minerals mentioned in this chapter, together with their formula.

Mineral name	Mineral formula
Adamite	$Zn_2(AsO_4)(OH)$
Arsenolite	As_2O_3
Bornite	Cu_5FeS_4
Chalcocite	Cu_2S
Dioptase	$CuSiO_3{\cdot}H_2O$
Geminite	$Cu(AsO_3OH)(H_2O)$
Gibbsite	$Al(OH)_3$
Kaolinite	$Al_2(Si_2O_5)(OH)_4$
Lavendulan	$NaCaCu_5(AsO_4)_4Cl{\cdot}5H_2O$
Libethenite	$Cu_2(PO_4)(OH)$
Lindackerite	$CuCu_4(AsO_4)_2(AsO_3OH)_2{\cdot}9H_2O$
Liroconite	$Cu_2Al(AsO_4)(OH)_4{\cdot}4H_2O$
Mahnertite	$NaCu_3(AsO_4)_2Cl{\cdot}5H_2O$
Olivenite	$Cu_2(AsO_4)(OH)$
Pushcharovskite	$Cu(AsO_3OH)(H_2O){\cdot}0.5H_2O$
Slavkovite	$Cu_{13}(AsO_4)_6(AsO_3OH)_4{\cdot}23H_2O$
Tennantite	$Cu_6(Cu_4X_2)As_4S_{12}S$, X=Fe^{2+}, Zn
Yvonite	$Cu(AsO_3OH)(H_2O){\cdot}H_2O$
Zincolivenite	$CuZn(AsO_4)(OH)$

geminite which is itself metastable with respect to olivenite but probably forms faster under acidic conditions. Because of its marked metastability, pushcharovskite should only be a transient phase that rapidly dehydrates to geminite. That would also explain its extreme rarity in nature.

Olivenite is the most common copper arsenate in the supergene environment of copper ore deposits containing arsenic-bearing phases (Anthony et al., 2000). Following, it is found in many localities worldwide, like in the type locality Carharrack Mine in Cornwall (UK), in Cap Garonne (Var, France) and in Tsumeb (Namibia).

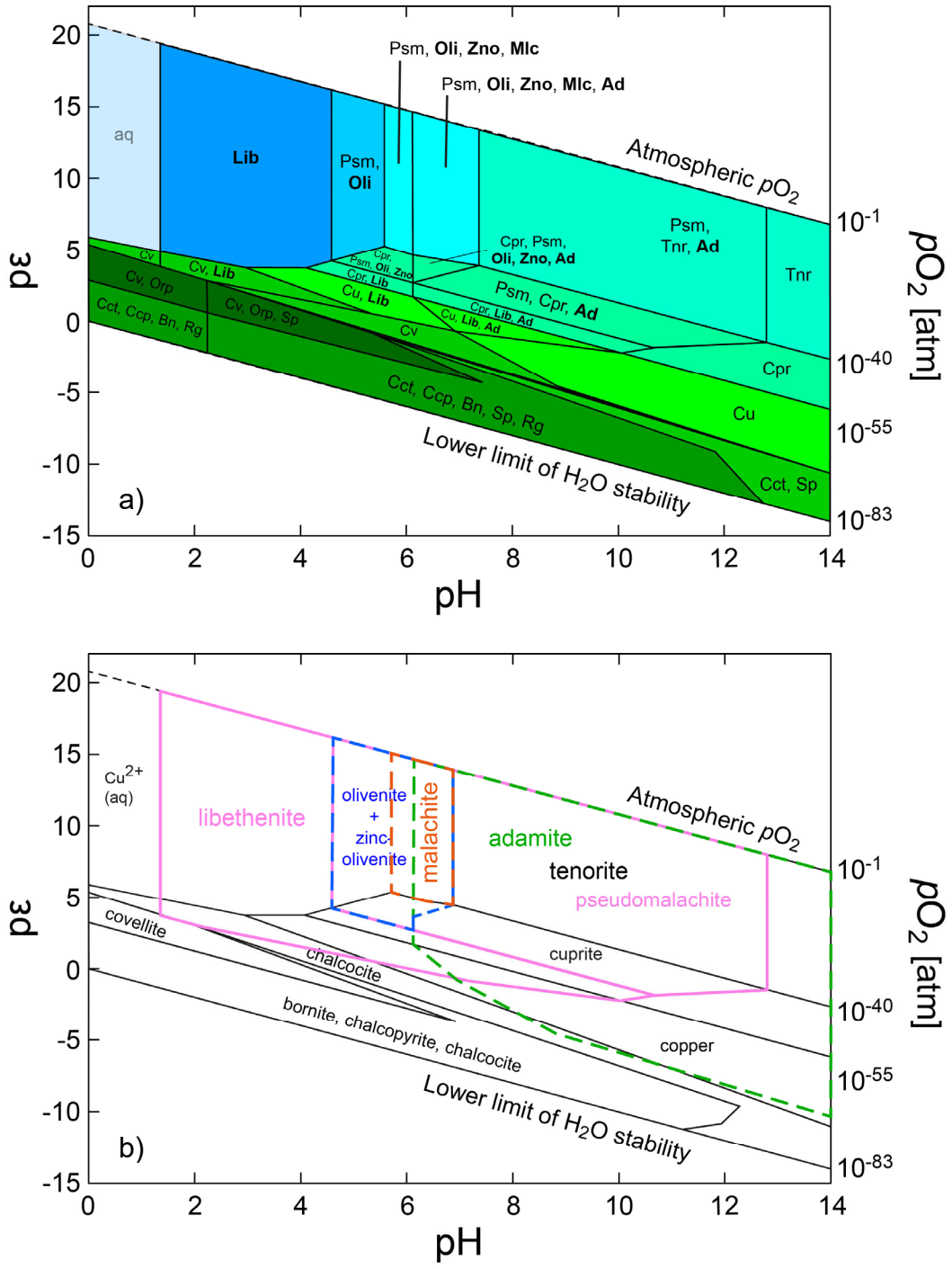

Figure 5-1. a) pH-pε phase diagram for a suite of copper and zinc minerals, including copper phosphates, arsenates and zinc arsenates. T = 25 °C, log a[Cu(II)] = -4, log a[Zn(II)] = -4, log a[P(V)] = -5, log a[As(V)] = -4, log a[S(-II)] = -5. b) sketch of a) for better visibility of the stability fields of the minerals of interest.

Zincolivenite is an approved mineral by IMA since 2006 and is a structurally distinct, intermediate member of the olivenite-adamite solid solution series with a Zn:Cu ratio from 1:3 to 3:1 (Chukanov et al., 2007). Prior to the approval, 'zinc-olivenite' and 'cuprian-adamite' were common declarations for intermediate members of the olivenite-adamite solid solution series whereby not yet all specimens and localities were newly determined. Therefore, only a few localities are known so far, like the type locality in East Attica (Greece), Tsumeb (Namibia) and Cornwall (England, UK).

Adamite is a secondary mineral in the oxidized zone of zinc- and copper-bearing mineral deposits and is distributed in a number of localities like Chanarcillo (Atacama, Chile), Tsumeb (Namibia) and Cap Garonne (Var, France).

Libethenite is a common copper phosphate which usually occurs only in small amounts in the supergene environment of copper ore deposits. Some of the most known localities are L'ubietova (Libethen in german, Slovakia), Cornwall (England, UK) and Nizhni Tagil (Ural Mountains, Russia).

Stability of the adamite, zincolivenite, olivenite, libethenite and malachite

The arsenates adamite, zincolivenite and olivenite as well as the phosphate libethenite and the carbonate malachite have stability fields in pH-pε space (Fig. 5-1).

Adamite is stable in a wide range of pH from neutral to alkaline conditions and will be stabilized by increasing the activity of Zn(II) (Fig. 5-1 and Fig. 5-2). With high activities of Cu(II) over 10^{-2}, adamite will not be stable and olivenite will form (Fig. 5-2). Therefore, the replacement and the formation of a solid solution series between adamite, zincolivenite and olivenite can be caused by the variation of pH or the activities of the aqueous species.

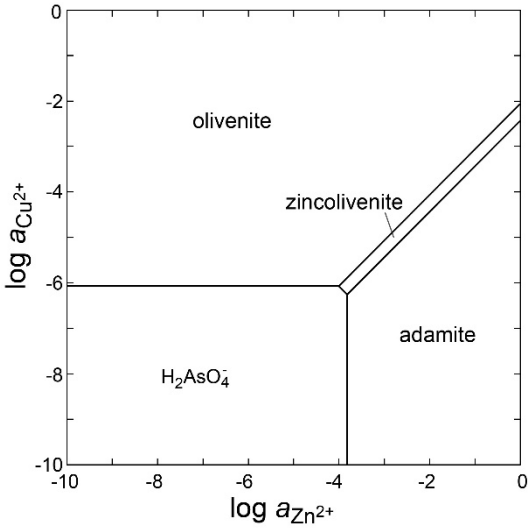

Figure 5-2. Activity-activity phase diagram for copper and zinc arsenates. T = 25 °C, log a[As(V)] = -4, pH = 6.

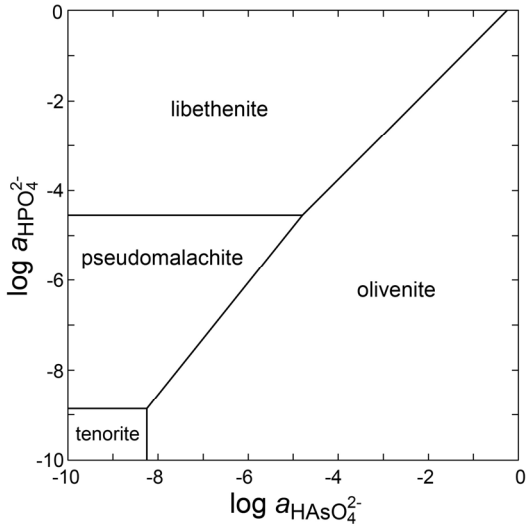

Figure 5-3. Activity-activity phase diagram for copper phosphates, arsenates and tenorite. T = 25 °C, log a[Cu(II)] = -4, pH = 6. (self calculated after Majzlan et al., 2015)

Libethenite is stable at lower pH and lower pε as olivenite and will be stabilized by increasing the activity of the phosphate species (Fig. 5-1 and Fig 5-3). Hence, the formation of members of the solid solution series between olivenite and libethenite can be caused by the variation of pH, pε or the activities of the aqueous species. (Further discussion in Ch. 5.2)

It should be noted that the diagram (Fig. 5-1) does not contain stability fields of other Cu arsenates, like euchroite, geminite or pushcharovskite, although their thermodynamic data are also taken into account in the calculations. The reason for this is the metastability of these minerals compared to olivenite (see Ch. 2 and Majzlan et al., 2017b).

Malachite is stable in slightly acidic conditions and at pCO_2 levels between $10^{-2.5}$ and 10^{4} (Kiseleva et al., 1992, Rose, 1989).

5.1.2 Crystal structures of the olivenite-libethenite series

A complete olivenite-libethenite solid solution series was synthesized and examined with pXRD, FT-IR and ICP-OES. The chemical analysis showed that we were able to synthesize the olivenite-libethenite solid solutions series in steps of 0.10 ± 0.01 apfu for the P and As content (Table 3-3). The end members of this solid solution belong to two different crystal systems: olivenite is monoclinic and libethenite is orthorhombic. The difference is in the crystallographic angle α from up to 90.13° for olivenite (Li et al., 2008) to 90.0° for libethenite. Therefore, the Rietveld analysis suggests an evolution of the unit cell parameters following the size of the ionic radii as a result of substitution of As^{5+} by the smaller P^{5+}. The IR-spectra show the evolution of the bands corresponding to the PO_4 and AsO_4 tetrahedron and also changes in the vibrations of the OH groups.

Furthermore, the crystallographic analysis shows a negative excess volume of mixing for arsenic-rich solid solution members and a positive excess volume of mixing for phosphoric-rich phases which could be an indication that two solid solutions exist. Additionally, this would be complicated by the symmetry change from monoclinic (olivenite) to orthorhombic (libethenite) between $X_{lib} = 0.69$ and 0.79 which is also shown by the calculated ΔH^{MIX} values. This asymmetry of the excess enthalpy of mixing shows the easier incorporation of a smaller cation (P^{5+}) into a larger site (As^{5+}) than vice versa. Taken all together, we have shown that a complete olivenite–libethenite solid solution exists without miscibility gap.

5.1.3 Isotopic studies of malachite

Since malachite is a common secondary mineral in the oxidation zones of ore deposits, we examined its fractionation factors of copper, oxygen and hydrogen isotopes. We determined the isotope fractionation between malachite and solution by precipitation experiments over the temperature range from 10 to 65 °C. The fractionation factors could be distinguished into two sets of fractionation depending on temperature: 10-35 °C and 45-65 °C. The application of the fractionation factors to data for natural samples suggests temperatures with the formation of

malachite as a weathering product. Our oxygen and hydrogen fractionation factors are well comparable with fractionation factors of other carbonates and secondary OH-containing minerals. Also the relationship between the oxygen and hydrogen isotope ratios of malachite results from the weathering with meteoric waters under conditions in which the fractionation factors are relatively constant.

During precipitation experiments like ours, copper isotope fractionation can occur either during redox reaction in solution or during the precipitation of the new phase. Since in our experiments no redox reaction occurs, the small fractionation of the copper isotopes is due to the precipitation of the new phase. Therewith, it is to be assumed that redox processes have by far the largest effect on copper isotope variations and that chemical reactions without change of redox state have only very small effects.

Summarizing, our experimental study of the copper, oxygen and hydrogen isotope fractionation during the precipitation of malachite from aqueous solution at 10 to 65 °C shows that isotopes are a strong tool for the determination of formation processes of secondary minerals in ore deposits.

5.2 Future perspectives

One important point for a better understanding of the evolution of oxidation zones and to better predict the fate of them is the analysis of more copper arsenates (e.g. strashimirite, parnauite and chalcophyllite). This would lead to more complete datasets for calculations that are closer to nature and to get a better understanding of the formation and stability fields of these minerals.

There should also be further work on the understanding of the substitution mechanism in solid solutions and how this can affect the assemblage of a supergene zone. Additionally, SEM pictures could be used to analyse the correlation between the changes in crystal morphology and the composition. And as already mentioned in chapter 4, it is important to measure the heat capacity of all solid solution members of the olivenite-libethenite and olivenite-adamite series to get the non-ideal entropy of mixing and a better insight into the thermodynamic properties of the solid solutions.

Another fact for the understanding of the secondary minerals is the consideration of the assemblages and the sequences of precipitation. This was mainly done in this work for liroconite, geminite and pushcharovskite and should be done for copper arsenates. The thoughts behind the sequences of precipitation are under what conditions are arsenates superseded by other minerals and what are more stable phases or less stable ones. It can also give us an insight to what extent the mineralogical evolution of an oxidation zone is coupled to global or local changes. This also includes more investigations of stable isotopes (e.g. O, H, C, S) of secondary minerals to get a better insight of the evolution of oxidation zones of ore deposits. Not only for the traditional stable isotopes but also for the non-traditional isotopes like Cu, Zn and Fe.

6 References

Anthony, J. B., Bideaux, R. A., Bladh, K. W., and Nichols, M. C. (Eds.): Handbook of Mineralogy, Chantilly, VA, USA, 2000.

Arne, L.: Nature and formation processes of the supergene Pb-Zn-Cu-V mineralisation of Bamba Kilenda, Bas-Congo province, DR Congo, PhD Dissertation, University Gent, 121 pp., 2014.

Asael, D., Matthews, A., Bar-Matthews, M., Harlavan, Y., and Segal, I.: Tracking redox controls and sources of sedimentary mineralization using copper and lead isotopes, Chem. Geol., 310-311, 23–35, https://doi.org/10.1016/j.chemgeo.2012.03.021, 2012.

Asael, D., Matthews, A., Bar-Matthews, M., and Halicz, L.: Copper isotope fractionation in sedimentary copper mineralization (Timna Valley, Israel), Chem. Geol., 243, 238–254, https://doi.org/10.1016/j.chemgeo.2007.06.007, 2007.

Benisek, A., Kroll, H., and Dachs, E.: The heat capacity of fayalite at high temperatures, Am. Mineral., 97, 657–660, https://doi.org/10.2138/am.2012.3924, 2012.

Bethke, C.: Geochemical and biogeochemical reaction modeling, 2nd ed., Cambridge University Press, Cambridge, New York, xix, 543, 2011.

Bethke, C., Farrell, B., and Yeakel, S.: GWB Reaction Modeling Guide, 12th ed., Champaign, Illinois, 2019.

Bigeleisen, J. and Mayer, M. G.: Calculation of Equilibrium Constants for Isotopic Exchange Reactions, J. Chem. Phys., 15, 261–267, https://doi.org/10.1063/1.1746492, 1947.

Borg, G.: A Review of Supergene Nonsulphide Zinc (SNSZ) Deposits - the 2014 Update, in: Current perspectives on zinc deposits, edited by: Archibald, S. M. and Piercey, S. J., Irish Association for Economic Geology, Dublin, 123–147, 2015.

Bötcher, M. E.: Stable Isotope Fractionation during Experimental Formation of Norsethite ($BaMg[CO_3]_2$): A Mineral Analogue of Dolomite, Aquat. Geochem., 6, 201–212, https://doi.org/10.1023/A:1009646805933, 2000.

Bournon, C. de: Description of the Arseniates of Copper, and of Iron, from the County of Cornwall, Phil. Trans., 91, 169–192, 1801.

Bowell, R. J. and Craw, D.: The management of arsenic in the mining industry, in: Environmental Mineralogy and Bio-Geochemistry of Arsenic, edited by: Bowell, R., Alpers, C. N., Jamieson, H., Nordstrom, K., and Majzlan, J., De Gruyter, Boston, 507–532, 2014.

Bowell, R. J., Alpers, C. N., Jamieson, H. E., Nordstrom, D. K., and Majzlan, J.: The Environmental Geochemistry of Arsenic—An Overview --, in: Environmental Mineralogy and Bio-Geochemistry of Arsenic, edited by: Bowell, R., Alpers, C. N., Jamieson, H., Nordstrom, K., and Majzlan, J., DE GRUYTER, Boston, 1–16, https://doi.org/10.2138/rmg.2014.79.1, 2014.

Braithwaite, R. S. W., Pritchard, R. G., Paar, W. H., and Pattrick, R. A. D.: A new mineral, zincolibethenite, $CuZnPO_4OH$, a stoichiometric species of specific site occupancy, Mineral. Mag., 69, 145–153, https://doi.org/10.1180/0026461056920242, 2005.

Braithwaite, R. S.W.: Infrared spectroscopic analysis of the olivenite-adamite series, and of phosphate substitution in olivenite, Mineral. Mag., 47, 51–57, 1983.

Brown, I. D.: Recent developments in the methods and applications of the bond valence model, Chem. Rev., 109, 6858–6919, https://doi.org/10.1021/cr900053k, 2009.

Brown, I. D.: The Chemical Bond in Inorganic Chemistry: The Bond Valence Model, Oxford University Press, United Kingdom, 2002.

Bruker: TOPAS, Bruker AXS, Karlsruhe, Germany, 2009.

Burns, P. C. and Hawthorne, F. C.: Coordination-geometry structural pathways in Cu^{2+} oxysalt minerals, Can. Mineral., 33, 889–905, 1995a.

Burns, P. C. and Hawthorne, F. C.: Rietveld refinement of the crystal structure of olivenite: a twinned monoclinic structure, Can. Mineral., 33, 885–888, 1995b.

Burns, P. C., Eby, R. K., and Hawthorne, F. C.: Refinement of the structure of liroconite, a heteropolyhedral framework oxysalt mineral, Acta Crystallogr. C, 47, 916–919, https://doi.org/10.1107/S0108270190010939, 1991.

Chacko, T., Cole, D. R., and Horita, J.: Equilibrium Oxygen, Hydrogen and Carbon Isotope Fractionation Factors Applicable to Geologic Systems, Rev. Mineral. Geochem., 43, 1–81, https://doi.org/10.2138/gsrmg.43.1.1, 2001.

Charoy, B.: The Genesis of the Cornubian Batholith (South-West England): The example of the Carnmenellis Pluton, J. Petrol., 27, 571–604, https://doi.org/10.1093/petrology/27.3.571, 1986.

Chesley, J. T., Halliday, A. N., Snee, L. W., Mezger, K., Shepherd, T. J., and Scrivener, R. C.: Thermochronology of the Cornubian batholith in southwest England: Implications for pluton emplacement and protracted hydrothermal mineralization, Geochim. Cosmochim. Acta, 57, 1817–1835, https://doi.org/10.1016/0016-7037(93)90115-D, 1993.

Chukanov, N. V., Pushcharovsky, D. Y., Zubkova, N. V., Pekov, I. V., Pasero, M., Merlino, S., Möckel, S., Rabadanov, M. K., and Belakovskiy, D. I.: Zincolivenite $CuZn(AsO_4)(OH)$: A new adamite-group mineral with ordered distribution of Cu and Zn, Dokl. Earth Sci., 415, 841–845, https://doi.org/10.1134/S1028334X07060037, 2007.

Chukanov, N. V.: Infrared spectra of mineral species: Extended library, Springer Geochemistry/Mineralogy, Springer Netherlands; Imprint: Springer, Dordrecht, 2014.

Ciesielczuk, J., Janeczek, J., Dulski, M., and Krzykawski, T.: Pseudomalachite–cornwallite and kipushite–philipsburgite solid solutions: chemical composition and Raman spectroscopy, EJM, 28, 555–569, https://doi.org/10.1127/ejm/2016/0028-2536, 2016.

Clayton, R. N. and Epstein, S.: The Use of Oxygen Isotopes in High-Temperature Geological Thermometry, J. Geol., 69, 447–452, https://doi.org/10.1086/626760, 1961.

Coelho, A. A.: TOPAS and TOPAS-Academic: an optimization program integrating computer algebra and crystallographic objects written in C++, J. Appl. Crystallogr., 51, 210–218, https://doi.org/10.1107/S1600576718000183, 2018.

Cole, D. R. and Chakraborty, S.: Rates and Mechanisms of Isotopic Exchange, Rev. Mineral. Geochem., 43, 83–223, https://doi.org/10.2138/gsrmg.43.1.83, 2001.

Conor, C., Raymond, O., Baker, T., Teale, G., Say, P., and Lowe, G.: Alteration and Mineralisation in the Moonta-Wallaroo Cu-Au Mining Field Region, Olympic Domain, South Australia, in: Hydrothermal Iron Oxide Copper-Gold and Related Deposits; A Global Perspective: Vol. 3: Advances in the Understanding of IOCG Deposits, edited by: Porter, T. M., PGC Publishing, Linden Park, 147–170, 2010.

Cordsen, A.: A crystal-structure refinement of libethenite, Can. Mineral., 16, 153–157, 1978.

Craig, H.: Isotopic Variations in Meteoric Waters, Science, 133, 1702–1703, https://doi.org/10.1126/science.133.3465.1702, 1961.

Criss, R. E.: Principles of stable isotope distribution, Oxford University Press, New York, 254 pp., 1999.

Criss, R. E., Gregory, R. T., and Taylor, H. P.: Kinetic theory of oxygen isotopic exchange between minerals and water, Geochim. Cosmochim. Acta, 51, 1099–1108, https://doi.org/10.1016/0016-7037(87)90203-1, 1987.

Decker, H. and Rüger, F.: Der Kamsdorfer Bergbau und seine Mineralien, in: Mineralien, Geologie und Bergbau in Ostthüringen, edited by: Museum für Naturkunde, Bode, 80–88, 1991.

Del Nero, M. and Fritz, B.: Thermodynamic modelling of the influence of water activity on the gibbsite-kaolinite-quartz system in lateritic weathering conditions, Chem. Geol., 84, 45–48, https://doi.org/10.1016/0009-2541(90)90160-9, 1990.

Dill, H. G.: Supergene Alteration of Ore Deposits: From Nature to Humans, Elements, 11, 311–316, https://doi.org/10.2113/gselements.11.5.311, 2015.

Ehrlich, S., Butler, I. B., Halicz, L., Rickard, D., Oldroyd, A., and Matthews, A.: Experimental study of the copper isotope fractionation between aqueous Cu(II) and covellite, CuS, Chem. Geol., 209, 259–269, https://doi.org/10.1016/j.chemgeo.2004.06.010, 2004.

Ferronsky, V. I. and Polyakov, V. A.: Isotopes of the Earths Hydrosphere, Springer Netherlands, 646 Seiten, 2012.

Fleischer, M. and Mandarino, J. A.: Glossary of mineral species, 7th ed, Mineral Record, Tucson, Arizona, 1995.

Friedman, I. and O'Neil, J. R.: Compilation of Stable Isotope Fractionation Factors of Geochemical Interest., U. S. Geol. Surv. Prof. Paper 440-KK, 1977.

Frost, R. L., Martens, W. N., and Williams, P. A.: Raman spectroscopy of the phase-related basic copper arsenate minerals olivenite, cornwallite, cornubite and clinoclase, J. Raman Spectrosc., 33, 475–484, https://doi.org/10.1002/jrs.880, 2002.

Gagné, O. C. and Hawthorne, F. C.: Comprehensive derivation of bond-valence parameters for ion pairs involving oxygen, Acta Crystallogr. B, 71, 562–578, https://doi.org/10.1107/S2052520615016297, 2015.

Gilg, H. A. and Sheppard, S. M.F.: Hydrogen isotope fractionation between kaolinite and water revisited, Geochim. Cosmochim. Acta, 60, 529–533, https://doi.org/10.1016/0016-7037(95)00417-3, 1996.

Giuseppetti, G., Coda, A., Mazzi, F., and Tadini, C.: La struttura cristallina della liroconite $Cu_2Al[(As_1P)O_4(OH)_4]\cdot 4H_2O$, Period. Mineral, 31, 19–42, 1962.

Gołębiowska, B., Pieczka, A., and Franus, W.: Olivenite-Adamite Solid Solution From Oxidation Zone in Rędziny (West Sudetes, Poland), Mineralogia, 37, 101–110, https://doi.org/10.2478/v10002-007-0001-1, 2006.

Golze, R., Henrich, M., Hucko, S., and Stötzel, N.: Siegerland & Westerwald: Bergbaugeschichte - Mineralienschätze - Fundorte, Edition Krüger-Stiftung, Bode, Salzhemmendorf-Lauenstein, 800 pp., 2013.

Graham, S., Pearson, N., Jackson, S., Griffin, W., and O'Reilly, S.Y.: Tracing Cu and Fe from source to porphyry: in situ determination of Cu and Fe isotope ratios in sulfides from the Grasberg Cu–Au deposit, Chem. Geol., 207, 147–169, https://doi.org/10.1016/j.chemgeo.2004.02.009, 2004.

Gregory, R. T. and Criss, R. E.: Isotopic exchange in open and closed systems, Rev. Mineral. Geochem., 16, 91–127, 1986.

Grenthe, I., Fuger, J., Konings, R. J. M., Lemire, R. J., Muller, A. B., Nguyen-Trung, C., and Wanner, H.: Chemical thermodynamics of uranium, 1, North-Holland Amsterdam, 1992.

Grundmann, G. and Martinek, K.-P.: Erzminerale und Gangarten des Bergbaugebietes Schwaz und Brixlegg, Lapis, 19, 28–40, 1994.

Guilbert, J. M. and Park, C. F.: The geology of ore deposits, Waveland Press, Long Grove, Illinois, 985 pp., 2007.

Guillemin, C.: Mineralogy of the arsenates, phosphates, and vanadates of copper. I. Arsenates of copper, Bull. Soc. fr. minéral. cristallogr., 79, 7–95, 1956.

Hawthorne, F. C.: A bond-topological approach to theoretical mineralogy: Crystal structure, chemical composition and chemical reactions, Phys. Chem. Miner., 39, 841–874, https://doi.org/10.1007/s00269-012-0538-4, 2012.

Hawthorne, F. C.: The role of OH and H_2O in oxide and oxysalt minerals, Z. Kristallogr. Cryst. Mater., 201, 183–206, https://doi.org/10.1524/zkri.1992.201.14.183, 1992.

Hawthorne, F. C. and Sokolova, E.: The role of H_2O in controlling bond topology: I. The $^{[6]}Mg(SO_4)(H_2O)n$ (n=0–11) structures, Z. Kristallogr. Cryst. Mater., 227, 594–603, https://doi.org/10.1524/zkri.2012.1473, 2012.

Hawthorne, F. C. and Schindler, M.: Understanding the weakly bonded constituents in oxysalt minerals, Z. Kristallogr. Cryst. Mater., 223, 41–68, https://doi.org/10.1524/zkri.2008.0003, 2008.

Hill, R. J.: The crystal structure and infrared properties of adamite, Am. Mineral., 61, 979–986, 1976.

Hoefs, J.: Stable Isotope Geochemistry, 8th ed. 2018, Springer Textbooks in Earth Sciences, Geography and Environment, Springer International Publishing, Cham, 437 pp., 2018.

Holko, L., Dósa, M., Michalko, J., and Sanda, M.: Isotopes of oxygen-18 and deuterium in precipitation in Slovakia / Izotopy kyslíka-18 A deutéria v zrážkach na Slovensku, J. Hydrol. Hydromech., 60, 265–276, https://doi.org/10.2478/v10098-012-0023-2, 2012.

IAEA/WMO: Global Network of Isotopes in Precipitation. The GNIP Database. Accessible at: https://nucleus.iaea.org/wiser, 2019.

Ingwersen, G.: Die sekundären Mineralbildungen der Pb-Zn-Cu-Lagerstätte Tsumeb, Namibia (Physikalisch-chemische Modelle), PhD Dissertation, 234 pp., 1990.

Jambor, J. R.: Mineralogy of sulfide-rich tailings and their oxidation products, in: Environmental Geochemistry of Sulfide Mine-Wastes, 22nd ed., edited by: Jambor, J. R. and Blowes, D. W., Mineralogical Association of Canada Short Course, 59–102, 1994.

Jansa, J., Novák, F., Pauliš, P., and Scharmová, M.: Supergene minerals of the Sn-W deposit Cínovec in the Krušné hory Mts (Czech Republic), Bull mineral-petrolog Odd Nár Muz (Praha), 6, 83–101, 1998.

Jinnouchi, S., Yoshiasa, A., Sugiyama, K., Shimura, R., Arima, H., Momma, K., and Miyawaki, R.: Crystal structure refinements of legrandite, adamite, and paradamite: The complex structure and characteristic hydrogen bonding network of legrandite, J. Miner. Petrol. Sci., 111, 35–43, https://doi.org/10.2465/jmps.141216, 2016.

Kampunzu, A. B., Cailteux, J.L.H., Kamona, A. F., Intiomale, M. M., and Melcher, F.: Sediment-hosted Zn–Pb–Cu deposits in the Central African Copperbelt, Ore Geol. Rev., 35, 263–297, https://doi.org/10.1016/j.oregeorev.2009.02.003, 2009.

Kato, T. and Miúra, Y.: The crystal structures of adamite and paradamite, Mineral. J., 8, 320–328, https://doi.org/10.2465/minerj.8.320, 1977.

Keeling, J. L., Mauger, A. J., Scott, K. M., and Hartley, K.: Alteration mineralogy and acid sulphate weathering at Moonta cooper mines, South Australia, in: Advances in Regolith, edited by: Roach, I. C., CRC LEME, 230–233, 2003.

Keller, P.: Darstellung und Eigenschaften von $Co_2[OH|AsO_4]$, N. Jb. Miner. Mon., 560–564, 1971.

Kennedy, C. A., Stancescu, M., Marriott, R. A., and White, M. A.: Recommendations for accurate heat capacity measurements using a Quantum Design physical property measurement system, Cryogenics, 47, 107–112, https://doi.org/10.1016/j.cryogenics.2006.10.001, 2007.

Kimball, B. E., Mathur, R., Dohnalkova, A. C., Wall, A. J., Runkel, R. L., and Brantley, S. L.: Copper isotope fractionation in acid mine drainage, Geochim. Cosmochim. Acta, 73, 1247–1263, https://doi.org/10.1016/j.gca.2008.11.035, 2009.

Kiseleva, I. A., Ogorodova, L. P., Melchakova, L. V., Bisengalieva, M. R., and Becturganov, N. S.: Thermodynamic properties of copper carbonates: Malachite $Cu_2(OH)_2CO_3$ and azurite $Cu_3(OH)_2(CO_3)_2$, Phys. Chem. Miner., 19, https://doi.org/10.1007/BF00204009, 1992.

Kiseleva, I. A., Ogorodova, L. P., Melchakova, L. V., and Bisengalieva, M. R.: Thermodynamic properties of copper silicate: dioptase: $Cu_6Si_6O_{18}\cdot 6H_2O$, J. Chem. Thermodyn., 25, 621–630, https://doi.org/10.1006/jcht.1993.1057, 1993.

Kolesar, P. and Tvrdý, J.: Zarenschätze: Mineralien & Fundstellen in Russland, Armenien, Aserbaidschan, Georgien, Kasachstan, Kirgistan, Tadschikistan, Turkmenistan, Usbekistan, Weißrussland und in der Ukraine, Bode, Haltern, 720 pp., 2006.

Kolesova, R. V. and Fesenko, E. G.: Determination of the crystal structure of liroconite, $Cu_2Al(AsO_4)(OH)_4(H_2O)_4$, Kristallografiya, 13, 396–402, 1968.

Kösters, J., Paulsen, C., Stegemann, F., Heying, B., Galéa-Clolus, V., and Pöttgen, R.: Twinned olivenite from Cap Garonne, Mine du Pradet – structure and magnetic behavior, Zeitschrift für Kristallographie - Crystalline Materials, 235, 7–13, https://doi.org/10.1515/zkri-2019-0063, 2020.

Lafuente, B., Downs, R. T., Yang, H., and Stone, N.: The power of databases: The RRUFF project, in: Highlights in mineralogical crystallography, edited by: Armbruster, T. and Danisi, R. M., DE GRUYTER, Berlin, 1–30, https://doi.org/10.1515/9783110417104-003, 2015.

Larson, P. B., Maher, K. C., Ramos, F. C., Chang, Z., Gaspar, M., and Meinert, L. D.: Copper isotope ratios in magmatic and hydrothermal ore-forming environments, Chem. Geol., 201, 337–350, https://doi.org/10.1016/j.chemgeo.2003.08.006, 2003.

Lee, J. Y., Choi, J. C., Yi, M. J., Kim, J. W., Cheon, J. Y., Choi, Y. K., Choi, M. J., and Lee, K. K.: Potential Groundwater Contamination with Toxic Metals in and Around an Abandoned Zn Mine, Korea, Water Air Soil Pollut, 165, 167–185, https://doi.org/10.1007/s11270-005-4637-4, 2005.

Leverett, P., McKinnon A.R., and Williams, P. A.: Supergene geochemistry of the Endeavor ore body, Cobar, NSW, and relationships to other deposits in the Cobar basin, Regolith, 191–194, 2005.

Li, C., Yang, H., and Downs, R. T.: Redetermination of olivenite from an untwinned single-crystal, Acta Crystallogr. E, 64, i60-i61, https://doi.org/10.1107/S1600536808026676, 2008.

Lindgren, W.: Mineral Deposits, 4th ed., McGraw-Hill, New York, 930 pp., 1933.

Luptáková, J., Milovská, S., Jeleň, S., Mikuš, T., Milovský, R., and Biroň, A.: Primary ore Cu mineralization at the Ľubietová-Podlipa locality (Slovakia), Acta Geol. Slovaca, 8, 175–194, 2016.

Magalhães, M. C. F., De Jesus, J. D. P., and Williams, P. A.: The chemistry of formation of some secondary arsenate minerals of Cu(II), Zn(II) and Pb(II), Mineral. Mag., 52, 679–690, 1988.

Magalhães, M. C. F., Pedrosa de Jesus, J. D., and Williams, P. A.: Stability constants and formation of Cu(II) and Zn(II) phosphate minerals in the oxidized zone of base metal orebodies, Mineral. Mag., 50, 33–39, 1986.

Majzlan, J.: Solution calorimetry on minerals related to acid mine drainage – methodology, checks, and balances, Acta Geol. Slovaca, 9, 171–183, 2017a.

Majzlan, J., Števko, M., Chovan, M., Luptáková, J., Milovská, S., Milovský, R., Jeleň, S., Sýkorová, M., Pollok, K., Göttlicher, J., and Kupka, D.: Mineralogy and geochemistry of the copper-dominated neutral mine drainage at the Cu deposit Ľubietová-Podlipa (Slovakia), Appl. Geochem., 92, 59–70, https://doi.org/10.1016/j.apgeochem.2018.02.012, 2018.

Majzlan, J., Števko, M., Dachs, E., Benisek, A., Plášil, J., and Sejkora, J.: Thermodynamics, stability, crystal structure, and phase relations among euchroite, $Cu_2(AsO_4)(OH)\cdot 3H_2O$, and related minerals, EJM, 29, 5–16, https://doi.org/10.1127/ejm/2017/0029-2584, 2017b.

Majzlan, J., Plášil, J., Dachs, E., Benisek, A., and Bender Koch, C.: Crystal chemistry, Mössbauer spectroscopy, and thermodynamic properties of botryogen, N. Jb. Miner. Abh., 193, 147–159, https://doi.org/10.1127/njma/2016/0299, 2016.

Majzlan, J., Zittlau, A. H., Grevel, K.-D., Schliesser, J., Woodfield, B. F., Dachs, E., Števko, M., Chovan, M., Plášil, J., Sejkora, J., and Milovská, S.: Thermodynamic Properties and Phase Equilibria of the Secondary Copper Minerals Libethenite, Olivenite, Pseudomalachite, Kröhnkite, Cyanochroite, and Devilline, Can. Mineral., 53, 937–960, https://doi.org/10.3749/canmin.1400066, 2015.

Majzlan, J., Plášil, J., Škoda, R., Gescher, J., Kögler, F., Rusznyak, A., Küsel, K., Neu, T. R., Mangold, S., and Rothe, J.: Arsenic-rich acid mine water with extreme arsenic concentration: mineralogy, geochemistry, microbiology, and environmental implications, Environ. Sci. Technol., 48, 13685–13693, https://doi.org/10.1021/es5024916, 2014a.

Majzlan, J., Drahota, P., and Filippi, M.: Parageneses and Crystal Chemistry of Arsenic Minerals, Rev. Mineral. Geochem., 79, 17–184, https://doi.org/10.2138/rmg.2014.79.2, 2014b.

Majzlan, J., Grevel, K.-D., and Navrotsky, A.: Thermodynamics of Fe oxides: Part II. Enthalpies of formation and relative stability of goethite (α-FeOOH), lepidocrocite (γ-FeOOH), and maghemite (γ-Fe_2O_3), Am. Mineral., 88, 855–859, https://doi.org/10.2138/am-2003-5-614, 2003.

Maréchal, C. N. and Sheppard, S. M.F.: Isotopic fractionation of Cu and Zn between chloride and nitrate solutions and malachite or smithsonite at 30° and 50 °C, Gold. Conf., 2002.

Maréchal, C. N., Télouk, P., and Albarède, F.: Precise analysis of copper and zinc isotopic compositions by plasma-source mass spectrometry, Chem. Geol., 156, 251–273, https://doi.org/10.1016/S0009-2541(98)00191-0, 1999.

Markl, G., Marks, M. A. W., Holzapfel, J., and Wenzel, T.: Major, minor, and trace element composition of pyromorphite-group minerals as recorder of supergene weathering processes from the Schwarzwald mining district, SW Germany, Am. Mineral., 99, 1133–1146, https://doi.org/10.2138/am.2014.4789, 2014.

Markl, G., Lahaye, Y., and Schwinn, G.: Copper isotopes as monitors of redox processes in hydrothermal mineralization, Geochim. Cosmochim. Acta, 70, 4215–4228, https://doi.org/10.1016/j.gca.2006.06.1369, 2006.

Martens, W. and Frost, R. L.: An infrared spectroscopic study of the basic copper phosphate minerals: Cornetite, libethenite, and pseudomalachite, Am. Mineral., 88, 37–46, https://doi.org/10.2138/am-2003-0105, 2003.

Martens, W. N., Frost, R. L., Kloprogge, J. T., and Williams, P. A.: The basic copper arsenate minerals olivenite, cornubite, cornwallite, and clinoclase: An infrared emission and Raman spectroscopic study, Am. Mineral., 88, 501–508, https://doi.org/10.2138/am-2003-0404, 2003.

Mason, T. F.D., Weiss, D. J., Chapman, J. B., Wilkinson, J. J., Tessalina, S. G., Spiro, B., Horstwood, M. S.A., Spratt, J., and Coles, B. J.: Zn and Cu isotopic variability in the Alexandrinka volcanic-hosted massive sulphide (VHMS) ore deposit, Urals, Russia, Chem. Geol., 221, 170–187, https://doi.org/10.1016/j.chemgeo.2005.04.011, 2005.

Mathur, R. and Fantle, M. S.: Copper Isotopic Perspectives on Supergene Processes: Implications for the Global Cu Cycle, Elements, 11, 323–329, https://doi.org/10.2113/gselements.11.5.323, 2015.

Mathur, R., Falck, H., Belogub, E., Milton, J., Wilson, M., Rose, A., and Powell, W.: Origins of Chalcocite Defined by Copper Isotope Values, Geofluids, 2018, 1–9, https://doi.org/10.1155/2018/5854829, 2018.

Mathur, R., Titley, S., Barra, F., Brantley, S. L., Wilson, M., Phillips, A., Munizaga, F., Maksaev, V., Vervoort, J., and Hart, G.: Exploration potential of Cu isotope fractionation in porphyry copper deposits, J. Geochem. Explor., 102, 1–6, https://doi.org/10.1016/j.gexplo.2008.09.004, 2009.

Mathur, R., Ruiz, J., Titley, S., Liermann, L., Buss, H., and Brantley, S. L.: Cu isotopic fractionation in the supergene environment with and without bacteria, Geochim. Cosmochim. Acta, 69, 5233–5246, https://doi.org/10.1016/j.gca.2005.06.022, 2005.

McCrea, J. M.: On the Isotopic Chemistry of Carbonates and a Paleotemperature Scale, J. Chem. Phys., 18, 849–857, https://doi.org/10.1063/1.1747785, 1950.

Melchiorre, E. B., Criss, R. E., and Rose, T. P.: Oxygen and Carbon Isotope Study of Natural and Synthetic Azurite, Econ. Geol., 95, 621–628, https://doi.org/10.2113/gsecongeo.95.3.621, 2000.

Melchiorre, E. B., Criss, R. E., and Rose, T. P.: Oxygen and Carbon Isotope Study of Natural and Synthetic Malachite, Econ. Geol., 94, 245–260, 1999.

Minčeva-Stefanova, J.: Zink-Olivenit aus der Lagerstätte Zapačica und über den Chemismus und die Ablagerung der Kupferarsenate, Chemie der Erde, 4, 248–258, 1964.

Mitchell, V. L.: Health Risks Associated with Chronic Exposures to Arsenic in the Environment, Rev. Mineral. Geochem., 79, 435–449, https://doi.org/10.2138/rmg.2014.79.8, 2014.

Mohs, F. and Haidinger, W.: Treatise on Mineralogy: Or The Natural History of the Mineral Kingdom, Band 1, Archibald Constable, Edinburgh, 1825.

Nordstrom, D. K. and Archer, D. G.: Arsenic Thermodynamic Data and Environmental Geochemistry, in: Arsenic in Ground Water: Geochemistry and Occurrence, edited by: Welch, A. H. and Stollenwerk, K. G., Kluwer Academic Publishers, Boston, MA, 1–25, 2003.

Nordstrom, D. K., Majzlan, J., and Königsberger, E.: Thermodynamic Properties for Arsenic Minerals and Aqueous Species, Rev. Mineral. Geochem., 79, 217–255, https://doi.org/10.2138/rmg.2014.79.4, 2014.

Ondruš, P., Veselovský, F., Hloušek, J., Skála, R., Vavřín, I., Frýda, J., Cejka, J., and Gabašová, A.: Secondary minerals of the Jachymov (Joachimsthal) ore district, J. Geosci., 42, 3–76, 1997.

O'Neil, J. R., Clayton, R. N., and Mayeda, T. K.: Oxygen Isotope Fractionation in Divalent Metal Carbonates, J. Chem. Phys., 51, 5547–5558, https://doi.org/10.1063/1.1671982, 1969.

Palache, C., Berman, H., and Frondel, C.: Dana's System of Mineralogy, 7th ed., 2, Wiley & Sons, New York, 1951.

Parkhurst, D. L. and Appelo, C. A.J.: User's guide to PHREEQC (Version 2): A computer program for speciation, batch-reaction, one-dimensional transport, and inverse geochemical calculations, Wat.-res. inv. report, 99, 312, 1999.

Pękala, M., Asael, D., Butler, I. B., Matthews, A., and Rickard, D.: Experimental study of Cu isotope fractionation during the reaction of aqueous Cu(II) with Fe(II) sulphides at temperatures between 40 and 200°C, Chem. Geol., 289, 31–38, https://doi.org/10.1016/j.chemgeo.2011.07.004, 2011.

Petříček, V., Dušek, M., and Palatinus, L.: Crystallographic Computing System JANA2006: General features, Z. Kristallogr. Cryst. Mater., 345–352, https://doi.org/10.1515/zkri-2014-1737, 2014.

Plant, J. A., Bone, J., Voulvoulis, N., Kinniburgh, D. G., Smedley, P. L., Fordyce, F. M., and Klinck, B.: Arsenic and Selenium, in: Environmental geochemistry (Treatise on

Geochemistry), 11th ed., edited by: Holland, H. D. and Turekain, K. K., Elsevier, Amsterdam, 13–57, https://doi.org/10.1016/B978-0-08-095975-7.00902-5, 2014.

Plášil, J., Sejkora, J., Škoda, R., Novák, M., Kasatkin, A. V., Škácha, P., Veselovský, F., Fejfarová, K., and Ondruš, P.: Hloušekite, $(Ni,Co)Cu_4(AsO_4)_2(AsO_3OH)_2(H_2O)_9$, a new member of the lindackerite supergroup from Jáchymov, Czech Republic, Mineral. Mag., 78, 1341–1353, https://doi.org/10.1180/minmag.2014.078.5.16, 2014.

Plumhoff, A. M. and Majzlan, J.: External Appendix to Publication: "Thermodynamic properties, crystal structure and phase relations of pushcharovskite, geminite and liroconite", Digitale Bibliothek Thüringen (DBT), Jena, https://doi.org/10.22032/dbt.41075, 2020.

Pollard, A. M., Thomas, R. G., Williams, P. A., Just, J., and Bridge, P. J.: The synthesis and composition of georgeite and its reactions to form other secondary copper (II) carbonates, Mineral. Mag., 55, 163–166, 1991.

Pouchou, J. and Pichoir, F.: „PAP" (phi-rho-z) procedure for improved quantitative microanalysis, in: Microbeam Analysis, edited by: Armstrong, J.T., San Francisco Press, San Francisco, 104–106, 1985.

Psyrillos, A., Manning, D. A.C., and Burley, S. D.: Geochemical constraints on kaolinization in the St Austell Granite, Cornwall, England, J. Geol. Soc., 155, 829–840, https://doi.org/10.1144/gsjgs.155.5.0829, 1998.

Pushcharovsky, D. Y., Teat, S. J., Zaitsev, V. N., Zubkova, N. V., and Sarp, H.: Crystal structure of pushcharovskite, EJM, 12, 95–104, https://doi.org/10.1127/0935-1221/2000/0012-0095, 2000.

Qi, D., Behrens, H., Lazarov, M., and Weyer, S.: Cu isotope fractionation during reduction processes in aqueous systems: evidences from electrochemical deposition, Contrib. Mineral. Petrol., 2019.

Reich, M. and Vasconcelos, P. M.: Geological and Economic Significance of Supergene Metal Deposits, Elements, 11, 305–310, https://doi.org/10.2113/gselements.11.5.305, 2015.

Ridley, J.: Ore deposit geology, Cambridge Univ. Press, Cambridge, 398 pp., 2013.

Rigaku: CrysAlis CCD and CrysAlis RED, Rigaku-Oxford Diffraction Ltd, Yarton, Oxfordshire, UK, 2019.

Robie, R. A. and Hemingway, B. S.: Thermodynamic properties of minerals and related substances at 298.15 K and 1 bar (10^5 Pascals) and at higher temperatures, 2131, U.S. Geological Survey Bulletin, 461 pp., 1995.

Rouxel, O., Fouquet, Y., and Ludden, J. N.: Copper Isotope Systematics of the Lucky Strike, Rainbow, and Logatchev Sea-Floor Hydrothermal Fields on the Mid-Atlantic Ridge, Econ. Geol., 99, 585–600, https://doi.org/10.2113/gsecongeo.99.3.585, 2004.

Sarp, H. and Černý, R.: Description and crystal structure of yvonite, $Cu(AsO_3OH)2H_2O$, Am. Mineral., 83, 383–389, https://doi.org/10.2138/am-1998-3-423, 1998.

Sarp, H. and Sanz-Gysler, J.: La Pushcharovskite, $Cu(AsO_3,OH)\cdot H_2O$, un nouveau minéral de la mine de Cap Garonne, Var (France), Arch. Sci., 50, 177–186, 1997.

Sarp, H. and Perroud, P.: La Geminite $Cu_2As_2O_7\cdot 3H_2O$, un Nouveau Minéral de la Mine de Cap Garonne, Var, France, Schweiz. mineral. petro. Mitt., 70, 309–314, 1990.

Savin, S. M. and Epstein, S.: The oxygen and hydrogen isotope geochemistry of clay minerals, Geochim. Cosmochim. Acta, 34, 25–42, https://doi.org/10.1016/0016-7037(70)90149-3, 1970.

Schindler, M. and Hawthorne, F. C.: The stereochemistry and chemical composition of interstitial complexes in uranyl-oxysalt minerals, Can. Mineral., 46, 467–501, https://doi.org/10.3749/canmin.46.2.467, 2008.

Schnorrer, G.: Die Sekundärminerale des Bergbaugebietes Schwaz-Brixlegg in Tirol, Lapis, 19, 41–68, 1994.

Scott, P. W., Hart, F. W., and Smith, D.: The quantitative mineralogy of ceramic grade kaolin from the St. Austell Granite and its relationship to chemistry and physical properties, Proc. Ussher Soc., 9, 91–96, 1996.

Seguin, M. K.: Thermogravimetric and differential thermal analysis of malachite and azurite in inert atmospheres and in air, Can. Mineral., 13, 127–132, 1975.

Sejkora, J., Plášil, J., Ondruš, P., Veselovský, F., Císařová, I., and Hloušek, J.: Slavkovite, $Cu_{13}(AsO_4)_6(AsO_3OH)_4\cdot 23H_2O$, a new mineral species from Horní Slavkov and Jáchymov: description and crystal-structure determination, Can. Mineral., 48, 1157–1170, https://doi.org/10.3749/canmin.48.5.1157, 2010a.

Sejkora, J., Ondruš, P., Fikar, M., Veselovský, F., Mach, Z., Gabašová, A., Škoda, R., and Beran, P.: Supergene minerals at the Huber stock and Schnöd stock deposits, Krásno ore district, the Slavkovský les area, Czech Republic, Journal of the Czech Geological Society, 51, 57–101, https://doi.org/10.3190/JCGS.989, 2006.

Sejkora, J., Plášil, J., Veselovský, F., Císařová, I., and Hloušek, J.: Ondrušite, $CaCu_4(AsO_4)_2(AsO_3OH)_2\cdot 10H_2O$, a new mineral species from Jáchymov ore district, Czech Republic: Description and crystal-structure determination, Can. Mineral., 49, 885–897, https://doi.org/10.3749/canmin.49.3.885, 2011.

Sejkora, J., Ondruš, P., and Novák, M.: Veselovskýite, triclinic $(Zn,Cu,Co)Cu_4(AsO_4)_2(AsO_3OH)_2\cdot 9H_2O$, a Zn-dominant analogue of lindackerite, N. Jb. Miner. Abh., 187, 83–90, https://doi.org/10.1127/0077-7757/2010/0165, 2010b.

Sejkora, J., Škovíra, J., and Škoda, R.: Zincolivenite from the ore district Krupka, the Krušné Hory Mts., Czech republic, Bulletin mineralogicko-petrologickeho oddělení Narodního Muzea (Praha), 24–29, 2008.

Sheldrick, G. M.: SHELXT - integrated space-group and crystal-structure determination, Acta Crystallogr. A, 71, 3–8, https://doi.org/10.1107/S2053273314026370, 2015.

Sheppard, S. M.F.: The Cornubian batholith, SW England: D/H and $^{18}O/^{16}O$ studies of kaolinite and other alteration minerals, J. Geol. Soc., 133, 573–591, https://doi.org/10.1144/gsjgs.133.6.0573, 1977.

Sheppard, S. M.F., Nielsen, R. L., and Taylor, H. P.: Oxygen and hydrogen isotope ratios of clay minerals from porphyry copper deposits, Econ. Geol., 64, 755–777, https://doi.org/10.2113/gsecongeo.64.7.755, 1969.

Škácha, P., Plášil, J., and Horák, V.: Jáchymov – a mineralogical pearl of Krušné Hory Mts., Academia, 682 pp., 2019.

Smedley, P.L. and Kinniburgh, D.G.: A review of the source, behaviour and distribution of arsenic in natural waters, Appl. Geochem., 17, 517–568, https://doi.org/10.1016/S0883-2927(02)00018-5, 2002.

Southwood, M., Števko, M., and Carr, P.: Tsumeb: Zincolivenite and the adamite-olivenite series, Rock. Min., 95, 210-233, https://doi.org/10.1080/00357529.2020.1716168, 2020.

Števko, M., Sejkora, J., and Bačík, P.: Mineralogy and origin of supergene mineralization at the Farbište ore occurrence near Poniky, central Slovakia, J. Geosci., 273–298, https://doi.org/10.3190/jgeosci.098, 2011.

Števko, M., Sejkora, J., and Súľovec, Š.: Contribution to the chemical composition of libethenite from the type locality: Podlipa copper deposit, Ľubietová (Slovak Republic), Bull. Mineral. Petrolog., 25, 252–259, 2017.

Strunz, H. and Nickel, E. H.: Strunz mineralogical tables: Chemical-structural mineral classification system, 9. ed., Schweizerbart, Stuttgart, 870 pp., 2001.

Stumpp, C., Klaus, J., and Stichler, W.: Analysis of long-term stable isotopic composition in German precipitation, J. Hydrol., 517, 351–361, https://doi.org/10.1016/j.jhydrol.2014.05.034, 2014.

Szakáll, S., Birch, W. D., Kovács, Á., and Postl, W.: Arsenate minerals from Hungary, Acta Mineralogica-Petrographica, 5–25, 1994.

Tanaka, H. and Yamane, M.: Preparation and thermal analysis of synthetic malachite $CuCO_3 \cdot Cu(OH)_2$, J. Therm. Anal., 38, 627–633, https://doi.org/10.1007/BF01979390, 1992.

Tarantino, S. C., Zema, M., Callegari, A. M., Boiocchi, M., and Carpenter, M. A.: Monoclinic-to-orthorhombic phase transition in $Cu_2(AsO_4)(OH)$ olivenite at high temperature: strain and mode decomposition analyses, Mineral. Mag., 82, 347–365, https://doi.org/10.1180/minmag.2017.081.048, 2018.

Taylor, H. P.: Water/rock interactions and the origin of H_2O in granitic batholiths, J. Geol. Soc., 133, 509–558, https://doi.org/10.1144/gsjgs.133.6.0509, 1977.

Toman, K.: Ordering in olivenite–adamite solid solutions, Acta Crystallogr. B, 34, 715–721, https://doi.org/10.1107/S0567740878003933, 1978.

Toman, K.: The symmetry and crystal structure of olivenite, Acta Crystallogr. B, 33, 2628–2631, https://doi.org/10.1107/S0567740877009042, 1977.

Urey, H. C.: The thermodynamic properties of isotopic substances, J. Chem. Soc., 562–581, https://doi.org/10.1039/jr9470000562, 1947.

Vasconcelos, P. M., Reich, M., and Shuster, D. L.: The Paleoclimatic Signatures of Supergene Metal Deposits, Elements, 11, 317–322, https://doi.org/10.2113/gselements.11.5.317, 2015.

Velasco, F., Herrero, J. M., Suárez, S., Yusta, I., Alvaro, A., and Tornos, F.: Supergene features and evolution of gossans capping massive sulphide deposits in the Iberian Pyrite Belt, Ore Geol. Rev., 53, 181–203, https://doi.org/10.1016/j.oregeorev.2013.01.008, 2013.

Viehweg, M.: Regionale Verteilung der Uranlagerstätten Sachsens und Thüringens, Z. Geol. Wiss., 23, 547–552, 1995.

Vitali, F., Longstaffe, F. J., Bird, M. I., Gage, K. L., and Caldwell, W.G. E.: Hydrogen-isotope fractionation in aluminum hydroxides: Synthesis products versus natural samples from bauxites, Geochim. Cosmochim. Acta, 65, 1391–1398, https://doi.org/10.1016/S0016-7037(00)00604-9, 2001.

Vogl, J. F.: Über das Vorkommen einer dem Voltzin ähnlichen Schwefelzink-Verbindung in Joachimsthal, Z. mont. Ver. Erzg., 1, 5, 1853.

Whitney, D. L. and Evans, B. W.: Abbreviations for names of rock-forming minerals, Am. Mineral., 95, 185–187, https://doi.org/10.2138/am.2010.3371, 2010.

Williams, P. A.: Oxide Zone Geochemistry, Ellis Horwood Ltd., Chichester, 286 pp., 1990.

Williams, P. A., Leverett, P., Birch, W. D., Hibbs, D. E., Kolitsch, U., and Mihajlovic, T.: Zinc-rich zincolibethenite from Broken Hill, New South Wales, Australian Journal of Mineralogy, 12, 3–7, 2006.

Wongsasuluk, P., Chotpantarat, S., Siriwong, W., and Robson, M.: Heavy metal contamination and human health risk assessment in drinking water from shallow groundwater wells in an agricultural area in Ubon Ratchathani province, Thailand, Environmental geochemistry and health, 36, 169–182, https://doi.org/10.1007/s10653-013-9537-8, 2014.

Zema, M., Tarantino, S. C., and Callegari, A. M.: Thermal behaviour of libethenite from room temperature up to dehydration, Mineral. Mag., 74, 553–565, https://doi.org/10.1180/minmag.2010.074.3.553, 2010.

Zhu, X. K., Guo, Y., Williams, R. J.P., O'Nions, R. K., Matthews, A., Belshaw, N. S., Canters, G. W., Waal, E. C. de, Weser, U., Burgess, B. K., and Salvato, B.: Mass fractionation processes of transition metal isotopes, EPSL, 200, 47–62, https://doi.org/10.1016/S0012-821X(02)00615-5, 2002.

Zhu, X. K., O'Nions, R. K., Guo, Y., Belshaw, N. S., and Rickard, D.: Determination of natural Cu-isotope variation by plasma-source mass spectrometry: Implications for use as

geochemical tracers, Chem. Geol., 163, 139–149, https://doi.org/10.1016/S0009-2541(99)00076-5, 2000.

7 Appendix

Table 7-1. Comparison of our mineral-solution oxygen isotope fractionation factors with carbonate-H_2O factors, all plotted as a function of temperature.

temperature range	A	B	phase- H_2O	source
0-50	2.66	2.66	malachite ($Cu_2CO_3(OH)_2$) - H_2O	Melchiorre et al. (1999)
0-500	2.78	-2.89	calcite ($CaCO_3$) - H_2O	Friedman and O'Neil (1977)
0-500	2.69	-3.24	strontianite ($SrCO_3$) - H_2O	Friedman and O'Neil (1977)
0-500	2.57	-4.23	witherite ($BaCO_3$) - H_2O	Friedman and O'Neil (1977)
33-197	3.13	-3.50	siderite ($FeCO_3$) - H_2O	Carothers et al. (1988)
10-45	2.67	4.75	azurite ($Cu_3(CO_3)_2(OH)_2$) - H_2O	Melchiorre et al. (2000)
20-65	2.63	-3.58	cerussite ($PbCO_3$) - H_2O	Melchiorre et al. (2001)
20-90	2.83	-2.85	norsethite ($BaMg(CO_3)_2$) - H_2O	Bötcher (2000)

Values for A and B of the equation for the isotopic fractionation factors of oxygen in the form of $1000 \ln \alpha = A (10^6 / T^2) + B$, with T the temperature in Kelvin.

Table 7-2. Comparison of our mineral-solution hydrogen isotope fractionation factors with mineral-H_2O factors, all plotted as a function of temperature.

temperature range	A	B	phase- H_2O	source
25-90	4.88	-22.54	brucite ($Mg(OH)_2$) - H_2O	Xu and Zheng (1999)
25-400	1.56	-4.70	serpentine ($Mg_6Si_4O_{10}(OH)_8$) - H_2O	Wenner and Taylor (1973)
0-330	-2.2	-7.7	kaolinite ($Al_4Si_4O_{10}(OH)_8$)-H_2O	Gilg and Sheppard (1996)
independent of temperature				
17-57	-15 ‰		gypsum ($CaSO_4 \cdot 2H_2O$)-H_2O	Fontes and Gonfiantini (1967)
25	-22.7 ‰		chalcanthite ($CuSO_4 \cdot 5H_2O$)-H_2O	Heinzinger (1969)
9-51	-5 ‰		gibbsite ($Al(OH)_3$)-H_2O	Vitali et al. (2001)

Values for A and B of the equation for the isotopic fractionation factors of oxygen in the form of $1000 \ln \alpha = A (10^6 / T^2) + B$, with T the temperature in Kelvin.

Content of disk

- DissPlumhoff.pdf — This Dissertation as pdf-File
- liroconite.cif — Crystallographic information file of liroconite
- thermo_CuArsenate.tdat — Extended LLNL thermodynamic database